COMPOSITION AND STRUCTURE DEPENDENCE OF THE PHOTOELASTIC RESPONSE OF OXIDE GLASS

by

Vincent Martin

Submitted in partial fulfillment of the
requirements for the degree of
Doctor of Philosophy

at

Dalhousie University
Halifax, Nova Scotia
August 2011

© Copyright by Vincent Martin, 2011

DALHOUSIE UNIVERSITY

DEPARTMENT OF CHEMISTRY

The undersigned hereby certify that they have read and recommend to the Faculty of Graduate studies for acceptance a thesis entitled "COMPOSITION AND STRUCTURE DEPENDENCE OF THE PHOTOELASTIC RESPONSE OF OXIDE GLASS" by Vincent Martin in partial fulfillment of the requirements for the degree of Doctor of Philosophy.

Dated: 05 August 2011

External Examiner: _____

Research Supervisor: _____

Examining Committee: _____

_____

_____

Departmental Representative: _____

DALHOUSIE UNIVERSITY

DATE: 05 August 2011

AUTHOR: Vincent Martin

TITLE: COMPOSITION AND STRUCTURE DEPENDENCE OF THE PHOTOELASTIC RESPONSE OF OXIDE GLASS

DEPARTMENT OR SCHOOL: Department of Chemistry

DEGREE: Ph.D. CONVOCATION: October YEAR: 2011

Permission is herewith granted to Dalhousie University to circulate and to have copied for non-commercial purposes, at its discretion, the above title upon the request of individuals or institutions. I understand that my thesis will be electronically available to the public.

The author reserves other publication rights, and neither the thesis nor extensive extracts from it may be printed or otherwise reproduced without the author's written permission.

The author attests that permission has been obtained for the use of any copyrighted material appearing in the thesis (other than brief excerpts requiring only proper acknowledgement in scholarly writing) and that all such use is clearly acknowledged.

_____

Signature of Author

Table of Contents

List of Tables

List of Figures

Abstract

The isotropy of a glass can be broken by the application of a mechanical stress giving rise to a phenomenon of birefringence. Some lead-containing glass compositions are known to prevent this phenomenon and they are called zero-stress optic glass. Mueller's theory of photoelasticity attempts to explain the structural origin of the photoelastic response in glass and crystal. Zwanziger's empirical model is able to predict the photoelastic response of a glass based on its composition and the crystal structure of its constituents.

Lead-, tin-, antimony-, zinc-, and cadmium-containing glasses were investigated in the binary silicate, borate, and phosphate systems. The stress optic coefficient of these binary glasses was measured experimentally using the Sénarmont method or found in the literature. Solid-state Nuclear Magnetic Resonance spectroscopy and Mössbauer spectroscopy were mainly used to investigate the local environment of the cations. The photoelastic response of a glass and its structure were correlated, and the results were compared with the expectations arising from Mueller's theory and Zwanziger's empirical model. The theory and the model were both tested and their reliability was discussed.

Zero-stress optic glasses are of technological interest, but new environmental regulations forbids the use of lead in materials, including glass. From experimental results and literature, a global strategy to design new zero-stress optic glasses was established. New lead-free zero-stress optic glasses were discovered with properties similar to the lead-containing zero-stress optic glass (high index of refraction, transparency, no coloration).

The study of the structural dependence of the photoelastic response of oxide glass contributed to identify new parameters influencing the photoelasticity, such as covalency, polarizability and natural deformation of the additive.

List of Abbreviations and Symbols Used

x: Molar fraction of additive

T_m: melting temperature

T_g: Glass transition temperature

σ: mechanical stress, chemical shielding

q_{ijkl}: Stress optic coefficient (tensor notation)

C: Stress optic coefficient

n: Refractive index

Δn: Birefringence

d: Cation-oxygen bond length

N_c: Cation's coordination number

ω: Angular frequency

α: Angular phase retardation

θ: Measured angle

δ_{PL}: Effective path length difference

l: Sample's width

λ: Wavelength

NMR: Nuclear Magnetic Resonance

μ: Magnetic moment

γ: Gyromagnetic ratio

$\hbar$: Reduced Planck's constant

I: Quantum spin number

$\overrightarrow{B_0}$: Applied magnetic field

ν_0: Larmor frequency

k: Boltzmann's constant

E: Energy

$\overrightarrow{M}$: Net magnetization

$\overrightarrow{B_1}$: Additional magnetic field

FID: Free-Induction Decay

CSA: Chemical Shift Anisotropy Δ: Anisotropy

η: Asymmetry

δ: Chemical shift

MAS: Magic Angle Spinning

f: Recoil-free fraction

v_D: Doppler velocity

ϵ: Energy shift

IS: Isomer Shift

QS: Quadrupole Splitting

ρ: Density

Acknowledgements

The first person I want to thank is my wife, Dr. Alexandra Mortimer, who always supported me and believed in me. Without you, I would never have made it this far. You really changed my life.

I also want to thank my supervisor, Dr. Josef W. Zwanziger, who offered me the chance to work on a project I truly enjoyed, and who was always available to provide useful advice. Also, thank you for your patience with my english when I first arrived at Dalhousie.

The work presented in this thesis was realized with the help of numerous students and post-doctoral fellows who worked in the Zwanziger's research group. Especially Dr. Marie Guignard who initiated the study on the tin phosphate glasses, Bryanna Wood who provided a large contribution to the study of the lead borate glasses, and also Dr. Banghao H. Chen, Justine Galbraith, and Victoria Dickinson.

If I had to perform the structural analysis all by myself, I would probably still be working on my very first project. Thankfully, I was able to count on amazing people who made the work much easier: Dr. "Ulli" Werner-Zwanziger for the Solid-State Nuclear Magnetic Resonance spectroscopy, and Dr. Richard Dunlap for the Mössbauer spectrocopy. Thank you both for all your work and availability, without you I would not have gone very far. I also wish to thank Dr. Heather Andreas and Dr. Peng Zhang. Your advices from the qualifying examination and all the discussions we had after that were well received.

There are so many people I still want to thank but the list would be too long. To not forget anybody, I should just say thank you to all faculty and staff at Dalhousie University who made these last four years a very special chapter of my life.

And last but not least, a special thanks to my parents, my two brothers and my parents-in-law for all their support.

Chapter 1

Introduction

Man's evolution is closely related to its ability to master specific materials. It is not surprising that the three-age system in archeology divides human prehistory in three periods named after three materials successively discovered and used: the stone age, the bronze age, and the iron age. Nowadays, many materials that surround us in our daily life are derived from the metals, which were among the very first materials exploited by men, up to the most recent discovery of carbon nanotubes in the early 1990s [1]. Among all these materials, glass remains one of the most fascinating on account of its nature, its properties, and also its history. Glass is not a human invention, it has probably existed since the earliest times of Earth. It can be created in nature from different methods, and it exists under different forms. The most famous kind of natural glass is probably the *fulgurite* which is a tube of amorphous silica formed by the impact of lightning on sand or silicate-rich soil [2]. The *obsidian* is another common geological glass. It is an alumino-silicate volcanic glass created by the rapid cooling of lava containing mainly Na, K, Ca, Fe and Mn oxides [3]. It was one of the main "rocks" used in the stone age due to its ability to produce sharp shards useful for making blades or arrowheads. The *impactites* and *tektites* are two

other types of geological glasses obtained by the shock of a meteorite impact. The impactites are formed from crystalline materials rendered amorphous by the impact, whereas the tektites are formed from the impacted melt [3]. Living organisms, mostly marine creatures, can also synthesize glass as a constituent of their skeleton or to create a shell. Radiolarians and diatoms are microscopic organisms (phytoplankton and zooplankton) using amorphous silica as a cellular membrane [4]. On a bigger scale, amorphous silica is synthesized by some species of sponge called *hexactinellid sponges*, also known as *glass sponges*, living primarily in deep and cold water of the arctic ocean [5]. In this species, the amorphous silica forms the skeleton of the living entity.

The first glass synthesis carried out by man is estimated at 3000 B.C. in Mesopotamia (area covering Iraq and parts of Syria, Turkey and Iran) and the oldest reference about glass discovery comes from Pliny the Elder in his encyclopedic work *Naturalis Historia* [6]. The story tells of merchants who were preparing their dinner on a seashore and could not find any stones to support their cauldrons. They decided to use lumps of nitre (Na_2CO_3) instead, which were a part of their merchandise. The mixture of nitre with sand (SiO_2) under the action of fire gave a new material nobody had ever seen before [6].

The large amount of glass objects found in Egypt suggests that its use became very popular around 1500 B.C. [7]. At this time glass blowing techniques did not exist, and it seems that threads of melted glass were applied on sand and clay pottery [3]. It should be noted that the first pieces of glass (bottles, flasks) were not transparent. The colorful objects from this period show that egyptians already knew a variety of pigments that could be added to the glass compositions. Some egyptian glass pieces are shown in Figure 1.1.

Glass making knowledge spread to eastern territories, mostly Syria, Cyprus, and along the south coast of the Mediterranean sea. Syrians and Palestinians became

Figure 1.1: Egyptian glass pieces displayed at the Corning Museum of Glass.

active glass makers initially by using techniques inherited from the egyptians, until they discovered the glass blowing technique, that would become one of the most important revolutions in the history of glass [3, 7]. With this technique it became possible to create highly symmetrical (spherical) glassware and complex shapes. This glass blowing technique is still used today for traditional hand-made artisanal glass pieces or in blow molding techniques for industrial production.

For centuries, the art of glass was exported into different regions mainly located around the Mediterranean sea. Greece and Macedonia became major glass centers around 400 B.C.. They perfected the techniques to create tableware, such as bowls and glasses, and also improved the color of glass and surface grinding techniques. The glass making knowledge which appeared in western Europe, mainly in Italy, with the emergence of the Roman Empire between 300 and 200 B.C. probably had the most important influence on the evolution of glass composition and techniques [3]. Glass was a very popular material in Rome, and it was used for a wider range of objects than at any other time in history, including the present day. At that time it was

mostly appreciated for interior decorative purposes [7]. One of the most significant symbol of roman culture is perhaps glass pieces made of *cameo* glass. The art of glass became a strong part of the italian city's culture, and persisted for centuries. The status of the venetian master glass blowers in the XIIIth century is certainly the best example of the strong ties connecting Italy and the art of glass. In order to avoid the danger of fire induced by the use of high temperatures, venetian glass blowers were obligated to move their workshop to Murano island. With its high concentration of glass makers, the island became the epicenter of glass industry. It was here that major innovations were developed, such as the addition of calcia ($CaCO_3$) to give clear transparent *crystallo* glass, and the addition of tin oxide to create glass that imitates precious stones (*calcedonio* glass) [7]. Murano became the most famous glass making place of western Europe, and where secret glass compositions and techniques were developed. Murano glass was so famous and prestigious that glass blowers and their families were considered equal to aristocrats. To protect the wealth and prestige of this art, the glass blowers were forced to remain living on the Murano island. Those who left the island to settle out of the Venetian area were subjected to the death penalty [8].

Another important step in the development of glass is the discovery of lead-containing glass, also called *flint* glass, attributed to Ravenscroft in 1674 [9] in England. Ravenscroft was looking for a new glass composition able to compete with the high quality Venetian glass when he heard about a patent of a glass of similar appearence to the Venetian glass, but of different composition. Unfortunately the high amount of alkaline salts in the composition gave a partially crystallized glass. From this composition, Ravenscroft decided to substitute parts of the salts with lead oxide, and he obtained a highly transparent and shiny glass, also known as *crystal* glass. The introduction of lead oxide in the glass also brings interesting technical properties which are detailed farther in this chapter.

More recent significant progress in terms of glass compositions are probably the discovery of metallic glasses in 1960 by W. Klement *al.* [10] which gave rise to the bulk metallic glasses considered as potential substitutes to plastic materials [11]; and the discovery of heavy metal fluoride glasses in 1975 by Poulain *et al.* [12] mainly used for optical applications and infra-red transmission.

Glass is one of the most used materials, it is suitable for many applications such as packaging (bottles), construction (windows, see Figure 1.2), telecommunication (optic fiber) and medical applications (emetic, biomaterial and bioactive materials). Chemistry itself would not have known the development we know without glassware made of borosilicate glass. In spite of its long and rich history and all the recent

Figure 1.2: The glass covered Purdy's Wharf towers in Halifax are part of the city's identity.

advances in terms of research, production, and engineering, the structure of many glasses remains unsolved. The technology based on crystals arises mostly from the knowledge of their structure, such as their conductive properties used for semiconductors or their diffractive properties used in monochromators for diffraction techniques. Crystalline materials are ordered structures, and all different types of crystals can be classified according to their Bravais lattice for example. Such a classification is not possible with amorphous materials like glass. Glass technology is mostly based on experimental observations and empirical models such as Cauchy's equation of the dispersion of the refractive index [13]. The present work is no exception to this tendency, and it focuses on the structural dependence of the photoelastic response of oxide glass. The structure of glass was investigated with the help of Nuclear Magnetic Resonance spectroscopy and Mössbauer spectroscopy to obtain information mostly about the first sphere of coordination of the elements present in the glass. The photoelasticity of a material is its ability to transform the light, or more specifically to polarize it. It is characterized by a stress optic coefficient usually noted C, and its unit is the Brewster (1 Brewster = 1 MPa^{-1}). The great majority of glasses have a positive stress optic coefficient. When they are subjected to a stress (mechanical or thermal for example), the light emerging from the material is in a different state of polarization than the entering light. The most common photoelastic phenomenon is the *double-refraction*, also called *birefringence*, and it can be observed in transparent crystals with a non-cubic Bravais lattice such as the calcite ($CaCO_3$) [14]. The phenomenon of birefringence is a problem for optical applications requiring glass subjected to a stress such as Liquid Crystal on Silicon (LCoS) projection display where the glass can expand due to the heat in the system, or optical fiber where mechanical stresses are applied on the glass due to the bending of the fiber [15]. In the early 1900s, Pockels discovered the influence of lead oxide on the photoelastic response

of silicate glasses [16]. In general, silicate glasses have a positive stress optic coefficient, but the addition of lead oxide decreases this value until it turns negative. This means that for a given composition the stress optic coefficient is equal to zero. These glass compositions are called *zero-stress optic* glasses and they are of technological interest because of their ability to prevent the phenomenon of birefringence under stress. This kind of glass finds its application in LCoS projection display and optical waveguide as previously mentioned but also in telescope [17] and ellipsometer [18] for example. The most common commercial zero-stress optic glass is the Schott SF57. Since July 2006, the Restriction of Hazardous Substances (RoHS) was introduced in Europe. This environmental regulation forbade the use of six substances in new materials [19]:

- Lead
- Cadmium
- Mercury
- Hexavalent chromium
- Polybrominated biphenyls
- Polybrominated diphenyl ether

This new regulation was first applied in Europe, but it is now extended to Asia, Pacific area and North America. For over a century, only lead oxide was used to reduce the stress optic coefficient in glass. Thallium dioxide and bismuth trioxide were also known to decrease the stress optic coefficient, but their use was excluded from any optical glass compositions because of the high toxicity of thallium and the dark color of bismuth [20,21]. Therefore new substitutes have to be found to produce lead-free zero-stress optic glass.

The present work investigates the structural origin of the photoelastic response of oxide glass and takes advantage of current knowledge in this field to design new lead-free zero-stress optic glasses that could potentially substitute the SF57 glass. To define the orientation of the work presented in this thesis, concepts about glass

structure are explained in the second chapter. A brief definition of glass is provided to clarify what distinguishes this particular material from other materials. Also, the two main theories of glass structure are presented with some historical facts to highlight the difficulties glass scientists have to establish a unique structural model. Finally, the classification of the oxides in relation to their role in the glass structure is provided. This last point is the basis of the formulation of new glass compositions. It needs to be presented to understand the strategy adopted to make glass in the various experiments exposed in the next chapters (chapter 5 to chapter 8), as well as to find new zero-stress optic glass compositions.

The third chapter defines the nature of photoelasticity and its mathematical expressions. The occurrence of double-refraction is also explained and illustrated with the help of the Snell-Descartes law of optics. This chapter introduces Mueller's theory of photoelasticity and the Zwanziger's empirical model which both connect glass structure and photoelastic response. These two concepts are the heart of the work presented in this thesis. Both theories were tested and compared with experimental results in the case of various binary glass systems. Their reliability and accuracy are the subject of numerous discussions in the case of each glass system.

The experimental techniques used to analyze the glass structure and properties are described in the fourth chapter. A brief description of Nuclear Magnetic Resonance spectroscopy and Mössbauer spectroscopy is provided, however it is important to note that only a general description of each techniques is presented. NMR and Mössbauer techniques have been developed for decades, and they have reach state of the art in solid-state analysis. Many textbooks are dedicated to each techniques and can provide detailed information about a specific element or isotope analysis. These techniques are valuable tools for glass analysis but they are not the main subject of this thesis, therefore only information necessary to understand the experiments and their results are provided. Conversely, the Sénarmont method [22], also known as the Friedel's method of compensation [23], used to determine the stress optic coefficient is not as common. Therefore a detailed description of the experiment is given. The

purpose of each optics involved in the experimental set-up and the state of polarization of the light after each optics is derived mathematically. A few words are also written about the density and refractive index measurements.

The glass systems prepared to test the Mueller's theory and Zwanziger's empirical model are binary systems made of the combination of one glass network former (SiO_2, B_2O_3, P_2O_5) and a metallic oxide (PbO, SnO, Sb_2O_3, ZnO, CdO). All glass compositions are expressed using the molar fraction x of additive. Similar to lead, cadmium is listed as an hazardous substance by the RoHS. The cadmium-containing glasses were prepared only with the scientific purpose of correlating the structure and photoelastic response. No lead-free glasses were prepared using CdO. Chapters 5 through 8 are dedicated to the structural correlation of the photoelastic response of glass for different systems based on the metallic oxide introduced in the glass composition. Results for lead-, tin-, antimony-, zinc- and cadmium-containing glass are presented. Binary systems were prepared and analyzed in order to test Mueller's theory and the Zwanziger's model, whereas ternary systems presented in the end of the tin and antimony chapters were designed with the objective to find new lead-free zero-stress optic glass compositions. In addition to experimental results and interpretation of the glass systems prepared, other binary glass systems, with data available in the literature about their structure and photoelastic response, are presented and discussed. The purpose of this work was to regroup a maximum amount of information about the correlation of the structure and photoelasticity, and to determine a global behavior of the metallic oxide according to the value of the stress optic coefficient.

In chapter 9, expectations from Mueller's theory and experimental data are compared, and the reliability of the theory is discussed based on previous observations and conclusions. Also, from the experimental results obtained in this work and derived from the literature, new concepts are developed to highlight the origin of the structural dependence of the photoelasticity in glass. With the help of the experimental data and some important work found in the literature, a classification of

simple oxides entering the glass compositions is correlated with the influence of these oxides on the stress optic coefficient. The comparison of several physical properties of the simple oxides also provides more information about the origin of the photoelastic response in glass. Finally, a general description of the role of each term in Zwanziger's empirical model is provided according to previous statements, in order to explain qualitatively the physics behind this model.

Many new ideas to study the photoelastic response of glass and to design new lead-free zero-stress optic glass compositions emerged from this work. Unfortunately time is one of the worst enemies of the grad student and most of these projects were not realized, therefore all these ideas are explained in the last chapter regrouping potential future studies and the conclusion arising from the previous chapters.

All of the work presented in this thesis was carried out with the hope of bringing a small but significant contribution to the understanding of the photoelasticity in glass. Experiments and interpretations were inspired mainly by the previous works of Mueller [24–26], Matusita [27–29], and many others.

I hope that anybody who will read this thesis will enjoy it as much as I enjoyed working on this project.

Chapter 2

Glass structure

The present thesis intends to highlight the relationship between the glass structure and the photoelastic response of glass, therefore it is important to expose and clarify the point of view adopted in this work. Glass scientists are well aware of the ninety year old "battle" between the two main theories that intend to describe the glass structure: the "Crystallite hypothesis" and the "Random Network Theory". Some concepts about glass structure and brief descriptions of the two structural theories are provided in this chapter.

2.1 Definition of glass

Glass is a common material used every day by billions of people and is commonly known as a transparent and brittle material. However, these two properties are not sufficient to properly define this material. The structure of a glass is often compared to the structure of the crystal of the same composition. A liquid mixture cooled below its melting point T_m usually gives a crystal. The volume of the mixture decreases suddenly at T_m due to the ordered arrangement of the molecules giving

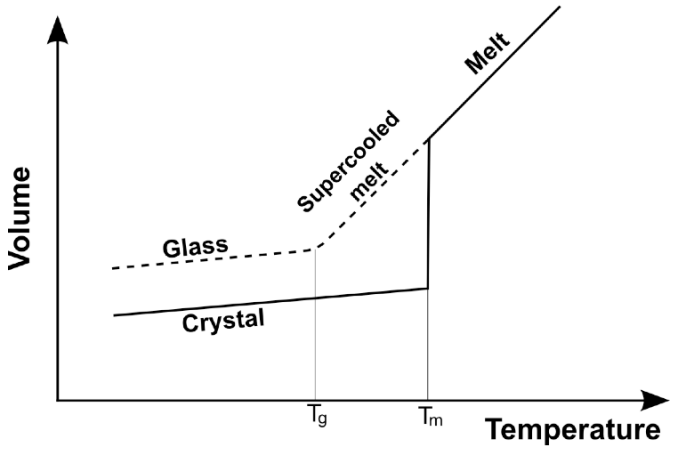

Figure 2.1: Evolution of the volume for a glass and a crystal.

rise to a more compact structure than in the liquid (see Figure 2.1) [30]. For a glass, the melt remains liquid below the melting point. It is called *supercooled melt* or *supercooled liquid*, the volume continues to decrease at the same rate until its viscosity progressively decreases to finally obtain a glass (amorphous solid). The progressive transition from liquid to glass (solid) is the *glass transition* and it is characterized by the *glass transition temperature* T_g which corresponds to the temperature where the melt has a specific viscosity of 10^{13} poises (1 poise = 1 Pa.s). The volume of the glass is higher than the volume of the crystal, but their variation with the temperature remains the same. The glass is a metastable solid which will eventually crystallize depending on its stability [31]. The glass transition is a unique property specific to the glass, but a given glass composition cannot be associated with a single glass transition temperature. The cooling rate of the melt affects the value of the Tg as shown in Figure 2.2, therefore a same glass composition has a range of possible glass transition temperatures [32].

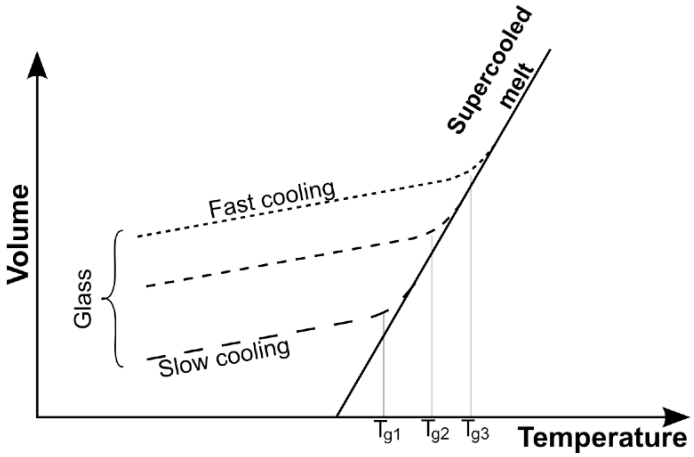

Figure 2.2: Glass transition temperatures for a same glass. Depending on the cooling rate, a same glass can have a different glass transition temperature.

2.2 Theories of glass structure

2.2.1 Crystallite Hypothesis

The birth of the Crystallite Hypothesis is attributed to Lebedev who suggested in 1921 that a glass is made of '*tiny crystals*" [33,34]. However, it should be noted that a similar idea was already stated in 1835 by Frankenheim [35], who mentioned the idea of *"a gradual transition from the solid state to a softened and eventually a liquid one to a first melting of the "lubricant" between aggregates of a larger size"* [36]. By this affirmation, Frankenheim was referring to the phenomenon of glass transition. Lebedev's theory originates mainly from the fact that silica-based glasses show an abrupt change of the thermal expansion at temperatures in the range of 570°C to 580°C, which is close to the temperature corresponding to the crystalline quartz $\alpha \leftrightarrow \beta$ transition [37]. Nevertheless, this change is not observed in the case of fused quartz (pure amorphous silicon dioxide) which invalidates Lebedev's conclusion [38]. In the beginning of the 1970s, it has been stated that no contemporary method,

including X-ray diffraction, was able to detect the presence of crystallite in glass [39]. This statement seemed to definitively reject the crystallite hypothesis, but in the following decade many authors declared that they detected regions of ordered silica sized from 11 to 66 Å in glasses [40–43]. All these affirmations were also strongly criticized based on the ambiguous nature of the results' interpretations [44–46].

2.2.2 Random Network Theory

The most famous and well accepted theory describing the structure of glass was published by Zachariasen in 1932 [47]. According to this theory a glass is made of the same polyhedron as the crystal of similar composition with the difference that the repetition of a unique pattern found in a crystal does not exist in a glass. In this last case the polyhedra are randomly distributed (Figure 2.3). From this theory the

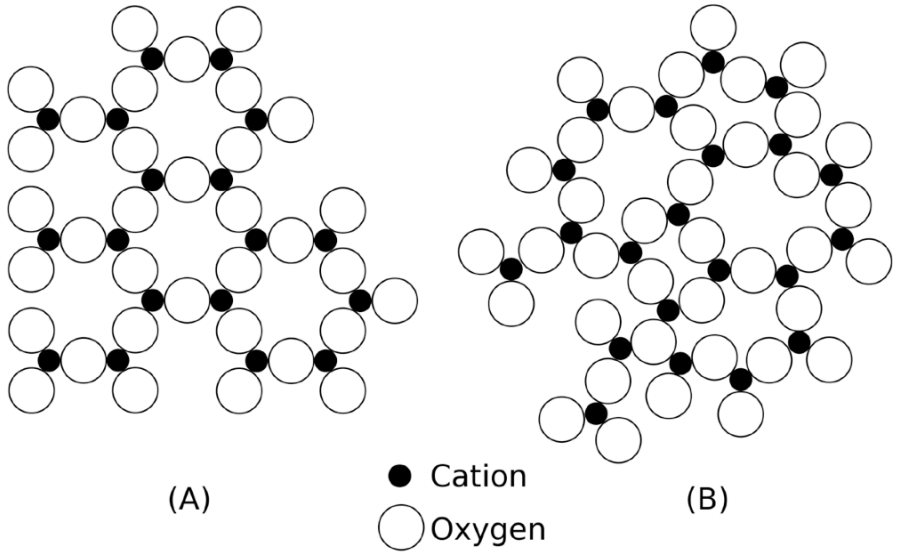

Figure 2.3: Representation of the crystalline structure (A) and glass structure (B) of an oxide M_2O_3 according to the Random Network Theory.

glass transition is explained by the existence of different bond angles and different bond lengths which imply a range of energy to break the cation-oxygen bonds. To

achieve a glass network, an oxide has to satisfy to four main rules:

1. The cation's coordination number has to be small (bonded to two or three oxygens).
2. An oxygen atom cannot be shared by more than two cations.
3. The polyhedra do not share their edges or faces; they are linked only by their vertices.
4. A polyhedron shares at least three vertices.

These conditions are fulfilled by some oxides of the formula MO_2, M_2O_3, and M_2O_5 and they are able to give a glass on their own. These oxides are called *glass network formers*, or more commonly, *glass formers*. The most common glass formers are SiO_2, B_2O_3, P_2O_5, and GeO_2.

A few years after the publication of the random network theory, Warren *et al.* published numerous studies about the atomic density radial distributions function of mono-component (SiO_2 and B_2O_3 and multicomponent glasses) [48–52]. The results were interpreted according to Zacahriasen's theory, contributing to its popularity [38]. Nevertheless the random network theory was also subject to criticisms [53], and Zachariasen and Warren recognized the possible presence of small clusters or crystallites in glass. But they also mentioned that the clusters are of negligible size (7-10 Å) [50, 51, 54] which represents one or two unit cells. One of the main consequences of a random network should be an homogeneous structure of the glass with no phase separation [30]. But Porai-Koshits *et al.* had shown by transmission electron microscopy (TEM) that heterogeneity (i.e. phase separation) exists in many glass compositions and probably exists in many others [55, 56].

2.2.3 Dominance of the Random Network Theory

Both theories have numerous supporters and disparagers who published various studies to defend their points of view. However, the random network theory dominates the world of glass science, and the reason does not come only from scientific facts. The

crystallite hypothesis officially started with Lebedev in the early 1920s, and it was mainly supported by German and Russian authors including Weyl, Zernike, Prins, Porai-Koshits [57]. The random network theory on the other hand was developed and supported by american authors such as Zachariasen, Warren, and Cooper [57, 58]. With the domination of the United States in the scientific literature during the Cold War, adherents of the random network theories published many studies supporting it, and then this theory was accepted as the main theory of glass structure [57].

2.3 Role of the oxides

Only few oxides are able to give a glass on their own (mono-component glass). These oxides are called glass network formers and they fulfill the four rules given by Zachariasen. The most common glass former is the silicon dioxide. In this oxide, the silicon atom is in the center of a tetrahedron surrounded by four oxygen atoms. In its amorphous form the tetrahedra are randomly distributed according to Zachariasen's theory. All the oxygen atoms are shared between two tetrahedra.

Other oxides can be added into a glass to modify its properties without destroying the glass network. These oxides do not participate in the glass network but they modify its structure. They are called *glass network modifiers* or simply *glass modifiers*. Their use is as old as the discovery of glass by the fortuitous heating of a mixture of sand (silicon dioxide) with nitre (sodium carbonate) [6]. The addition of Na_2O in the SiO_2 glass network breaks the $-O-Si-O-Si-O-$ chain into two smaller $-O-Si-O^-\ Na^+$ chains (see Figure 2.4). The sodium oxide transforms two bridging oxygens into two non-bridging oxygens. It breaks the long silicon-oxygen chains into shorter ones, which gives rise to a decrease of the viscosity [30]. A second effect of the addition of sodium oxide into a silicate glass is to reduce the temperature of the liquidus: pure silicon dioxide melts at 1710°C but a SiO_2-NaO mixture of ratio 3:1 melts at only 800°C [32]. The maximum and minimum amounts

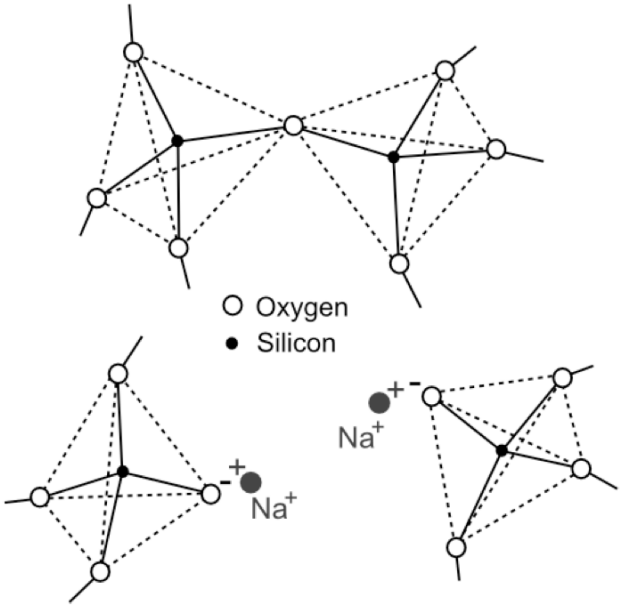

Figure 2.4: Action sodium oxide on a silicate chain. The Na^+ cation breaks the $Si - O - Si$ chains creating non-bridging oxygens

of modifier allowed in a glass without giving rise to a phenomenon of devitrification (crystallization) depend on the interactions between the elements constituent of the glass.

A third category regroups the oxides which can either participate in the glass network or act as an oxide modifier depending on their concentration or the presence of other compounds in the glass. These oxides are defined as *intermediate oxides*. A first example is the case of lead oxide which acts ionically at low concentration; and then enters into the glass network by creating covalent bonds when its concentration increases [59–61]. Another example is the case of BeO, MgO and ZnO which creates non-bridging oxygens when they are added into a glass; however, they can adopt a tetrahedral configuration and form covalent bonds if the glass already contains enough alkaline ions [30].

Sun's Single Bond Strength uses the cation-oxygen bond strength as an indicator of the inability of the atom to rearrange during the vitrification process [62]. From

this value, it is possible to assign each oxide into one of the three categories mentioned above (glass former, glass modifier, or intermediate oxide). The concept of intermediate oxide was originally introduced from this criterion [58], and they correspond to the oxide with a single bond strength in the range 250 - 330 kJ.mol^{-1}. Oxides with a higher bond strength are classified as glass formers, and oxides with a lower bond strength are classified as glass modifiers. However, Sun's criterion is limited to several oxides and it does not fit the case of chalcogenide glasses. These glasses have a single bond strength at values around 160 kJ.mol^{-1}. Some oxides are also exceptions to Sun's criterion such as CO_2 which cannot give a glass on its own, but it has a high single bond strength (about 500 kJ.mol^{-1}) [58]. Another criterion used to classify the oxides is Dietzel's Field Strength Criterion based on the electrostatic interaction between the cation and the oxygen [63]. The field strength F is given by:

$$F = \frac{Z_c}{(r_c + r_{o^{2-}})^2} \tag{2.1}$$

with Z_c as the cation's valence, r_c and $r_{o^{2-}}$ the ionic radius of the cation and oxygen respectively. According to this criterion, the glass network formers have a high field strength (from $\sim$1.3 to 2) and the glass network modifiers have a low field strength (from 0.1 to $\sim$0.4). Oxides with field strengths between these two ranges are considered as intermediates.

2.4 Glass network formers

In order to obtain a glass, at least one glass network former has to enter the composition. This oxide creates a network or a matrix in which other oxides will be integrated to modify the structure and properties of the glass and eventually also participate in the network. According to the random network theory, a glass is a random distribution of the unit polyhedron that forms the crystal of the same composition. In the next section of this chapter, theories of photoelasticity are described (section *3*

Photoelasticity) and their relationship with crystalline structure are also explained. Both theories are based on crystalline structures, and then they are extended to the case of glasses. Brief descriptions of the crystalline and glass structures of three common glass network formers (SiO_2, B_2O_3, and P_2O_5) are described in the following paragraphs with the aim to highlight the differences and similarities between the ordered and amorphous materials.

2.4.1 Silicon dioxide

Eleven polymorphs of silica SiO_2 are known (quartz, tridymite, cristobalite, coesite, stishovite for example), and they are all made of interconnected [SiO_4] tetrahedra [64]. The most common polymorph is the α-quartz and its structure was solved in the early 1920s with the emergence of X-ray diffraction techniques [65, 66]. The silicon atoms are in the center of a tetrahedron site and they are bonded to four oxygens at the vertices of the tetrahedron forming [SiO_4] units. Each oxygen is shared between two silicon atoms. The arrangement of the [SiO_4] units is different for each polymorph, but the unit itself remains unchanged. In a large majority of textbooks the structure of silica glass or amorphous silica (a-SiO_2) is taught as a random distribution of [SiO_4] units sharing at least three vertices, according to the random network theory. However, the exact structure of a-SiO_2 is still not solved and this remains a subject of active research mainly related to the emission of visible light by electroluminescence and photoluminescence discovered in the early 1990s [67]. Nevertheless, the $Si-O$ bond length, the oxygen - oxygen distance, and silicon - silicon distance have been determined at 1.61 Å, 2.62 Å, and 3.08 Å respectively [68, 69] The properties of amorphous silica revealed the existence of a medium range order, interpreted as a non-random correlation between neighboring [SiO_4] units in region of 5 to 50 Å [67]. Advances in theoretical and computational techniques also revealed the presence of four and three membered rings in a very small fraction ($\sim$1 at% Si) in the a-SiO_2 network [70, 71].

2.4.2 Boron trioxide

At normal pressure, crystalline boron trioxide B_2O_3 is made of plane [BO_3] triangles: three oxygen atoms form a triangle with a boron atom standing on its center [72–75]. The [BO_3] units are linked by their corners to create infinite chains oriented in three directions. The resulting structure corresponds to an hexagonal Bravais lattice [76]. In this BO_3 structural unit, the mean B-O bond length is 1.37 Å and the mean B-O-B bond angle is 120° [75]. In spite of this specific bond angle, [BO_3] units are not equilateral triangles, all three angles and bond lengths are slightly different. Also, the bond lengths and bond angles are not similar in all triangle units: two different [BO_3] units can be distinguished [75]. These differences are listed in Table 2.1. In

	Bond Lengths (Å)	
	BO_3(I)	*BO_3(II)*
$B-O_1$	1.404	1.401
$B-O_2$	1.337	1.336
$B-O_3$	1.366	1.380

	Bond Angles (^{o})	
	BO_3(I)	*BO_3(II)*
O_1-B-O_2	114.7	121.5
O_1-B-O_3	119.0	113.8
O_2-B-O_3	126.1	124.6

Table 2.1: Bond lengths and bond angles in [BO_3] triangles according to G.E. Gurr *et al.* [75]

its amorphous form, B_2O_3 is simply a random distribution of the planar [BO_3] units through a three-dimensional network [77]. Nevertheless, many structural units are found to be forming boroxol rings [78] which can contain up to six [BO_3] triangles [79]. Contrary to the silica glass, a large fraction of boron atoms are trapped in these rings ($\sim$ 80 at%) [80–83]. The discovery of these rings gave rise to intense discussion between supporters of the glass structure theories, but it was finally stated that these boroxol rings could not be termed crystallites and do not contribute to the creation

of order in the glass [84]. It should be mentioned that in pure amorphous B_2O_3 the boron atoms are found only in a planar triangle configuration, but the addition of cations in the glass network gives rise to the appearance of $[BO_4]^-$ tetrahedra, as in lead borate glass for example [59]. The boron atoms also adopt this tetra-coordinated configuration in pure boron trioxide glass under high pressure [85] with the tetrahedra sharing their edges. This configuration breaks the third rule given by Zachariasen (see section 2.2.2).

2.4.3 Phosphorus pentoxide

At least three forms of phosphorus pentoxide P_2O_5 are known: h-P_2O_5, o-P_2O_5 and o'-P_2O_5. Similarly to SiO_2 and B_2O_3, all these oxides are made of the same PO_4 tetrahedra [86–88]. For the three forms of phosphorus pentoxide, the bond lengths and bond angles inside the PO_4 unit are equivalent, only the arrangement of the tetrahedron is different. The values of the bond lengths and bond angles are listed in Table 2.2. In the h-form the PO_4 tetrahedron are associated in discrete P_4O_{10} molecules [86]. These molecules are made of four PO_4 and they can be described as tetrahedra of tetrahedra: each PO_4 share one bridging oxygen with the three other PO_4. The o-form has an orthorhombic lattice, it is made of helices of PO_4 tetrahedra, and each tetrahedra shares three corners with three adjacent helices [87, 89]. In this compound, the $P-O$ bonds are the less consistent with length varying from 1.562 Å to 1.583 Å. The third form of phosphorus pentoxide is the o'-form which consists of infinite layers built from six-membered rings of PO_4 tetrahedra linked by three corners [90]. It also has an orthorhombic lattice. Phosphorus pentoxide is often considered as the best glass network former due to its high field strength comparing to the other oxides [32, 58]. However its high hygroscopy makes it difficult to prepare and even more challenging to keep water-free during experiments and for long term storage. Similarly to silica and boron glasses, amorphous P_2O_5 (a-P_2O_5) and all phosphate glasses in general are made of a random distribution of PO_4 tetrahedra

	$P-O_T$ (Å)	$<P-O_B>$ (Å)	$<O\widehat{-P-}O>$ (degree)	$P\widehat{-O_B-}P$ (degree)	References
h-form	1.43	1.59	113.05	123	[86]
o-form	1.45	1.58	109.02	135.72 123.01	[87]
o'-form	1.44	1.57	109.64	143.7	[88]

Table 2.2: Bond lengths and bond angles in three different forms of P_2O_5

similar to the ones found in the crystal structures described above [91–95]. In a-P_2O_5 the tetrahedra share 3 corners, the $P-O$ bond lengths remains very similar to the bonds lengths found in the crystal structures. Bond lengths of the terminal oxygen and bond lengths the bridging oxygens remains very consistent in all three forms as shown in Table 2.2. An interesting characteristic of phosphate is the stability of the PO_4 tetrahedra with the addition of modifiers: no matter the amount and nature of modifier added to the glass, the phosphorus keeps a coordination four and the bond lengths and bond angles remain unchanged [96, 97].

Chapter 3

Photoelasticity

3.1 Mathematical nature of photoelasticity

The photoelasticity, also called *photoelastic effect* or *piezo-optic effect*, refers to an experimental method to determine the stress and strain distribution in transparent materials. The stress distribution can be observed using a polariscope that reveals

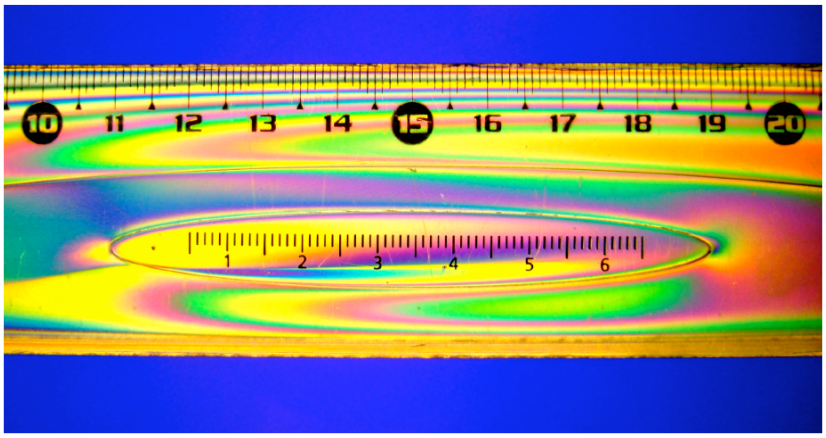

Figure 3.1: Stress distribution in a plastic ruler observed under polarized light.

the interferences of the light through the material which gives rise to fringes patterns [23]. From these patterns, a direct localization, and eventually quantification, of the stress in the material is possible as shown in Figure 3.1 and Appendix A. Different configurations of polariscopes were designed for different experiments, but they are all made essentially of linear polarizers and quarter-wave plates. The simplest configuration to measure the stress optic coefficient of a glass is to apply a uniaxial mechanical stress on a parallelepiped sample according to the Sénarmont method of compensation [22] (see section 4.1 for a complete description of this method). The mechanical stress is a second-rank tensor which in an arbitrary coordinate system is:

$$\sigma_{ij} = \begin{pmatrix} \sigma_{11} & \sigma_{12} & \sigma_{13} \\ \sigma_{21} & \sigma_{22} & \sigma_{23} \\ \sigma_{31} & \sigma_{32} & \sigma_{33} \end{pmatrix} (N.m^{-2}) \tag{3.1}$$

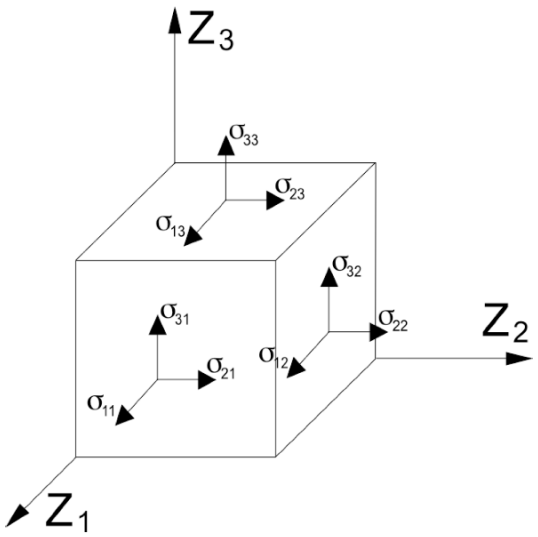

Figure 3.2: Stress components on a cubic piece of glass in a cartesian system of coordinates.

The first subscript refers to the direction of the strength and the second subscript refers to the axis normal to the face where the force is applied. The sample is not in

motion therefore the matrix has to be symmetrical ($\sigma_{ij} = \sigma_{ji}$) to satisfy the static equilibrium [98]. In the cartesian system of coordinates shown in Figure 3.2 the matrix can be simplified and the tensor form can be written with only six terms:

$$\begin{pmatrix} \sigma_{11} & \sigma_{12} & \sigma_{13} \\ \sigma_{12} & \sigma_{22} & \sigma_{23} \\ \sigma_{13} & \sigma_{23} & \sigma_{33} \end{pmatrix} = \begin{pmatrix} \sigma_{11} = \sigma_1 \\ \sigma_{22} = \sigma_2 \\ \sigma_{33} = \sigma_3 \\ \sigma_{23} = \sigma_4 \\ \sigma_{13} = \sigma_5 \\ \sigma_{12} = \sigma_6 \end{pmatrix} \tag{3.2}$$

In the case of a uniaxial mechanical stress parallel to the Z_3-axis as shown in Figure 3.3, the matrix and tensor are greatly simplified:

$$\begin{pmatrix} 0 & 0 & 0 \\ 0 & 0 & 0 \\ 0 & 0 & \sigma_{33} \end{pmatrix} = \begin{pmatrix} 0 \\ 0 \\ \sigma_3 \\ 0 \\ 0 \\ 0 \end{pmatrix} \tag{3.3}$$

The randomness of the glass structure induces the isotropy of the material: its physical properties, including the refractive index n, are the same in all directions. The application of an uniaxal mechanical stress σ_{33} on the glass breaks the isotropy which gives rise to the appearance of two different refractive indices: n_3 in the extraordinary direction (parallel to the stress) and n_1 in the ordinary direction (perpendicular to the stress) (see Figure 3.3). In a case where the refractive indices are different in the three directions Z_1, Z_2 and Z_3, they form an ellipsoid in the cartesian space called the indicatrix. The indicatrix is defined by:

$$\frac{x_{Z1}^2}{n_1^2} + \frac{x_{Z2}^2}{n_2^2} + \frac{x_{Z3}^2}{n_3^2} = 1 \tag{3.4}$$

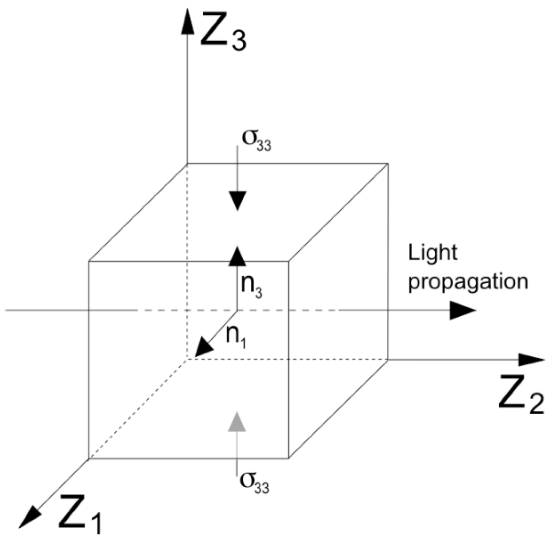

Figure 3.3: The application of a uniaxial mechanical stress gives rise to the appearance of an extraordinary refractive index n_3 in the direction of the stress and an ordinary refractive index n_1 in the direction normal to the stress.

Defining $B_i = 1/n_i^2$, Equation 3.4 can be written:

$$B_1 x_{Z1}^2 + B_2 x_{Z2}^2 + B_3 x_{Z3}^2 = 1 \tag{3.5}$$

and more generally:

$$\sum B_{ij} x_i x_j = 1 \tag{3.6}$$

In an unstressed homogenous glass, the value B_{ij} is the same in all directions, but the application of a stress changes the shape, size, and orientation of the indicatrix. This variation is given by:

$$\Delta B_{ij} = q_{ijkl} \sigma_{kl} \tag{3.7}$$

where q_{ijkl} is a fourth-rank tensor called the stress optic coefficient, it is given in Brewster which is an unit equivalent to 10^{-12} Pa^{-1} (or 1 MPa^{-1}). This coefficient quantifies the photoelastic effect and it is specific to each material. In the case of an homogenous glass, the isotropy induces a high symmetry and then the stress optic tensor can be simplified with only two independent stress optic coefficients q_{ijkl} [23]:

$q_{11} = q_{22} = q_{33}$

$q_{12} = q_{21} = q_{13} = q_{31} = q_{23} = q_{32}$

$q_{44} = q_{55} = q_{66} = (q_{11} - q_{12})$

With these two independent stress optic coefficients and only one stress component, Equation 3.7 can be solved to give the results [58]:

$$n_3 - n = -\frac{n^3}{2} q_{11} \sigma_{33} \tag{3.8}$$

$$n_1 - n = -\frac{n^3}{2} q_{12} \sigma_{33} \tag{3.9}$$

The birefringence Δn is defined as the difference between the extraordinary and ordinary refractive indices, here it is given by:

$$\Delta n = n_3 - n_1 = -\frac{n^3}{2}(q_{11} - q_{12})\sigma_{33} \tag{3.10}$$

By definition, the birefringence is also equal to the product of the mechanical stress with the stress optic coefficient [30]:

$$\Delta n = C\sigma_{33} \tag{3.11}$$

A relationship between the stress optic coefficient and the refractive index of the unstressed material is obtained by comparing 3.10 with 3.11:

$$C = -\frac{n^3}{2}(q_{11} - q_{12}) \tag{3.12}$$

The refractive index is wavelength dependent and this phenomenon is named *dispersion*, therefore the value of the stress optic coefficient also varies with the wavelength.

3.2 Birefringence

The phenomenon of birefringence exists in crystals with different lattice parameters. The most famous birefringent crystal is the calcite $CaCO_3$ (rhombohedral, a = 4.990 Å, c = 17.068 Å) [99]. This phenomenon comes from the existence of

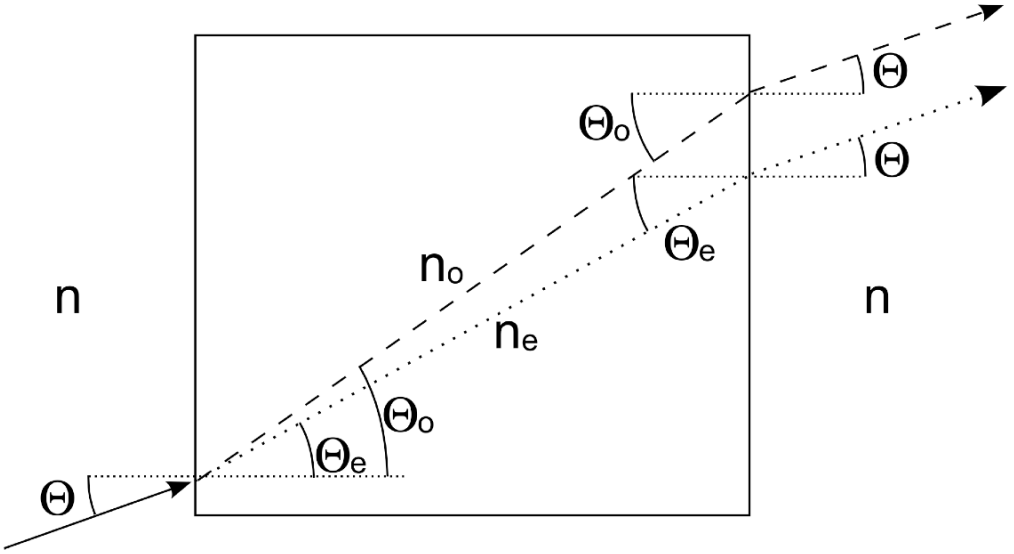

Figure 3.4: Optical path of the ordinary and extraordinary polarizations

two different refractive indices in the material, along the a- and c-axis in the crystal, and along the extraordinary and ordinary directions in the stressed glass. If an unpolarized light enters into the material, it is polarized along the two directions with different refractive indices n_1 and n_3. The two polarized waves travel through the material with two different velocities v according to the definition of the refractive index $n = c/v$ (with c the velocity of light in vacuum) and with two different refractive angles according to the Snell-Descartes Law of Optics.

$$n_a \sin\theta_a = n_b \sin\theta_b \tag{3.13}$$

The ordinary and extraordinary beams start to travel trough the material at the same point but emerge from it at two different positions as shown in Figure 3.4. The result is a double picture of the original object.

3.3 Theories of photoelasticity

3.3.1 Mueller's theory of photoelasticity

The main theory relating the structure and the photoelastic response of glass and crystals was published by Mueller in 1938 [26]. Before him, many authors attempted to explain the relationship between crystal structures and photoelasticity based mainly on the cases of two cubic crystals: KCl and NaCl [100–105]. Mueller worked on the structural origin of the photoelasticity in both cubic crystals [24] and amorphous materials [25] before writing a common theory for the two types of solids. In this last theory, known as the theory of photoelasticity, Mueller identified two effects contributing to the photoelastic response when a stress is applied to the material:

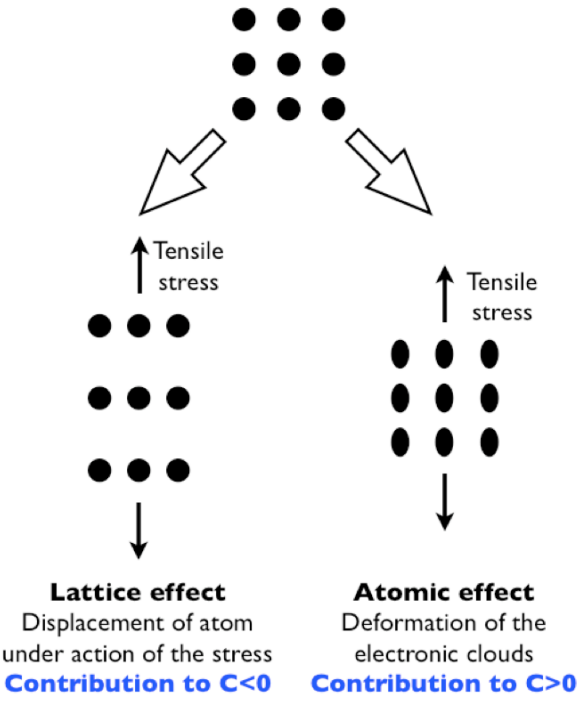

Figure 3.5: Lattice and atomic effects as described by Mueller [26].

1. The **lattice effect** which corresponds to the displacement of the atom in the structure.
2. The **atomic effect** which is the deformation of the electronic cloud.

According to Mueller, the lattice effect contributes to a negative value of the stress optic coefficient, whereas the atomic effect has a contribution to a positive value of the same coefficient. Furthermore the amplitude of the electronic effect is greater than the amplitude of the lattice effect. These two effects are illustrated in Figure 3.5. The case of a cation−oxygen chain is illustrated in Figure 3.6. Generally,

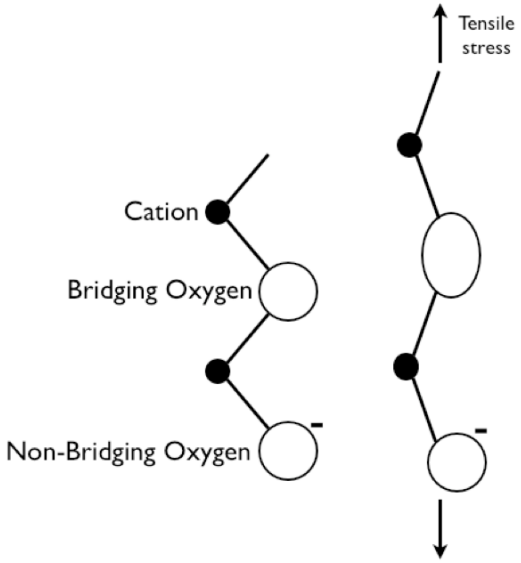

Figure 3.6: Effect of a tensile stress on a cation-oxygen chain. The bridging oxygen suffers a greater deformation than the non-bridging oxygens. Therefore, the bridging oxygens contribute to a positive stress-optic coefficient whereas the non-bridging oxygen's contribution is minimized according to Mueller's theory of photoelasticity.

the polarizability of the anions is greater than the polarizability of the cations, therefore the cations are assumed to be rigid. They are also considered to be bonded to only two oxygens for the purpose of the demonstration. The chain presented in the example contains a bridging and a non-bridging oxygen. When a tensile stress is

applied on the solid, the chain extends in the direction of the stress because of the high polarizability of the oxygen atoms. However, a bridging oxygen suffers a much greater deformation than a non-bridging oxygen [27]. According to Mueller's theory of photoelasticity, bridging oxygens greatly contribute to a positive stress optic coefficient whereas it is minimized in the case of non-bridging oxygens. Therefore, to decrease the value of the stress optic coefficient and to achieve a zero-stress optic glass, the number of non-bridging oxygens has to be maximized. These non-bridging oxygens carry a negative charge which has to be compensated by the cation brought by the oxide modifiers added to the glass composition. It can be concluded that, according to Mueller's theory of photoelasticity, the value of the stress optic coefficient decreases when the cation added to the glass acts ionically (i.e. addition of cations that does not integrate the glass network).

3.3.2 The Zwanziger's empirical model

More recently, an empirical model that can predict the photoelastic response of a glass was discovered by Zwanziger *et al.* [106]. This model is based on the glass composition and the crystalline structure of its constituents:

$$\sum_i x_i \left(\frac{d}{N_c}\right)_i \approx 0.5 \ \mathring{A} \tag{3.14}$$

In this equation x_i is the molar fraction of the oxide i constituent of the glass, d is the cation-oxygen bond length and N_c the coordination number of the cation in compound i. If the sum over all components is equal to 0.5 Å the glass should have a stress optic coefficient C equal to 0 Brewster. A value less than 0.5 Å yields a positive stress optic coefficient and a value greater than 0.5 Å yields a negative stress optic coefficient. This model reveals that the d/N_c ratio brings valuable information about the contribution of each oxide to the photoelastic response of the glass. Thanks to this simple model, the zero-stress optic property of some binary glass systems were discovered such as $(SnO)_x$-$(P_2O_5)_{1-x}$, $(SnO)_x$-$(SiO_2)_{1-x}$, $(Sb_2O_3)_x$-$(B_2O_3)_{1-x}$ and

$(TeO_2)_x$-$(BaO)_{1-x}$ [106, 107]. From the work of Zwanziger *et al.*, it appears that even if this model can predict the possibility for a glass composition to present a zero-stress optic property, the prediction of the composition for a binary system is given with an accuracy of about 15% [106].

3.4 Photoelastic response of glass formers and effect of some additives

All glass made of pure network formers has a positive stress optic coefficient such as:

- SiO_2: 3.47 Brewsters [27]
- B_2O_3: 11 Brewsters [28]
- TeO_2: 0.64 Brewsters [107]

The stress optic coefficient for pure P_2O_5 can not be determined directly because of its high hygroscopic nature and its mechanical properties. Its tendency to absorb water makes its preparation and use for experiment quite challenging. P_2O_5 is a very soft glass and the application of a mechanical stress results in a plastic deformation which makes the measurement of the stress optic coefficient impossible. Other glass formers such has Sb_2O_3 and V_2O_5 are extremely difficult to prepare. Both can be synthesized by fast and ultra fast quenching methods, but only small pellets of glass can be obtained [108, 109]. No sample big enough for stress optic measurements can be prepared. To obtain a zero-stress optic glass, the stress optic coefficient can be decreased by the addition of glass network modifiers. In the early 1980s Matusita *et al.* published a list of stress optic coefficients for binary silicate, borate and phosphate systems [27–29]. From this work it appears that alkaline oxides M_2O (M = Li, Na, and K) and alkaline-earth oxides MO (M = Mg, Ca, Sr, and Ba) are able to decrease significantly the stress optic coefficients of any glass. However, their effect is not sufficient to turn the coefficient into negative values and their ionic nature degrades the glass network, therefore they can be added only in small amounts to avoid a

devitrification of the glass.

So far, only five oxides are known to give negative stress optic properties to a glass. The best and most famous oxide is the lead oxide PbO. Its effect on the photoelastic response was discovered by Pockels in lead containing silicate glasses [16]. PbO provides high transparency in the visible range and a high refractive index. It also has the property of being a *pseudo-glass network former*. It cannot give a glass on its own, but the addition of a small amount of SiO_2 ($\sim$8 wt%) is sufficient to form a glass network [32]. A new European environmental regulation, the *Restriction of Hazardous Substances* [19], forbids the use of six substances in material including Hexavalent chromium (Cr^{6+}), Polybrominated biphenyls (PBB), Polybrominated diphenyl ether (PBDE), lead, cadmium, and mercury. Lead oxide is broadly used to produce Pockels' glasses, the challenge is now to find new glass compositions combining the same properties as the lead-containing glass: zero-stress optic, high index of refraction, high transparency in the visible range, good chemical durability, and no coloration.

As a rule of thumb, it is known that heavy elements bring high refractive indices in glass, therefore the best chance to obtain a zero-stress optic glass with a similar refraction as lead-containing glasses is to use the elements close to it in the periodic table. Its direct neighbors are thallium and bismuth, their d/N_c ratios are 0.84 Å for Tl_2O and 0.55 Å for Bi_2O_3. This ratio is much greater than the ratio for lead oxide (0.58 Å) in the case of thallium oxide, and similar to the ratio for the bismuth oxide which makes them good candidates to substitute lead oxide. Rabukhin *et al.* demonstrated experimentally that Bi_2O_3 can achieve zero-stress optic glass [21], but its addition in a small quantity greatly degrades the transparency of the glass which becomes dark brown. Thallium oxide Tl_2O seems to have some potential to generate zero-stress optic properties [20], but its high toxicity, like all thallium compounds, makes it a dangerous product that has to be handled with extreme care. Also in the binary lead silicate glass, the zero-stress optic composition is found at about 75 wt-% PbO. It can be expected that the need in Tl_2O for the same result would be

in this range of composition. The substitution of a hazardous compound by another with an extremely high toxicity does not seem to be the optimal solution to solve the problem. However, the synthesis of thallium-containing glasses could be of great scientific interest to understand the origin of the photoelastic response. No such glasses were prepared and presented in this thesis, but it remains an eventual field of investigation for future projects.

Antimony trioxide Sb_2O_3 and tin oxide SnO are both oxides containing cations from the fifth period of the periodic table. Zwanziger et al. [106] demonstrated that antimony trioxide can turn the stress optic coefficient into negative values in the case of the binary borate glass system $(Sb_2O_3)_x$-$(B_2O_3)_{1-x}$. This new family of zero-stress optic glass was discovered with the help of the empirical model, but the compositions of the zero-stress optic glass predicted by the model and the experimental results are quite different: $x = 0.20$ and $x = 0.43$ respectively. An hypothesis to explain this difference is the oxidation of antimony: the samples were prepared in air, but the antimony(III) trioxide is partially oxidized into antimony(V) pentoxide Sb_2O_5 when heated over 800°C [110]. The contribution to a negative stress optic coefficient for some antimony (Sb(III) $d/N_c = 0.63$ Å) changes for a contribution to a positive stress optic coefficient (Sb(V) $d/N_c = 0.30$ Å). Therefore, the overall effect of the antimony is lowered and more Sb_2O_3 is required. This can be an explanation to the difference between the experiment and the theoretical prediction, but a deeper investigation has to be done to know exactly the reason of this difference. In order to avoid the antimony(III)'s oxidation, its use should be performed under O_2-free atmosphere. At high content, Sb_2O_3 brings a yellow color to the glass, therefore it cannot pretend to completely substitute PbO. Nevertheless, pure amorphous Sb_2O_3 has a refractive index of 2.09 [108]. An addition of antimony to the glass composition in moderate amount can help to decrease the stress optic coefficient and increase the refractive index. It is interesting to note that the addition of Sb_2O_3 decreases the stress optic coefficient in the antimony borate glass [106]. Pure amorphous antimony trioxide can be assumed to be the only glass network former to have a negative stress optic

coefficient.

Tin oxide is probably the best additive suitable to substitute lead oxide. Its effect on the photoelastic response was observed in the case of binary silicate and phosphate glasses [106]. This oxide does not generate any absorption in the visible range and it also increases the refractive index. However, at high temperature SnO is oxidized into SnO_2 which contributes to increase the stress optic coefficient and degrades the absorption in the visible range. Therefore, all tin-containing glasses have to be prepared under O_2-free atmosphere.

One more oxide has a contribution strong enough to decrease the stress optic coefficient into negative values. Barium oxide has been used in the case of the binary system $(BaO)_x$-$(TeO_2)_{1-x}$ to achieve a zero-stress optic glass for $x = 0.17$ [107]. Previous works by Matusita clearly demonstrated that barium oxide added to borate or phosphate glass decreases the stress optic coefficient, but the limit of the vitreous compositions in these two cases was not established [28, 29]. An extrapolation of the data obtained by Matusita *et al.* suggests that a zero-stress optic glass could be achieved for $x_{BaO} \approx 0.56$ in the borate glass and $x_{BaO} \approx 0.63$ in the phosphate glass. A barium borate glass with a content of BaO of 60 mol-% can be prepared which means a zero-stress optic glass might be possible for this system. The limit in BaO in the barium phosphate glass seems to also be 60 mol-% [112]. Therefore, a zero-stress optic glass might not be possible. In the case of the barium tellurate glass, the low amount of BaO required might come from the fact that TeO_2 is a glass former with a stress optic coefficient already close to zero (0.64 Brewsters). This glass system provides a good example of the additivity property of the photoelastic effect suggested by the empirical model (Equation 3.14).

Chapter 4

Experimental techniques

4.1 Stress optic measurement

The stress optic coefficients for all glass samples presented in this work was measured using the Sénarmont method [22], also known as the Friedel's method of compensation [23]. This experimental method is illustrated in Figure 4.1. The Sénarmont method actually measures the phase difference induced by the application of a stress on a glass sample, then this phase difference is used among other parameters to calculate the stress optic coefficient unique to the sample.

4.1.1 Description of the polariscope

The following section describes the different states of polarization of the light after each optic of the polariscope. This experiment is used to determine the phase difference induced by the stress applied on the glass sample. The derivation of each equation presented in this section is detailed in appendix A. First, an unpolarized light is sent through a linear polarizer whose polarizing axis is oriented at 45° with

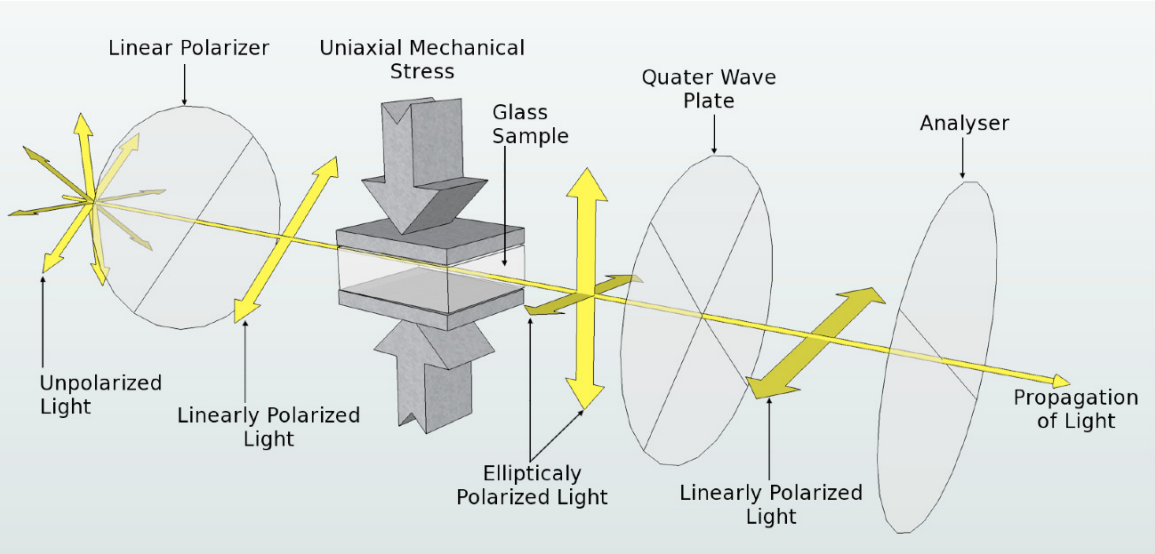

Figure 4.1: Representation of the experimental set-up used to measure the stress optic coefficient in glass according to the Sénarmont method.

respect to the direction of the uniaxial mechanical stress applied on the glass sample. The linearly polarized light emerging from the polarizer can be described by the following equation:

$$A_0 = asin(\omega t) \tag{4.1}$$

The light emerging from the polarizer is linearly polarized at 45° and passes through the glass sample. The uniaxial mechanical stress applied perpendicularly to the surface of the parallelepiped piece of glass breaks the isotropy of the glass, and creates two new refractive indices: one in the direction of the stress (extraordinary direction) and one in the direction perpendicular to the stress (ordinary directions). The existence of these different refractive indices has two effects on the light passing through the stressed sample:

1. The linearly polarized light is decomposed in two new linearly polarized light in the ordinary and extraordinary directions. At this stage, the two waves are

described by A_1 and A_2 in Figure 4.2. Their equations are:

$$\begin{cases} A_1 = A_0 \cos\frac{\pi}{4} = \frac{a}{\sqrt{2}} \sin(\omega t) \\ A_2 = A_0 \cos\frac{\pi}{4} = \frac{a}{\sqrt{2}} \sin(\omega t) \end{cases} \tag{4.2}$$

2. The two new linearly polarized light waves have the same frequency, but they are traveling through the glass sample with two different speeds because of the two different refractive indices. This difference of speed induces an angular phase difference α between the ordinary and extraordinary polarized waves emerging from the sample. The expressions A_1 and A_2 can now be described by A_3 and A_4 respectively:

$$\begin{cases} A_3 = \frac{a}{\sqrt{2}} \sin(\omega t) \\ A_4 = \frac{a}{\sqrt{2}} \sin(\omega t - \alpha) \end{cases} \tag{4.3}$$

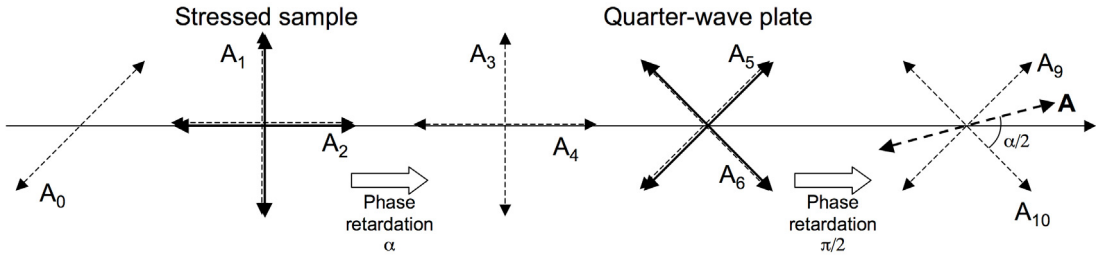

Figure 4.2: The different states of polarization along the polariscope

Here only A_4 suffers an angular phase retardation, but in an absolute way A_3 should also suffers an angular phase retardation. However, as said previously, α is the angular phase difference between the ordinary wave and the extraordinary wave, therefore α is required to appear only in one of the two equations. The two linearly polarized light emerging from the sample have the same amplitude but are not in phase. Their combination gives rise to an elliptical polarization as explained in appendix A, but in the special case of $\alpha = \pi/2$, their combination gives rise to a circular polarization. This new elliptical polarization passes through a quarter-wave

plate. The quarter-wave plate's slow and fast axis are oriented at 45° with respect to direction of the stress. Once again two phenomena occur:

1. The two waves described by the Equations A.3 are both polarized along the fast and slow axis. The new waves are now described by:

$$\begin{cases} A_5 = \frac{a}{2}[\sin(\omega t) + \sin(\omega t + \alpha] \\ A_6 = \frac{a}{2}[\sin(\omega t) - \sin(\omega t - \alpha)] \end{cases} \tag{4.4}$$

   But A_5 and A_6 can be written in a more convenient way.

$$\begin{cases} A_5 = a\cos(\omega t - \frac{\alpha}{2})\sin(\frac{\alpha}{2}) \\ A_6 = a\sin(\omega t - \frac{\alpha}{2})\cos(\frac{\alpha}{2}) \end{cases} \tag{4.5}$$

   (note: in appendix A, Equations 4.5 are called A_7 and A_8 to be able to differentiate the two states of polarization at this stage.)

2. A quarter wave plate is designed to create a phase difference of $\pi/2$ between the two waves polarized along the slow and fast axis. In the case presented here, the retardation is applied on the wave described by A_5. The new states of polarization A_5 and A_6 are now described by A_9 and A_{10}:

$$\begin{cases} A_9 = a\cos(\omega t - \frac{\alpha}{2} - \frac{\pi}{2})\sin(\frac{\alpha}{2}) \\ A_{10} = a\sin(\omega t - \frac{\alpha}{2})\cos(\frac{\alpha}{2}) \end{cases} \tag{4.6}$$

$$\begin{cases} A_9 = a\sin(\omega t - \frac{\alpha}{2})\sin(\frac{\alpha}{2}) \\ A_{10} = a\sin(\omega t - \frac{\alpha}{2})\cos(\frac{\alpha}{2}) \end{cases} \tag{4.7}$$

The common part of A_9 and A_{10} can be named A:

$$A = a\sin(\omega t - \frac{\alpha}{2}) \tag{4.8}$$

and

$$\begin{cases} A_9 = A\sin(\frac{\alpha}{2}) \\ A_{10} = A\cos(\frac{\alpha}{2}) \end{cases} \tag{4.9}$$

A is a linear polarized light whose amplitude depends on the stress applied on the sample. A_9 and A_{10} are its projections in the cartesian system defined along the directions corresponding to the slow and fast axis of the quarter-wave plate.

A second linear polarizer placed after the quarter-wave plate is set up on a rotating stage. It is used as an analyzer. The intensity of the light is measured after this analyzer for different angles. When the polarizing axis of the analyzer is perpendicular to the direction of the linear polarized light A, the intensity is equal to zero (extinction). The orientation of the polarized light changes with the intensity of the stress, therefore the angle θ corresponding to the extinction for different amount of stress is recorded. This angle θ is equal to half the value of the angular phase difference α induced by the stress:

$$\theta = \frac{\alpha}{2} \tag{4.10}$$

This angle is used to calculate the stress optic coefficient unique to the sample.

4.1.2 Experiment

The stress optic coefficient was measured using two different devices both set up for the Sénarmont method of compensation. The simplest device is a PS-100 Polariscope (Strainoptics) operated manually (Figure 4.3 (a)). For this device the experiment is set up vertically. The polariscope is made of a light table equipped with a linear polarizer, and the quarter-wave plate and analyzer are both set up in an optics holder. The holder attached to a pole which allows the quarter wave plate and analyzer to

stand on top of the sample. The stressed sample is placed directly on top of the light table, between the first linear polarizer and the quarter-wave plate. With this polariscope the analyzer is rotated by hand, and the extinction in the stressed sample and corresponding angle are evaluated by eye.

The second device is a Varian Cary 5000 Spectrometer operated through a computer (Figure 4.3 (b)). The spectrometer measures the intensity of light for a full range of wavelength from near-UV (200 nm) to mid-IR (3300 nm). In this case the experiment is set up horizontally. All optics (linear polarizer, sample, quarter-wave plate, analyzer) are aligned in the dark chamber of the spectrometer. The analyzer is installed in a rotating stage controlled using a computer, its accuracy is estimated to be 0.1°. In both cases, spectrometer and light table, the stress is applied on the sample using a homemade loading stage equipped with a miniature load cell (model LC703-200, Omegadyne Inc.).

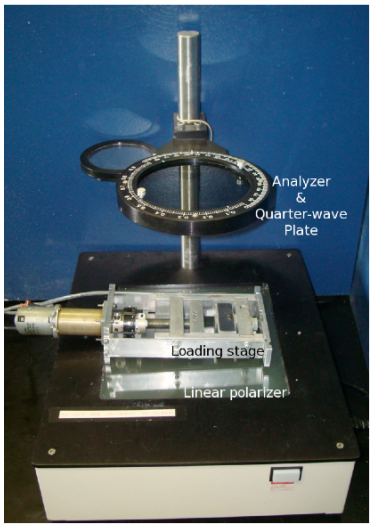

(a) PS-100 Polariscope, commonly called light table

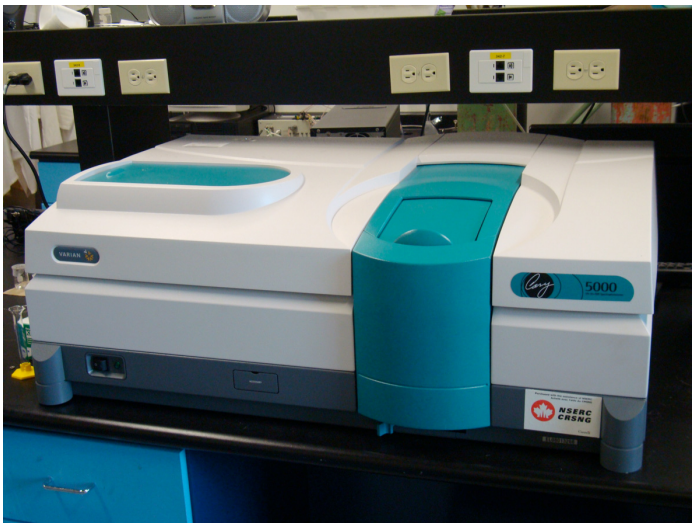

(b) Varian Cary 5000 Spectrometer. The optics and loading stage are installed in the chamber of the spectrometer. They are not visible on the picture.

Figure 4.3: Light Table and Varian Spectrometer used to measured the stress optic coefficient according to the Sénarmont method.

4.1.3 Determination of the stress optic coefficient

The stress optic coefficient can be calculated with the equation:

$$\delta_{PL} = C\sigma l \tag{4.11}$$

Where δ_{PL} is the effective path length difference (in nm), C is the stress optic coefficient (Brewsters), σ is the stress applied on the glass sample (Pa) and l is the optical path length or sample thickness (mm). The equation can be written as:

$$\frac{\delta_{PL}}{l} = C\sigma \tag{4.12}$$

The plot of δ/l versus σ gives a line, and the slope corresponds to the stress optic coefficient. The parameters δ_{PL}, σ and l can be determined experimentally. The effective path length difference δ_{PL} can be calculated from the angular phase difference α:

$$\delta_{PL} = \frac{\alpha\lambda}{2\pi} \tag{4.13}$$

In this expression α should be expressed in radian and λ is the wavelength of the light. The angular phase difference is measured by the Sénarmont method (Equation 4.10), the effective path length difference is then obtained according to the equation:

$$\delta_{PL} = \frac{\theta\lambda}{\pi} \tag{4.14}$$

The load cell used to apply the stress of the glass sample gives the weight applied on the sample in kilograms. The value of the stress can be obtained according to:

$$\sigma = \frac{Pg}{A} \tag{4.15}$$

P is the weight (kg), g is the gravitational acceleration (9.8 $m.s^{-2}$) and A is the surface of the sample on which the stress is applied (m^2). Finally the optical path length, which corresponds to the sample thickness, can be directly measured on the sample.

Experimentally, the angle θ corresponding to the extinction is measured for different pressures applied on the sample. The effective path length difference δ_{PL} and the corresponding stress σ are calculated, and then the stress optic coefficient C is calculated from the plot of Equation 4.12.

4.2 Nuclear Magnetic Resonance spectroscopy

In this section, a brief and simple description of the main mechanism of Nuclear Magnetic Resonance spectroscopy is presented. The purpose is not to detail all the experimental mechanisms or to derive the mathematical equations relative to NMR theory, but to provide the basic knowledge required to understand the experiments and results presented in this thesis.

4.2.1 Fundamental principles of Nuclear Magnetic Resonance

The spin properties of protons and neutrons in the nuclei combine to define the overall spin of the nucleus. If the atomic number (number of proton) and the atomic mass (sum of protons and neutrons) are even, the nucleus' spin quantum number I is equal to 0 and the nucleus has no magnetic properties. In this case it is invisible to NMR spectroscopy. For all other cases (the atomic number and/or atomic mass are odd) the nucleus has a quantum spin number I different from 0 and therefore has magnetic properties. The nucleus is then said to be spinning. Carbon 12 (^{12}C) and oxygen 16 (^{16}O) are common atoms in organic compounds, but both have an even atomic number and atomic mass. Substances containing non-active NMR elements can be doped with active isotopes such as ^{13}C or ^{17}O which have a much lower natural abundance (1.1% and 0.04% respectively) [113]. Some of the most common isotopes with a spherical nuclei are ^{1}H, ^{13}C, ^{15}N, ^{19}F, ^{29}Si and ^{31}P. They have a spin of 1/2. Non-spherical nuclei (ellipsoid shape) have a spin number I greater than 1/2 and are

called quadrupolar nuclei, they include ^{2}H, ^{11}B, ^{14}N, ^{17}O, ^{33}S and ^{35}Cl.

A spinning nucleus has a magnetic moment μ whose amplitude is given by the following equation:

$$\mu = \gamma \hbar I \tag{4.16}$$

The value γ is called the *magnetogyric* (or *gyromagnetic*) ratio and is specific to a given isotope and $\hbar$ is the reduced Planck's constant. In the absence of a magnetic field, all the same isotopes of a substance have a similar energy. If a strong external magnetic field $\overrightarrow{B_0}$ is applied along the z-axis in a cartesian coordinate system, the energy of the nuclei is splitted by the Zeeman effect. In the case of a spin 1/2, the magnetic moments slightly align in the direction of the field $\overrightarrow{B_0}$ (parallel) or in the opposite direction (anti-parallel). However, the magnetic moments μ are not perfectly aligned along the z-axis, they also have components along the x- and y-axis. The existence of these components generates a precessional motion of the magnetic moment around the z-axis with a specific angle to $\overrightarrow{B_0}$ and a specific angular frequency ω_0 called the Larmor frequency (rad.s^{-1}). This frequency ω_0 is proportional to the intensity of the applied magnetic field $\overrightarrow{B_0}$:

$$\omega_0 = \gamma B_0 \tag{4.17}$$

The Larmor frequency is preferably given in Hertz:

$$\nu_0 = \frac{\gamma B_0}{2\pi} \tag{4.18}$$

For a spin number $I = 1/2$ the two possible values of the directional quantum number m_I are $+1/2$ and $-1/2$ therefore only two precession motions are possible: with the field (oriented in the direction of $\overrightarrow{B_0}$ or +z corresponding to $m_I = +1/2$) or against the field (oriented in the direction -z corresponding to $m_I = -1/2$). The difference of energy ΔE between the two states $+1/2$ and $-1/2$ is given by the Boltzmann's distribution:

$$\frac{n_{(+\frac{1}{2})}}{n_{(-\frac{1}{2})}} = e^{\frac{\Delta E}{kT}} \tag{4.19}$$

The n values are the population of each state, k the Boltzmann's constant, and T the temperature (Kelvin). This energy difference can be related to the Larmor Frequency according to [114]:

$$\Delta E = \gamma \hbar B_0 \tag{4.20}$$

The two states $+1/2$ and $-1/2$ of energy are not equally populated, the state of lower energy is slightly more populated than the higher state. Therefore, a part of the magnetic moment of the lower state is not compensated. This gives rise to a *resulting magnetic moment* or *net magnetization* $\overrightarrow{M}$. The magnetic moment of the nuclei of the same isotope do not spin all together in a unique direction but they are distributed on a conical surface. As a result the net magnetization $\overrightarrow{M}$ is aligned along the z-axis.

This net magnetization exists only when an external magnetic field is applied. When this magnetic field is turned off, the magnetic moments μ of every nuclei progressively recover their initial orientation in a process of relaxation. The random distribution of these magnetic moments at the equilibrium reduces the net magnetization to zero. The time required for the net magnetization to disappear is called the *spin-lattice relaxation time* and is commonly written T_1.

The main purpose of the Nuclear Magnetic Resonance is to take advantage of this phenomenon of relaxation. An additional magnetic field $\overrightarrow{B_1}$ can be applied in a direction perpendicular to $\overrightarrow{B_0}$. It will affect the position of the net magnetization which will make an angle θ with the z-axis. According to $\overrightarrow{F} = \overrightarrow{M} \times \overrightarrow{B_1}$, the application of a magnetic field $\overrightarrow{B_1}$ perpendicular to the net magnetization $\overrightarrow{M}$ induces a strength perpendicular to both $\overrightarrow{M}$ and $\overrightarrow{B_1}$. If this field remains static, i.e. always applied in the same direction, the angle between the z-axis and the magnetic momentum μ of each nuclei will alternatively increase and decrease. To be effective, the field $\overrightarrow{B_1}$ has to rotate with an angular frequency ω. According to Equation 4.17 and Equation 4.20, a phenomenon of resonant absorption occurs when the frequency ω is equal to the Larmor Frequency ω_0, the energy provided by the field $\overrightarrow{B_1}$ matches the energy

difference ΔE between the two nuclear spin levels:

$$\Delta E = \hbar\omega_0 \tag{4.21}$$

At the resonance, under the effect of $\overrightarrow{B_1}$ spinning with the Larmor frequency, the net magnetization $\overrightarrow{M}$ deviates from its original position along the z-axis. The vector $\overrightarrow{M}$ has now x and y coordinates and also spin around the z-axis with a precessional motion. When the field $\overrightarrow{B_1}$ is turned off, the net magnetization comes back to its initial position along the z-axis. Because of its precessional motion, it describes a spiral in the (xy) plane. The oscillations of the magnetization along the x- and y-axis are recorded, and the NMR signal, or free induction decay (FID), is plotted (Figure 4.4). The time T_2 required for the net magnetization to come back along the z-axis is called *transverse relaxation time*. From the FID signal a Fourier transform generates an absorption Lorentzian function with the mathematical form [113]:

$$S(\omega) = \frac{\frac{1}{T_2}}{(\frac{1}{T_2})^2 + (\omega - \omega_0)^2} \tag{4.22}$$

The maximum of the peak generated occurs when $\omega = \omega_0$ and the peakwidth at half-height is equal to $2/T_2$ (rad.s^{-1}). Therefore a fast transverse relaxation gives rise to a broad peak and vice versa. NMR spectra can also be presented using a frequency scale ν ($\nu = \omega/(2\pi)$) in Hertz, in this case the peakwidth at half-height is given by $1/(\pi T_2)$ (Hz).

4.2.2 Chemical shielding and Chemical shift

The electrons surrounding the nucleus are charged particles in motion, they create a local magnetic field that affects the field "seen" by the nucleus. Depending on the shape and density of the electron cloud around the nucleus, the local magnetic field $\overrightarrow{B}_{local}$ affecting this nucleus can be expressed as $B_0(1-\sigma)$ where σ is the electronic modulation of $\overrightarrow{B_0}$ called "*shielding*". Taking into account this shielding,

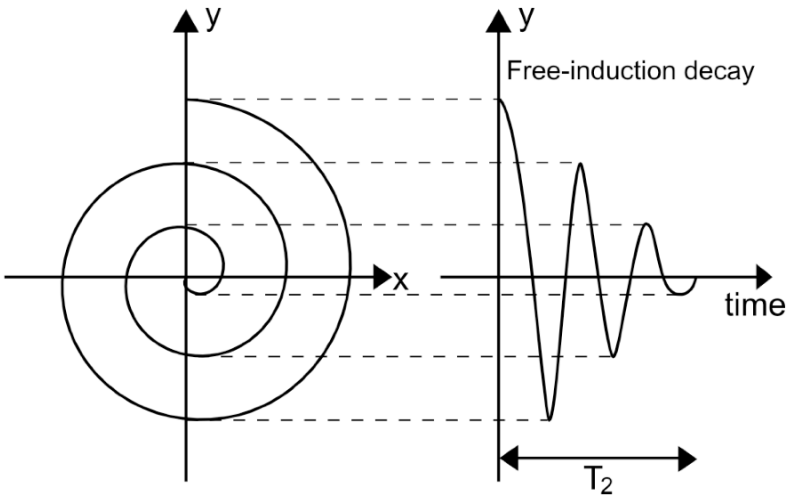

Figure 4.4: The Free Induction Decay (FID) is given by the oscillation of the components of the magnetization $\overrightarrow{M}$ along the x- or y-axis

.

the expression for the resonance frequency from Equation 4.18 becomes [115]:

$$\nu_0 = \frac{\gamma B_0(1-\sigma)}{2\pi} \tag{4.23}$$

However, in most of cases, the electron distribution around a nucleus in a molecule is not spherically symmetric. The intensity of the current, and therefore the intensity of the magnetic field induced by the electrons, is not uniformly distributed in space, and depends on the orientation of the molecule with respect to the applied field $\overrightarrow{B_0}$. Because of this spatial dependence, the shelding σ cannot be expressed as a single number, but as a Cartesian tensor represented by a 3 x 3 matrix:

$$\sigma = \begin{pmatrix} \sigma_{xx} & \sigma_{xy} & \sigma_{xz} \\ \sigma_{yx} & \sigma_{yy} & \sigma_{yz} \\ \sigma_{zx} & \sigma_{zy} & \sigma_{zz} \end{pmatrix} \tag{4.24}$$

In this matrix x, y and z correspond to the axis of the laboratory frame defined with the applied field $\overrightarrow{B_0}$ along the z-axis. It is also convenient to express the shielding tensor in a frame such as the matrix becomes diagonal. This frame is the *principal*

axis system (PAS), the terms of the tensor in this frame are expressed with the "PAS" superscript and the numbers along the diagonal σ_{xx}^{PAS}, σ_{yy}^{PAS} and σ_{zz}^{PAS} are the *principal values* of the shielding tensor. From the expression of the chemical shielding in the principal frame, three main values can be defined: the isotropic value σ_{iso}, the anisotropy Δ and the asymmetry η [116].

$$\sigma_{iso} = \frac{1}{3}(\sigma_{xx}^{PAS} + \sigma_{yy}^{PAS} + \sigma_{zz}^{PAS}) \tag{4.25}$$

$$\Delta = \sigma_{zz}^{PAS} - \sigma_{iso} \tag{4.26}$$

$$\eta = \frac{(\sigma_{zz}^{PAS} - \sigma_{yy}^{PAS})}{\sigma_{xx}^{PAS}} \tag{4.27}$$

NMR spectra are more often presented with results expressed in term of a *chemical shift* δ instead of chemical shielding. A substance of known structure is used as a reference to calibrate the spectrometer for a specific isotope. For example, tetramethylsilane $Si(CH_3)_4$ (TMS) is used as a reference for ^1H, ^{13}C and ^{29}Si NMR. H_3PO_4 can be used as a reference for ^{31}P NMR, and $BF_3.Et_2O$ for ^{11}B NMR. The resonance frequency ν_r for the reference is considered as the zero on the frequency scale and the frequency of the sample ν_i is measured with respect to this relative zero.

$$\nu_r = \frac{\gamma B_0(1 - \sigma_r)}{2\pi} \tag{4.28}$$

$$\nu_i = \frac{\gamma B_0(1 - \sigma_i)}{2\pi} \tag{4.29}$$

The relative resonance frequency of the sample with respect to the reference can be calculated:

$$\delta = \frac{\nu_i - \nu_r}{\nu_r} \tag{4.30}$$

The difference of frequency is expressed in Hertz whereas the frequency of the reference is expressed in megahertz, therefore the chemical shift δ is expressed in ppm.

According to Equations 4.23 and 4.30, the chemical shift is related to the chemical shielding.

$$\delta = \frac{\sigma_r - \sigma_i}{1 - \sigma_r} \tag{4.31}$$

Therefore the chemical shift can also be written as a tensor whose elements are expressed with respect to the chemical shielding tensor:

$$\delta_{ij} = \frac{\sigma_{ij}^{(ref)} - \sigma_{ij}^{(sample)}}{\sigma_{ij}^{(ref)}} \tag{4.32}$$

Although, the principal values of the chemical shift tensor are known, the orientation of the principal axis frame is not. The principal values are then labelled δ_{11}^{PAS}, δ_{22}^{PAS}, and δ_{33}^{PAS} with $\delta_{11}^{PAS} \geq \delta_{22}^{PAS} \geq \delta_{33}^{PAS}$. The isotropic chemical shift, chemical shift anisotropy Δ_{cs}, and the asymmetry η_{cs} are then defined by the following expressions [116]:

$$\delta_{iso} = \frac{1}{3}(\delta_{11}^{PAS} + \delta_{22}^{PAS} + \delta_{33}^{PAS}) \tag{4.33}$$

$$\Delta_{cs} = \delta_{11}^{PAS} - \delta_{iso} \tag{4.34}$$

$$\eta_{cs} = \frac{(\delta_{33}^{PAS} - \delta_{22}^{PAS})}{\delta_{11}^{PAS}} \tag{4.35}$$

4.2.3 Basis of solid-state NMR

The chemical shift anisotropy contributes to line broadening in the NMR spectra and it depends on the orientation of the molecules. In solutions, the molecules are free to move, and, as a result of this molecular tumbling, the measured chemical shift is the average of the shielding of a nucleus over all directions. In a solid, the orientation of a specific nucleus remains constant due to the rigid structure. As mentioned previously, in most cases the chemical shielding is not spherically distributed around the nucleus, therefore its effect on the local field $\overrightarrow{B}_{local}$ depends on the orientation

of the nucleus with respect to the field $\overrightarrow{B_0}$. As a result, a specific nucleus in a solid always experiences the same shielding. If the solid is a perfect crystal with all molecules oriented in the same direction, the chemical shift is the same for all nuclei in a given orientation, it is then possible to vary the chemical shift by rotating the crystal. In the case of a powder, each grain has a different orientation which implies that all nuclei does not see the same shielding. The result is a broad signal covering the range of possible chemical shifts in function of the orientation. The broadening of the peaks makes the determination of a specific chemical shift impossible. However, the shape of the spectrum depends on the principal values of the chemical shielding tensor and it can provide information about the overall geometry of the nuclei's sites.

The chemical shift anisotropy can be cancelled using the Magic Angle Spinning method (MAS). No derivation will be provided here but the chemical shift anisotropy depends on the mathematical term $3\ cos^2\theta_r - 1$ [113]. This term is equal to zero for the special angle $\theta_r = 54.74°$, called the magic angle. Spinning the sample around an axis at an angle θ_r from the applied field $\overrightarrow{B_0}$ will average the orientation of all nucleus similarly to the tumbling present in solution. The broad peak described above splits into narrow sidebands, but if the spinning frequency is high enough the spinning sidebands disappear to give a spectrum with well resolved peaks [113]. The case of P_2O_5 is illustrated in Figure 4.5.

4.3 Mössbauer Spectroscopy

Recoilless nuclear resonant absorption was accidentally observed for the first time in 1957 by Rudolph L. Mössbauer who gave his name to the experimental method [117]. This technique provides information about the local environment of specific isotopes in a solid which makes it perfectly suitable for the study of glass. Based on the absorption resonance of the nuclei, the nature of the data obtained by Mössbauer spectroscopy are very similar to the data obtained by NMR spectroscopy. Since the discovery of the Mössbauer effect, it became one of the most popular techniques in

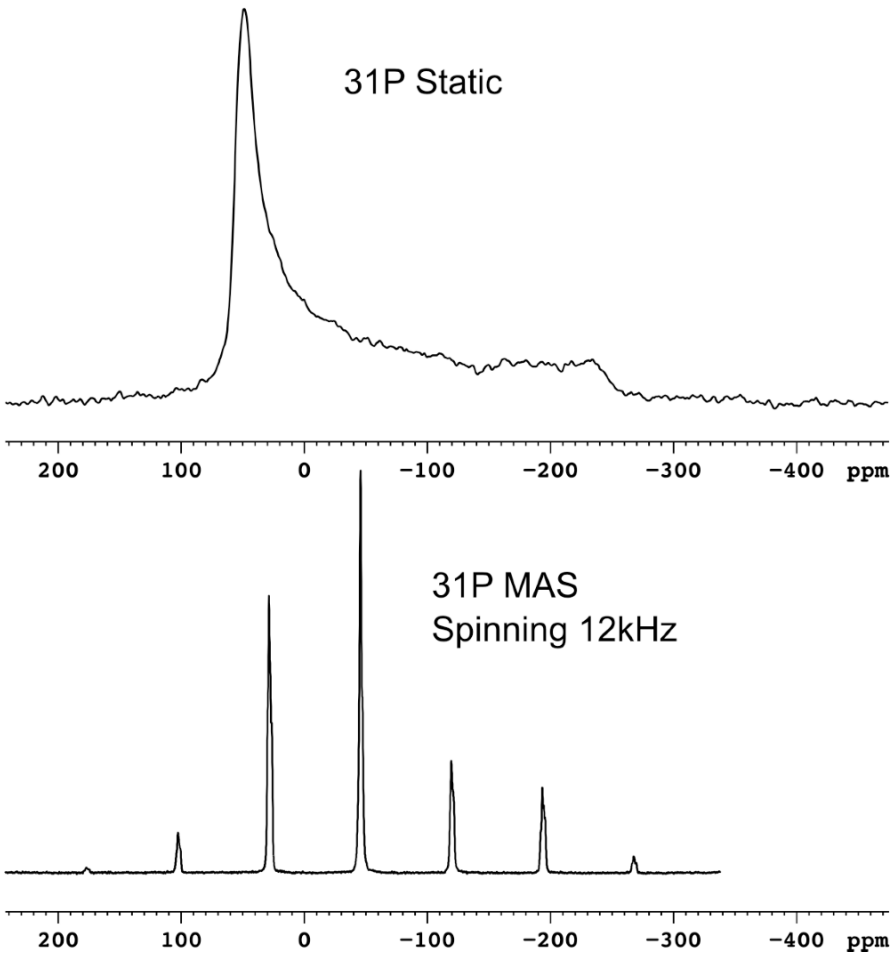

Figure 4.5: Static and MAS ^{31}P NMR spectra of P_2O_5

solid-state analysis. Its principle is briefly described in this section.

4.3.1 Isolated atom

In a first approach, an isolated atom of mass m in a gas phase is considered. This atom is in motion with a speed $\overrightarrow{V_x}$ along a unique direction x. Its kinetic energy is $\frac{1}{2}mV_x^2$. Similar to electrons, nuclei can be on different levels of energy. The difference of energy between the ground state and the excited state of the nucleus is noted E.

It is now possible to write the total energy of the system in motion with the nucleus in its excited state as $E + \frac{1}{2}mV_x^2$.

When it comes back to its ground state, the nucleus emits a photon in the range of energy corresponding to the γ-ray emission (around 10^{19} Hz). In an ideal case, the emitted photon carries the exact amount of energy E corresponding to the nuclear transition between the ground state and the first excited state. If the photon is absorbed by a similar nucleus, it gives rise to another transition from the ground state to the excited state. A photon of energy E is emitted again when the newly excited nucleus comes back to its ground state, and the phenomenon of resonance should occur indefinitely.

However, the emission of the photon gives rise to a recoil of the emitting atom similar to the recoil of a gun. To simplify the problem the emission of the photon is considered to be in the same direction x as the motion of the atom, and the speed $\overrightarrow{v}$ of the recoil is also along this direction. It should be mentioned that the value of $\overrightarrow{v}$ can be positive or negative depending on its orientation. After emission of the γ-ray the total energy of the system becomes $E_\gamma + \frac{1}{2}m(V_x + v)^2$.
By conservation of the energy, it is possible to write [118]:

$$E + \frac{1}{2}mV_x^2 = E_\gamma + \frac{1}{2}m(V_x + v)^2 \tag{4.36}$$

The energy of the photon emitted is given by:

$$\begin{aligned} E_\gamma &= E - \frac{1}{2}mv^2 - mvV_x \\ &= E - E_R - E_D \end{aligned} \tag{4.37}$$

Equation 4.37 shows that the energy of the photon emitted is degraded by a recoil energy E_R and by a thermal (or Doppler) energy E_D. Because of these two phenomenon the energy of the emitted photon is too low to allow the phenomenon of resonant absorption in another nucleus. Similarly to the recoil at the emission, another recoil occurs when the atom absorbs a photon. As a consequence, to give rise to a resonant absorption, the absorbed photon needs to provide the energy E for

the nuclear transition but also additional energy to compensate the recoil energy E_R and the Doppler energy E_D. The statistical energy distribution of the emited pho-

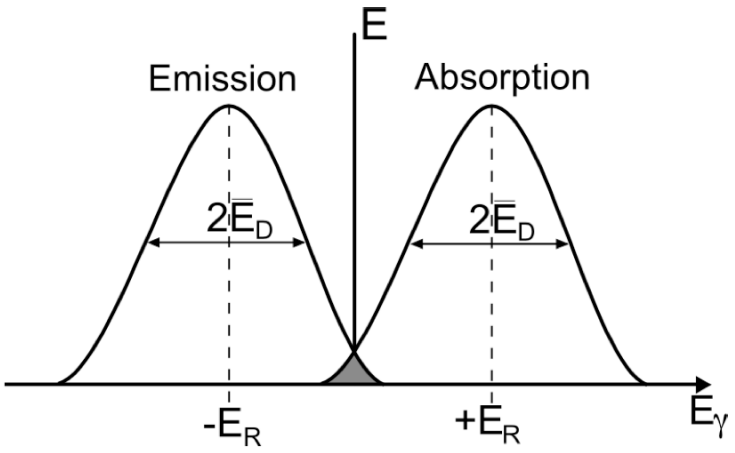

Figure 4.6: Gaussian distributions for the emission and the absorption of a photon.

.

ton and the statistical energy distribution of the absorbed photon both correspond to a gaussian distribution as shown in Figure 4.6. The emission energy is shifted by a value of $-E_R$ with respect to the transition energy E, whereas the absorption energy requires an additional energy $+E_R$. Both shifts are related to the recoil. The full-width at half height is proportional to the mean thermal energy $\bar{E}_D$. Nuclear resonant absorption has a significant probability to occur if the emission and absorption energy are close to each other, that is to say when the gaussian distributions for emission and absorption presented in Figure 4.6 strongly overlap.

4.3.2 The Mössbauer effect

The recoil due to absorption or emission of a photon can be greatly reduced in the case of an atom in a rigid lattice. If the atom is part of a rigid lattice, the recoil energy can be transferred to the vibrational energy, in this case the γ-ray energy is still degraded. However, phonon energies are quantified and the energy transfer can

only take place in the case of integral multiples of $\hbar\omega$, with $\hbar$ the reduced Planck's constant and ω a vibrational frequency in an Einstein solid. If the recoil energy E_R is less than $\hbar\omega$, then either zero or one unit of vibrationnal energy can be transferred to the lattice. It is possible to determine a fraction f of γ-photons emitted with no transfer of recoil energy to the vibrational states of the lattice. This fraction f is called the *recoilless fraction* or *recoil-free fraction*, and it is given by the following equation [119]:

$$f = 1 - \frac{E_R}{\hbar\omega} \tag{4.38}$$

In the case of a recoil-free emission or absorption, the whole lattice (i.e. single crystal) recoils rather than the single nucleus. The recoil energy E_R and the mean thermal energy $\bar{E}_D$ can be calculated according to the equations [119]:

$$E_R = \frac{E_\gamma^2}{2mc^2} \tag{4.39}$$

$$\bar{E}_D \simeq E_\gamma \sqrt{\frac{kT}{mc^2}} \tag{4.40}$$

where k is the Boltzmann's constant, and T is the absolute temperature. Both energies depend on the reciprocal mass 1/M, therefore, in the case of a recoil-free phenomenon (recoil of the whole crystal), the energy distributions for emission and absorption are narrowed and centered on the transition state energy E, and they are strongly overlapping.

4.3.3 Mössbauer experiment

The energy for the resonant absorption depends on the local environment of the nucleus. If a nucleus of a given isotope emits a γ-photon, this photon has a specific energy, and it can be absorbed by the same isotope in an equivalent environment. Experimentally, a radioactive source containing the Mössbauer isotope is excited in order to produce γ-rays. An absorber (i.e. the sample) contains the same isotope as in the source. If the source and the absorber are made of the same material, the

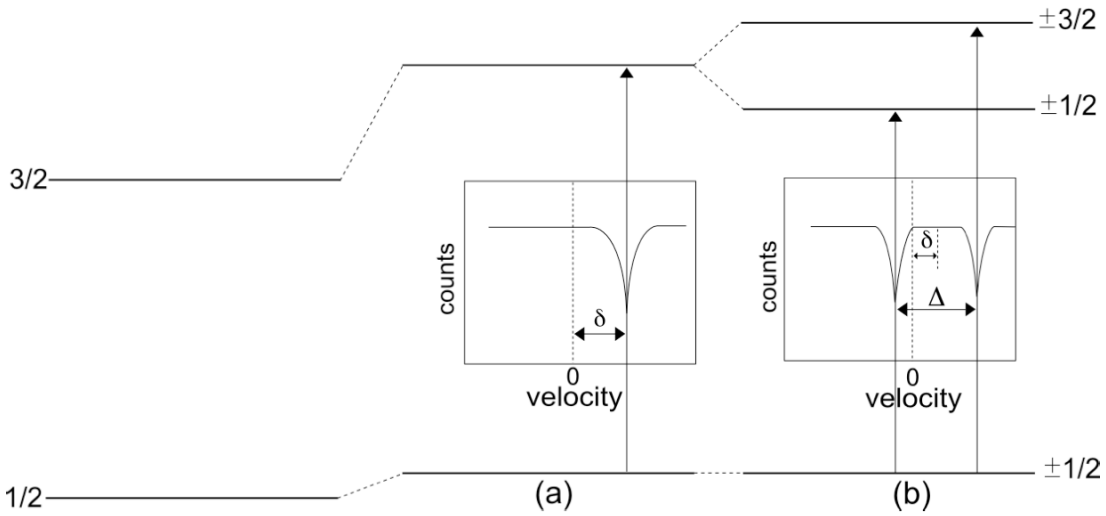

Figure 4.7: Energy level diagrams associated to the isomer shift (a) and to the quadrupole splitting (b)

Mössbauer nuclei are in the same environment and they emit and absord γ-rays of the same energy. If the environment of the Mössbauer nuclei is different in the absorber and in the source, the nuclei in the absorber do not absorb the γ-photons emitted by the source. The energy of the γ-rays emitted by the source needs to be modulated to correspond to the resonant energy of the absorber. This can be achieved by Doppler effect: a motion is applied on the source with a Doppler velocity v_D giving rise to an energy shift ϵ [119]:

$$\frac{v_D}{c} = \frac{\epsilon}{E_\gamma} \tag{4.41}$$

A spectrum giving the intensity of the γ-energy (in counts) versus the Doppler velocity (in mm.s^{-1}) is recorded. To be able to compare data from different absorbers, the origin of the velocity axis is usually determined using a standard absorber which depends on the Mössbauer isotope. In ^{119}Sn Mössbauer spectroscopy, $BaSnO_3$, $CaSnO_3$, or SnO_2 are usually used as a reference. The position of the absorption peak, and its eventual splitting, result from hyperfine interactions such as isomer shift and quadrupole splitting which are detailed in the next section.

4.3.4 Hyperfine interactions

Isomer shift

For the same isotope, the resonance absorption can be shifted depending on the actual environment of the nucleus. This shift results from two factors: the difference in the nuclear volume of the ground state and the excited state, and the difference between the electron densities at the Mössbauer nuclei in different materials [118]. It is known as *isomer shift*, *centre shift* or *chemical isomer shift* and is noted IS ($mm.s^{-1}$). In a system where the isomer shift is the only hyperfine interaction (spherical charge distribution, $I = 1/2$), the peak at the resonance absorption is a singlet as shown in Figure 4.7.a. However, because of the difference in the interactions occurring at the nucleus between the source and the absorber, the absorption in the sample takes place at a different energy then in the source. The emitted energy needs to be modulated by Doppler effect, as explained previously, and then the isomer shift corresponds to the Doppler velocity required to match the resonance energy of the absorber (see Figure 4.7.a). It should be kept in mind that the isomer shift is not an absolute value since the origin of the x-axis (Doppler velocity) is calibrated using a standard absorber specific for each isotope [118]. The isomer shift can be calculated according to [119]:

$$IS = \frac{c}{5E_\gamma \epsilon_0} Ze^2R^2 \frac{\delta R}{R}(|\Psi_{absorber}|^2 - |\Psi_{source}|^2) \tag{4.42}$$

with E_γ and c from Equation 4.41, ϵ_0 the permittivity of vacuum, Z the atomic number, e the elementary charge, R the radius of the nucleus and $|\Psi|^2$ is the electron density.

Quadrupole splitting

Nuclear states with a nuclear angular momentum quantum number $I > 1/2$ (non-spherical charge distributions) are characterized by a nuclear quadrupole moment.

If the nucleus is surrounded by an asymmetric electronic charge distribution, an electric quadrupole interaction occurs between this electronic charge distribution and the nuclear quadrupole moment. This gives rise to a splitting of the nuclear energy levels as shown in Figure 4.7.b. The quadrupole splitting QS ($mm.s^{-1}$) reflects the symmetry of the bonding environment in the vicinity of the Mössbauer atom [118, 120]. Information can be obtained by comparing the quadrupole splitting and isomer shift from different related materials. For example, values of both parameters obtained in glass can be compared to the values from crystalline compounds of known structure to determine structural information such as coordination number, geometry and bond length.

4.4 Density

The densities were obtained using the Archimedes' method. A density kit, made of a scoop and a scoop holder, is installed on a precision balance as shown in Figure 4.8. The holder is attached to the plate of the balance, and the piece made of two scoops is placed on top of it. The bottom scoop is low enough to be immersed in a liquid of known density ρ_{liquid}. The zero is made on the balance, then the sample is placed in the scoop A, the mass is recorded, and the zero on the balance is made again with the sample still in the scoop. Then the sample is placed in the scoop B, and the weight indicated by the balance is the buoyancy (negative value on the balance). The density of the sample is calculated according to the formula:

$$\rho = \frac{mass}{-buoyancy}\ \rho_{liquid} \tag{4.43}$$

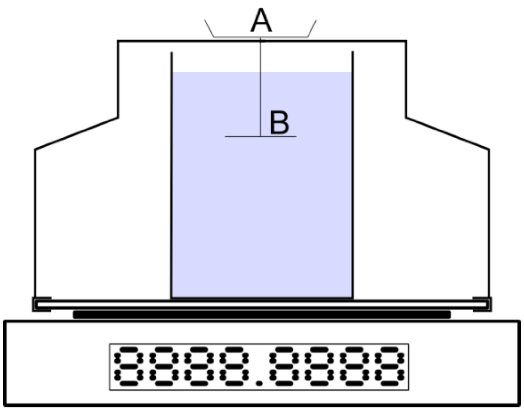

Figure 4.8: Sketch of the density measurement set-up.

4.5 Refractive index

The refractive index was measured on an Abbe refractometer (Atago DR-M4/1550) at 589 nm. In some cases, the refractive index was also measured at 486 nm and 656 nm. The optimal and maximum dimensions of a glass sample are 40 mm long and 8 mm wide. The smallest size acceptable for a sample is 15 mm long and 6 mm wide. Measurements on an Abbe refractometer are very accurate and the results can usually be given with four decimal places.

Chapter 5

Lead-containing glasses

5.1 Lead borate system $(PbO)_x$ - $(B_2O_3)_{1-x}$

(*The content of this section was published in the Journal of Non-Crystalline Solids* [121])

The structure of lead borate glasses has been extensively studied over the last few decades using Raman spectroscopy [122–125], ^{11}B and ^{207}Pb NMR [59, 126, 127] and X-Ray diffraction [127]. It is well known that the surrounding environments of boron and lead atoms undergo several modifications as the glass composition changes. This system also shows a large variation in photoelastic response as assessed through the stress optic coefficient. The purpose of the present contribution is to provide a rigorous test of Mueller's theory and Zwanziger's empirical model. The system chosen for study is lead borate glass, $(PbO)_x$-$(B_2O_3)_{1-x}$, in the range $0.35 \leq x \leq 0.65$. This range in sample composition exhibits a large variation in the environment and behavior of both the lead and boron cations.

5.1.1 Experiment

Glass preparation

All glass samples were prepared in platinum crucibles. Samples were synthesized from lead (II) oxide (litharge, 99+%, Strem Chemicals) and boron oxide (B_2O_3, 99%, Sigma-Aldrich). The powders were mixed in the crucibles and placed in a oven preheated to 300°C. The temperature was increased by 300°C every 15 min up to 900°C, and then increased by 200°C up to a maximum temperature of 1100°C for 15 minutes. The melts were quenched at room temperature on an aluminum plate and then immediately transferred over to another oven that was held at a temperature between 200°C and 450°C, depending on the composition of the glass and its respective glass transition temperature. The glasses were annealed between 350°C and 400°C. The molar fraction in lead oxide was verified by density measurement.

Density measurements

All sample density measurements were performed using Archimedes principle. The immersion liquid used was 99+mol% ethanol. Water was not used because of the hygroscopic character of the glasses, particular those with low lead content. Due to the slight variation of the density of ethanol depending on temperature, a series of values for the density of ethanol were taken from the literature [128].

Stress optic measurements

The stress optic coefficient of each sample was determined by the Sénarmont method of compensation described in section 4.1.

^{11}B NMR

All samples were crushed and packed in 2.5mm rotors. The ^{11}B magic angle spinning (MAS) NMR was performed on a Bruker Avance NMR spectrometer with a 16.4 T magnet (700 MHz proton Larmor frequency, 224.68 MHz ^{11}B Larmor frequency). The samples were spun at 10 and 22 kHz to determine center bands and to identify spinning sidebands. The $NaBH_4$ resonance served as a secondary chemical shift standard at -42.1 ppm relative to $BF_3.Et_2O$ and was used to determine the pulse power. For the ^{11}B MAS NMR spectrum 64 scans were accumulated using a pulse length of 0.4 μs at 78 kHz amplitude strength, chosen short for uniform excitation. Pulse repetition times between 1 s and 5 s were determined to be sufficient for these samples. Because of the substantial boron background, mostly from the rotors, the spectrum of an empty rotor was subtracted.

^{207}Pb NMR

All NMR experiments were carried out on a Bruker Avance NMR spectrometer with a 9.4 T magnet (400 MHz proton Larmor frequency, 83.7 MHz ^{207}Pb Larmor frequency) using a probe head for rotors of 4 mm diameter. The spectra were acquired on static samples, as spinning the sample did not enhance resolution. The spectra were acquired with a Hahn echo pulse sequence, using 90 degree pulses of 5.4 μs, 10.8 μs for the 180 degree pulses and 20 μs delay between the pulses. This delay was sufficient for the acquisition of a full echo. Relaxation times were estimated by successively increasing the repetition times. From these experiments a delay of 20 seconds was found to give the best signal-to-noise ratio per time. A total of 128 transients were accumulated. Spectra were processed with shifted Gaussian broadening, followed by magnitude calculation of the spectrum. In these experiments the spectral shape is determined by the pulse excitation profile, the probe quality factor and the intensity of the sample spectrum. To characterize the total spectral intensities, the excitation offsets of the spectra were shifted by 500 ppm successively until the full spectral

Fraction PbO	density (g cm^{-3})
0.35	4.62(7)
0.40	4.99(4)
0.45	5.36(6)
0.50	5.66(2)
0.55	6.02(2)
0.60	6.44(9)
0.65	6.49(2)

Table 5.1: Densities of the lead borate glasses

width was covered. To avoid excessive baseline noise due to these additions, the right and left baseline regions (30% on each side) were set to zero. The spectra presented are the sum of all the acquired sub-spectra. Chemical shift referencing was done with solid $Pb(NO_3)_2$ spinning the sample at 5.0 kHz at -3491 ppm. The temperature dependence of the chemical shift has been well characterized [129] and taken into account. Given the wide signal, this shift referencing is sufficient.

5.1.2 Results

Density measurements

The measured mass densities of the samples are collected in Table 5.1. These values agree to within about 1% with those obtained by interpolating the data reported by Feller and Affatigato [130], so we are confident that the glass compositions are reasonably close to the nominal values.

Stress optic results

The samples used for the present study were measured on a light table operated manually and on a spectrometer operated automatically by a computer. The values of the stress optic coefficient for each glass composition are presented in Figure 5.1.

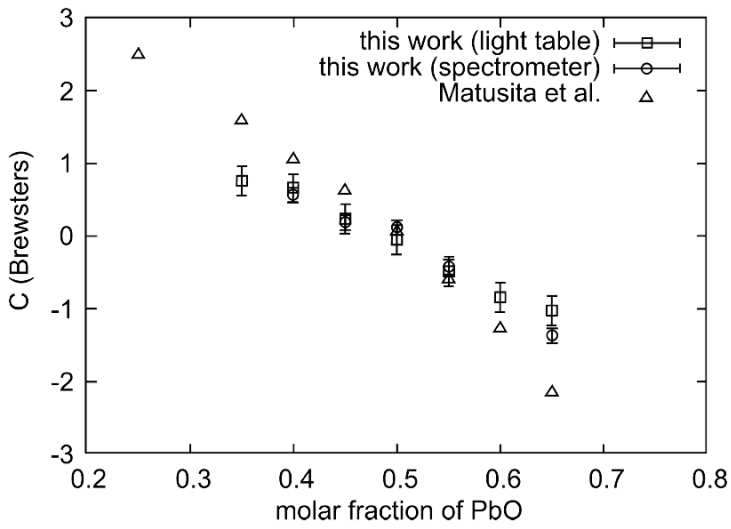

Figure 5.1: Evolution of the stress optic coefficient as a function of lead oxide content. Samples of the present work were measured on a light table and with a spectrophotometer using the Sénarmont method. Data from Matusita *et al.* [28] are shown for comparison.

As expected, the stress optic coefficient decreases as lead content increases, starting with positive values for low PbO content, giving a zero-stress optic composition at $x = 0.49$ and then ending with negative stress optic coefficient at high lead content. The values obtained by both methods here are very close, validating our results, but they show a significant difference in amplitude with Matusita's work [28]. The difference may come from the method used to measure the angular phase difference: in this work the Friedel's method of compensation is used whereas Matusita *et al.* determined the phase difference with a technique derived from the Tardy's method of compensation [23, 28]. In spite of the difference in slope from Matusita's results, the evolution of the stress optic coefficient with the composition follows the same trend in both cases, and the stress optic coefficient is equal to 0 Brewsters for a molar fraction in lead oxide of 0.49 for all three series of measurements.

^{11}B NMR

The ^{11}B NMR reveals the presence of 3-fold coordinated boron with a peak around 15 ppm and 4-fold coordinated boron with a peak at 0 ppm [131] in each of the spectra, as shown in Figure 5.2. Slight variations on the chemical shifts and peak

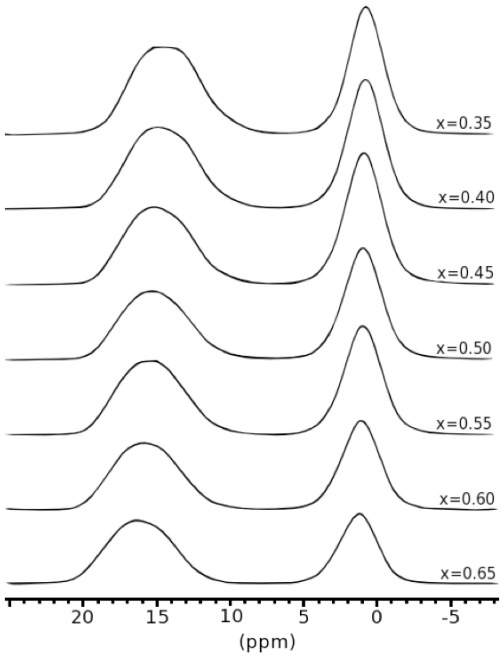

Figure 5.2: ^{11}B NMR spectrum for each sample in the range $0.35 \leq x \leq 0.65$. Peaks are detected around 15 ppm and 0 ppm characteristic of $[BO_3]$ units and $[BO_4]^-$ units respectively. A very small variation of the chemical shift is observed for both boron species.

widths are observed over the whole range of composition. The $[BO_3]$ peaks show both residual quadrupole coupling as well as the change from isolated $[BO_3]$ units to $[BO_3]$ units in six membered rings [79, 132]. The fractions of $[BO_3]$ and $[BO_4]^-$ units show variations with the composition. The areas of the well-separated peaks were integrated and the N_4 fractions were determined for each composition using data obtained at 22 kHz and including the spinning side bands. The N_4 fraction is

defined as the ratio of $[BO_4]^-$ units by the total number of boron units:

$$N_4 = \frac{[BO_4]^-}{[BO_4]^- + [BO_3]} \tag{5.1}$$

The results are reported in Figure 5.3. The number of 4-fold coordinated boron increases with increasing lead oxide content, and reaches a maximum at approximately $x = 0.5$. Following this point, the fraction of 4-fold coordinated boron decreases.

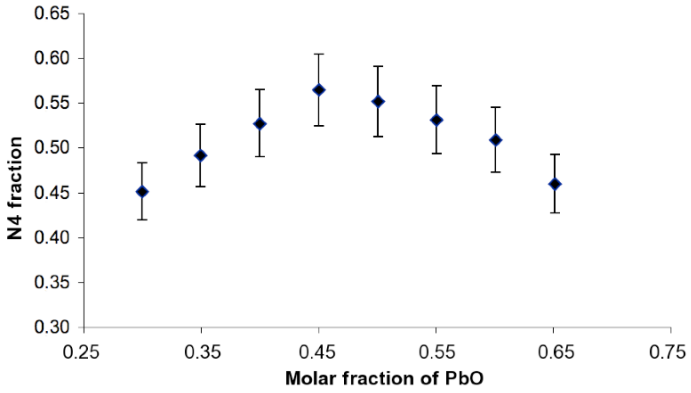

Figure 5.3: The evolution of the N_4 fraction as a function of lead oxide content. The fraction of 4-fold coordinated boron increases until a molar fraction of PbO of about 0.5 when the lead is entering the covalent network; then it decreases beyond this composition.

^{207}Pb NMR

^{207}Pb NMR spectra were obtained for 4 samples with molar fractions of 0.35, 0.45, 0.55 and 0.65 lead oxide (see Figure 5.4). For all samples, wide peaks typical of ^{207}Pb NMR spectra are observed, and the spectra show a clear evolution from a lower chemical shift to a higher chemical shift with increasing lead oxide. This observation is in good agreement with a previous study [134]. Each spectrum was decomposed into 2 or 3 gaussians and the chemical shifts and peak widths are reported in Table 5.2. At low PbO content ($x = 0.35$ and $x = 0.45$) only two peaks with low

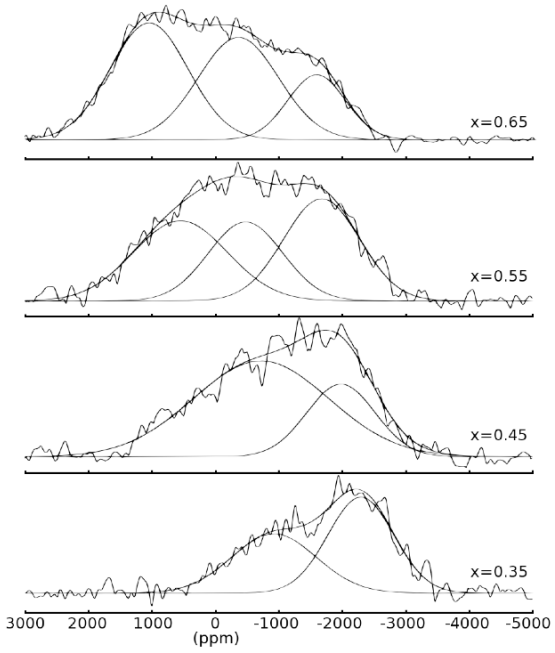

Figure 5.4: ^{207}Pb NMR spectra for samples at $x = 0.35$, 0.45, 0.55 and 0.65. The gaussians peaks used to fit each signal are also displayed.

chemical shift are necessary to fit the signal. A third peak appears at high lead content and the chemical shifts of all three peaks increase with lead content. The intensity of the peaks with the lowest chemical shift decrease with the increase of the molar fraction of PbO.

5.1.3 Discussion

The stress optic coefficient decreases significantly with increasing lead oxide content as in numerous lead containing oxide glasses [16, 20, 133], and the zero-stress optic glass has the composition of 49 mol-% PbO for all three series of measurements (see Figure 5.1). As an initial test of Equation 3.14, an estimate of the zero-stress-optic composition can be made using only the crystal structure values for bond length and coordination number, which corresponds to the original formulation of the model.

mol-% PbO	δ ppm, ±140	$\Delta\delta$ ppm, ±240	Area	N_c
0.65	-1569	1064	17.8	3-4
	-344	1482	39.0	3-4
	1056	1439	43.2	3
0.55	-1672	1410	36.6	4
	-475	1380	27.7	3-4
	553	1746	35.7	3
0.45	-1753	2452	24.4	6
	-138	1338	75.6	3-4
0.35	-2290	1223	55.8	6-7
	-921	1568	44.2	3-4

Table 5.2: Deconvolution of the ^{207}Pb NMR spectra (Figure 5.4). The spectra were fitted with two or three gaussians. The table columns list lead oxide content; chemical shift δ of gaussian; width $\Delta\delta$ of gaussian; relative area of gaussian; and assigned coordination number N_c of lead in the fitted resonance.

Using 1.366 Å and 3 for the B_2O_3 bond length and coordination numbers [75], and 2.309 Å and 4 for PbO [135], the model predicts zero-stress optic response at 37 mol-% PbO, in poor agreement with experiment.

As noted, the empirical model was proposed based solely on crystal structure data, which is reasonable when coordination numbers and bond lengths change little over the glass composition range. This assumption is broadly true in silicates and phosphates but not in borates. Indeed, the ^{11}B MAS NMR reveals the presence of both 3-fold coordinated boron and 4-fold coordinated boron as expected according to previous NMR studies of borate glasses [59,126,127]. Equation 3.14 suggests that the photoelastic response depends on the cations' coordination number and oxygen-cation bond lengths. Therefore, it is reasonable that the two different boron species have to be taken into consideration in order to predict the photoelastic response. Because the model is based on content of the different oxide compounds and x is the mol-% PbO, we use N_4 to weight the B_2O_3 contribution to photoelasticity as $(1-x)N_4$ as $[BO_4]^-$-like and $(1-x)(1-N_4)$ as $[BO_3]$-like.

The ^{207}Pb NMR spectra indicate that the lead environment evolves with composition as well. The signal at lower chemical shift in the ^{207}Pb NMR was assigned to the lead atoms with a high coordination number [134] and this coordination number was found to be 6 at low lead content ($x < 0.35$) [127, 136]. At high lead content the spectra are very similar to the signal obtained in lead silicate glasses $(PbO)_y$ - $(SiO_2)_{1-y}$ with $y > 0.60$ where the large broadening is characteristic of covalent PbO_3 and PbO_4 pyramidal units [137]. Furthermore, the presence of a Pb-O-Pb covalent network was observed by X-ray radial distribution function analysis only for samples with $x > 0.50$ and with a lead coordination number that has a minimum value of 3 for all compositions with $x > 0.75$ [127].

From these results it appears that the variation of the $[BO_4]^-$ results from of the evolution of the lead atoms. At low content, the lead behaves ionically, carrying two positive charges. Boron adopts a tetrahedral configuration $[BO_4]^-$ to balance the overall charge of the material. For $x > 0.50$, the lead starts to behave covalently, participating in the glass network and the amount of covalent lead increases with increasing PbO content while the amount of lead atoms that behaves ionically decreases. As a result the fraction of charge compensating $[BO_4]^-$ units decreases. In addition, it is possible that $[BO_3]$ units with one or more nonbridging oxygen begin to form at these compositions. The chemical shift and weight of each gaussian composing the lead spectra are presented in Table 5.2. From these chemical shifts it is possible to obtain an estimate of the Pb coordination number using the work of Fayon *et al.* [136]. This estimation is in good agreement with Takaishi *et al.* [127] who determined the average coordination number of lead and the Pb-O mean bond length in lead borate glasses by X-ray radial distribution function analysis.

In order to test whether the additional structural details on the lead and boron environments improves agreement of the stress-optic coefficient model with experiment, we re-write Equation 3.14 as

$$(1 - N_4)(1 - x)\frac{d(B_3)}{3} + (N_4)(1 - x)\frac{d(B_4)}{4} + x\frac{d(PbO)}{N_c(PbO)} = 0.5\mathring{A} \qquad (5.2)$$

where $d(B_3)$ and $d(B_4)$ are the B-O bond lengths in $]BO_3]$ and $[BO_4]^-$ units respectively, and $d(PbO)$ and $N_c(PbO)$ are the Pb-O mean bond length and average lead coordination number.

The structural data can be used in this model to various levels of detail. Ignoring all variations in coordination numbers and bond lengths gives the original crystal-based model of Equation 3.14. Next, one can use the NMR-based determinations of coordination numbers for boron and lead (Figure 5.3 and Table 5.2), together with crystallographically-derived bond lengths (1.366 Å for $[BO_3]$, 1.44 Å for $[BO_4]^-$, and 2.309 Å for PbO [75, 135, 138]). Finally, one can try to account for the variation in Pb-O bond length by incorporating Takaishi *et al.*'s results based on x-ray diffraction [127]. In that work, assignments of both N_c and d were made for different glass compositions, and can be correlated with a second order fit as:

$$d(PbO) \approx 0.054 N_c(PbO)^2 - 0.275 N_c(PbO) + 2.68. \tag{5.3}$$

These three approaches are plotted in Figure 5.5. Based on this plot, a series of revised estimates for the zero-stress optic composition may be made and compared with experiment. This comparison is made in Table 5.3, where it is seen that both methods of including detailed structural variation around the boron and lead sites lead to greatly improved agreement with experiment. This finding is significant because it shows that the empirical model based on bond lengths and coordination numbers captures the majority of the physics giving rise to photoelasticity in an oxide glass. In contrast to the above approach, according to Mueller's theory of photoelasticity a negative stress optic coefficient results from the presence of a large amount of non-bridging oxygen [26]. Therefore the cation from the glass network modifier should act ionically with these non-bridging oxygen. From Table 5.2 it appears that the amount of high coordinated lead atoms ($N_c \geq 6$) decreases with the increase of lead oxide. Highly coordinated lead are only present in the two samples at $x = 0.35$ and $x = 0.45$. The lead coordination number seems to remain consistent at high lead oxide content with a value between 3 and 4. Results from this work clearly

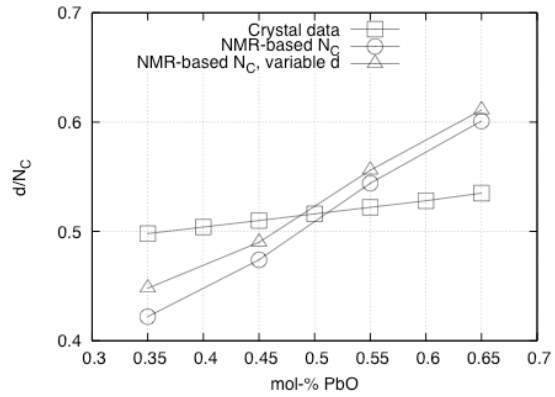

Figure 5.5: Results of the empirical model for three different cases: crystalline data only; NMR results (this work) introducing an estimation of the variation of the cation coordination number for each composition (bond length still constant); finally, coordination numbers from this work and also Pb-O bond lengths based on work of Takaishi [127].

Model	Prediction	Error
Crystal data	0.37	-25%
NMR-based N_c	0.48	-2%
Variation of d	0.46	-6%
Experiment	0.49	

Table 5.3: Predictions of the various implementations of the empirical model for zero-stress-optic composition with experiment. "Crystal data" means that only data from crystalline B_2O_3 and PbO were used; "NMR-based N_c" means that coordination numbers for B and Pb based on the current study were used, together with crystallographic bond lengths; and "Variation of d" means that in addition, the Pb-O bond length was estimated based on the NMR-based N_c and Takaishi's bond-length data [127].

show that the lead is acting covalently at high lead oxide content even while the stress optic coefficient is negative, in contrast to the prediction of Mueller's theory.

5.1.4 Conclusion

The empirical model recently introduced by Zwanziger et al. [106] is based on three parameters to determine the photoelastic response of a glass: the mole fraction, the cation coordination number, and the cation-oxygen bond length of each oxide constituents of the glass. This simple equation gives a result with a percentage of error of typically 10% in glasses such as silicates and phosphates. The error becomes significantly larger however in glasses like borates, where there are many non-linear structural variations. However, inclusion of local structural information on the variation of coordination number and bond length are shown to restore the accuracy of the model while retaining its simplicity and without introducing additional parameters. Unlike the theory of Mueller, the empirical model appears therefore to offer a robust tool for designing glasses with desired photoelastic response. It remains to investigate more fully the detailed physics of the underlying phenomena. For this task the Mueller theory may be a good starting point, but any theory should ultimately also provide some ability for compositional prediction and should be consistent with the present model.

5.2 Other glass systems

5.2.1 Lead silicate $(PbO)_x$ - $(SiO_2)_{1-x}$

Zero-stress optic properties were first discovered in lead-containing silicate glass. It is well known that the zero-stress optic glass occurs at $x = 0.45$ (75 wt-%) [16, 133]. Since the discovery of the Pockels' glasses, the role of Pb^{2+} in the lead silicate system has been investigated using various analytical methods, such as lead and silicon NMR, Raman spectroscopy, XPS experiments, X-ray diffraction, and neutron

diffraction [137, 139–149]. From the crystalline data of PbO ($Pb-O$ = 2.326 Å, N_c = 4 [135]) and SiO_2 ($Si-O$ = 1.609 Å, N_c = 4 [68, 69]), the empirical model predicts a zero-stress optic glass composition at $x = 0.56$, which gives an error of 24%. The structure of the lead silicate glasses is not fully understood because of the ambiguous behavior of the lead atoms. The silicon atoms remain in a constant environment no matter the amount of lead oxide in the glass. The Q^n species of silicon evolve from $n = 4$ to $n = 0$ with the increase of lead oxide in the composition [137,147–149]. The silicon dioxide acts as the main glass former up to $x = 0.60$, after which point the SiO_2 chains are being depolymerized, and only Q^1 and Q^0 silicon remains at high lead content, in the form of SiO_4^{4-} pyrosilicate and $Si_2O_7^{6-}$ orthosilicate. In the late 1990s, Fayon *et al.* investigated the lead silicate glass structure using ^{29}Si NMR, ^{207}Pb NMR, and Pb-L_{III} edge XAFS [137, 147] in the range of composition $0.31 \leq x \leq 0.73$. They demonstrated that through the whole range of compositions, the ^{207}Pb NMR static spectra show only large broadening signal with a strong chemical shift anisotropy and a positive isotropic chemical shift typical of a covalent behavior. At high content, the lead atoms are located at the apex of covalent [PbO_4] and [PbO_3] distorted pyramids. The ^{207}Pb NMR does not show any transitions from ionic to covalent nature as seen in the lead borate glass [137]. The XAFS experiment revealed the consistency of the $Pb-O$ bond length with constant values between 2.22 Å and 2.42 Å in the range $0.31 \leq x \leq 0.66$ [147].

X-ray and neutron diffraction were used by Takaishi *et al.* to investigate the local environment of the lead atoms in the range of composition $0.25 \leq x \leq 0.89$ [148]. The results from both diffraction methods gave similar results: the coordination number of the lead decreases from 6 to 3 with the increase of lead oxide in the composition, similarly to the lead borate system. The oxygen atoms around the Pb atoms are not all at the same distance: three oxygens are always at approximately 2.3 Å from the lead, whereas the additional oxygens are at about 2.8 Å. The shortest distance corresponds to the $Pb-O$ bond length of the [PbO_3] pyramidal unit; therefore, in agreement with the work of Fayon *et al.*, it can be said that the lead is on top of

a triangle based pyramid through the whole range of composition with additional oxygens from the surrounding [SiO_4] at low lead content. Nevertheless, the use of the bond lengths and coordination numbers given by Takaishi *et al.* in the empirical model improves the prediction of the zero-stress optic composition with a fraction of lead oxide at $x = 0.50$ (error = 11%).

A recent study involves various spectroscopic methods whose results can be compared to solve the structure of this glass system [149]. Time-of-flight mass spectrometry (MS-TOF) reveals the presence of Pb^{2+} ions in the glass at $x = 0.50$, but its amount decreases to finally not being detected at high lead content. In agreement with Takaishi *et al.*, this study states that the lead is acting as a glass network modifier at low content, and it creates its own glass network at high content ($x > 0.66$).

All the studies agree on the role and local structure of the silicon dioxide, which is always present as a [SiO_4] tetrahedron, that creates a three dimensional glass network at low and medium lead content ($x < 0.66$). The role of the lead atoms and their surrounding environments is more ambiguous. According to the most recent studies involving numerous spectroscopic methods, it appears that the lead's coordination number decreases from 6 to 3 with the increase of PbO. At low content, the lead is acting as a glass network modifier, but it becomes more and more covalent as its concentration increases, and finally it creates its own sub-network of [PbO_n] pyramidal units ($n = 3$ and 4) [149]. However, more investigations should be done to find out why the ionic lead is not visible on the static NMR spectra [137]. An evolution of coordination number from 6 to 3 should give clear changes of the average isotropic chemical shift and shape of the signal (CSA). In spite of the remaining uncertainty on the lead's nature at low content, all studies agree on the covalent character of the lead in glasses with high amounts of PbO, which also corresponds to the compositions with low and negative stress optic coefficients.

5.2.2 Lead phosphate $(PbO)_x$ - $(P_2O_5)_{1-x}$

Almost no data can be found in the literature about the photoelastic response of the lead phosphate binary glass system. Only two values of stress optic coefficients were reported for this system: $C = 0.35$ Brewsters at $x = 0.50$ [150], and $C = -0.59$ Brewsters at $x = 0.55$ [151]. Thanks to these two stress optic coefficients of opposite signs, it can be deduced that the zero-stress optic composition is in the range $0.50 \leq x \leq 0.55$. Based on the crystalline data of each oxide and the empirical model, the zero-stress optic composition is predicted to be at $x = 0.60$, which remains in the $\sim$15% error range usually observed in the results given by the model. It has been observed in all binary systems that the evolution of the stress optic coefficient always continuously increases or continuously decreases with the addition of a glass network modifier. Therefore it can be assumed that the addition of lead oxide in the phosphate glass decreases continuously the stress optic coefficient, similarly to the lead silicate and lead borate systems. In phosphate glasses, the coordination number of the phosphorus atoms and the $P - O$ mean bond length have the advantage of remaining constant throughout all glass compositions, with values 4 and 1.5 Å respectively [96,97,152]. This characteristic makes it easier the study of the structure of binary phosphate glasses. The environment of the lead atoms has been investigated using various spectroscopic methods, such as Raman and infrared spectroscopy [152], ^{207}Pb NMR [60,61], EXAFS [153] and X-ray diffraction [154]. All these studies agree on the same conclusions:

- The addition of lead oxide in the glass gives rise to a progressive depolymerization of the phosphate network.
- The addition of lead oxide gives rise to a decrease of the $Pb - O$ bond length.
- At low content, the lead acts ionically whereas at high content it acts more covalently (transition from a high to a low coordination number).

In spite of all the studies about this glass system, none of them provide quantified measurements of the bond lengths and coordination of the lead through the compositions, therefore no structural data of the glass can be used to see if the empirical model can provide an improved result. Similarly to the borate and silicate glasses, a positive stress optic coefficient is associated with an ionic lead, whereas a negative stress optic coefficient is associated with a covalent lead.

5.3 Summary

The investigation of the structural variations in the lead borate glasses revealed important modifications of the coordination and bond length of the lead atoms. These structural variations are correlated with the photoelastic response of the different glasses and it was observed that a lead acting ionically gives rise to a positive stress optic coefficient, whereas a covalent nature is associated to a negative stress optic coefficient. This correlation between the structure and the photoelastic response appears to be consistent in all lead glasses as determined from the literature in the silicate and phosphate glasses. Such a consistent correlation contradicts Mueller's theory of photoelasticity which cannot be considered as a general theory to interpret the structural origin of the photoelastic response in glasses.

On the other hand, the introduction of the structural variation in the Zwanziger's empirical model greatly improves the accuracy of the predictions.

Chapter 6

Tin-containing glasses

6.1 Tin phosphate system $(SnO)_x$ - $(P_2O_5)_{1-x}$

(*The content of this section was published in the International Journal of Applied Glass Science* [155])

In this section the tin phosphate system is investigated in detail. Phosphorus pentoxide, P_2O_5, is a strong glass former, and for all phosphate glasses the P atom is coordinated to four oxygen atoms in a tetrahedral geometry [91, 94, 95, 156, 157]. Furthermore, the $P-O$ mean bond length does not vary when a modifier is added, even when the number of bridging oxygens and non-bridging oxygens does not remain constant [96, 97, 158]. Therefore, in binary phosphate glasses, the d/N_c ratio for the phosphate component is always equal to 0.38 Å, and the difference between the prediction of the photoelastic response and the experimental values should only come from the contribution of the additive. Using data from crystalline SnO and P_2O_5, the zero-stress optic composition is predicted on the basis of Eq. 3.14 to occur at 69% SnO when in fact it occurs at about 56% [106].

The previous work on lead borate glasses showed that the discrepancy between

the empirically predicted composition and the experimental composition for a zero-stress optic composition could be attributed to structural variations (see section 5.1). In that study, however, the well-documented coordination change of boron was easy to measure; taking it into account gave excellent agreement between the corrected empirical value and the experiment. In the present case, the phosphate component is known to be structurally invariant, as mentioned above, therefore the evolution of the stress optic coefficient should be related to the composition and the structural variation of the tin's environment.

6.1.1 Experimental and Computational Methods

Glass preparation

Tin phosphate glasses were prepared from ammonium dihydrogen phosphate ($NH_4H_2PO_4$, Sigma-Aldrich, 98+%) and tin(II) oxide (SnO, Sigma-Aldrich, 10 micron powder, 99+%). The reagents were mixed in alumina crucibles and melted at 1050°C for 30 min under argon atmosphere to avoid the oxidation of tin(II) oxide to tin(IV) dioxide. The liquid was cooled between two brass plates at room temperature [106]. Chemical compositions were checked using energy dispersive spectroscopy (EDS), coupled with scanning electron microscopy (SEM) observation.

^{119}Sn Mössbauer spectroscopy

Room temperature ^{119}Sn Mössbauer effect spectra were obtained using a $Ca^{119m}SnO_3$ source and a Wissel System II Mössbauer spectrometer operating in constant acceleration mode. Center shifts were referenced to $CaSnO_3$ and the spectra were fitted with the *Recoil* software package [159]. For the Mössbauer experiment, the glass samples were ground under O_2-free atmosphere in a mortar.

^{31}P Nuclear Magnetic Resonance Spectroscopy

The ^{31}P NMR experiments were performed on a Bruker Avance NMR spectrometer with a 9.4 T magnet (162.02 MHz ^{31}P Larmor frequency) using a magic-angle spinning probe and 2.5 mm diameter sample rotors. The ^{31}P NMR chemical shift scale was referenced externally against $NH_4H_2PO_3$ at 0.81 ppm as a secondary reference. The 90 degree pulse time was also determined on this sample. The final 1-d magic-angle spinning spectra were acquired with a pulse of 0.75 μs (corresponding to a 20 degree flip angle) at 74 kHz rf field strength and 60 s recycle delay. Samples were spun at 25.0 kHz. Line shape simulations were performed using the program Dmfit [160] and XEDPLOT (Bruker software package).

Stress optic measurements

The stress optic coefficient of each samples was determined by the Sénarmont method of compensation described in section 4.1.

6.1.2 Computational Studies

The computational studies of several tin-phosphate crystals was performed by J.W. Zwanziger [155] Crystalline model compounds were studied using the ABINIT software package [161], using the projector-augmented wave (PAW) approach [162]. This code implements density functional theory to compute the electronic structure of a solid, using a planewave basis and pseudopotentials for the ionic cores. The PAW approach implements a mapping from the pseudo-wavefunctions in the valence space back to all-electron wavefunctions and thus recovers accuracy similar to all-electron codes but with much smaller basis sets [163]. The Mössbauer isomer shift and electric field gradients were computed using the PAW-derived electronic densities and reconstructing the all-electron values of these quantities [164–166]. This approach has been thoroughly tested in the ABINIT code for these ground-state quantities on

a variety of materials [164, 165].

6.1.3 Results

^{119}Sn Mössbauer spectroscopy

^{119}Sn Mössbauer spectra were obtained for glass compositions $(SnO)_x(P2O5)_{1-x}$ with $x = 0.42, 0.55, 0.66, 0.75$, and 0.86. Using the program *Recoil*, the spectra were fitted with doublets represented by Voigt-based functions utilizing Gaussian distributions of quadrupole splittings. The center shift distribution was assumed to be a linear function of the quadrupole splitting distribution. For the two glasses with the lowest content in tin oxide, a small peak was present at 0 mm.s^{-1}, which reveals the presence of tin dioxide, SnO_2, in the samples. The content of tin(IV) is estimated at 2.1% of the total tin content for $x = 0.42$ and 1.7% for $x = 0.55$ SnO respectively. Initially the spectra were fitted with one component for the site corresponding to SnO. The fits were good except at the base of the doublet where they were too narrow compared to the data. To solve this problem, another component was added and in this case the fits were much improved; final fits are shown in Figure 6.1.

x_{SnO}	Component 1			Component 2		
	IS	QS	Width	IS	QS	Width
0.42	+3.54(2)	1.23(1)	0.46(3)	+3.01(2)	4.64(6)	3.32(3)
0.55	+3.26(4)	1.55(2)	0.48(4)	+2.66(4)	6.07(5)	1.26(3)
0.66	+3.18(3)	1.59(2)	0.51(4)	+2.76(3)	5.61(3)	3.6(3)
0.75	+3.05(3)	1.88(1)	0.61(4)	+3.05(3)	2.30(2)	6.22(3)
0.86	+2.90(2)	1.91(1)	0.44(3)	+2.81(3)	3.87(5)	3.71(2)

Table 6.1: Isomer shift IS relative to SnO_2 , quadrupole splitting QS, and Gaussian width (all in units of mm.s^{-1}) for ^{119}Sn Mössbauer spectra of glasses with the given SnO content. Uncertainties in the last digit are given in parenthesis. In all cases the broad second component represents about 10% of the total intensity.

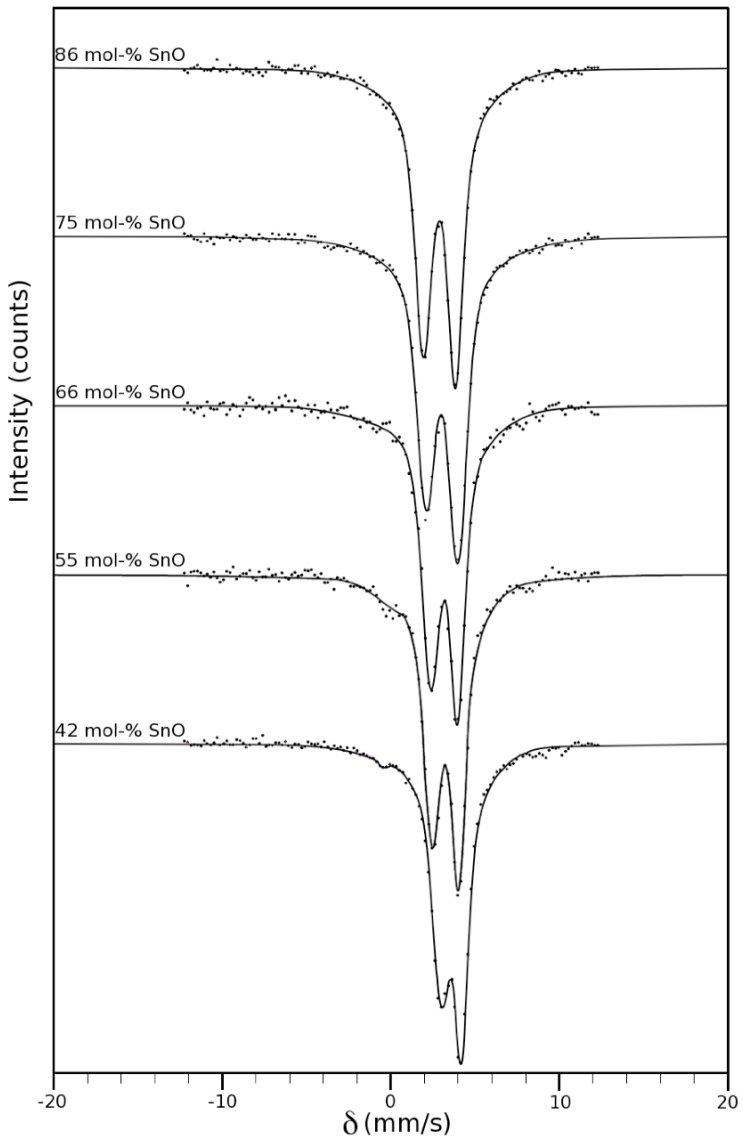

Figure 6.1: ^{119}SnMössbauer spectra of the $(SnO)_x$-$(P_2O_5)_{1-x}$

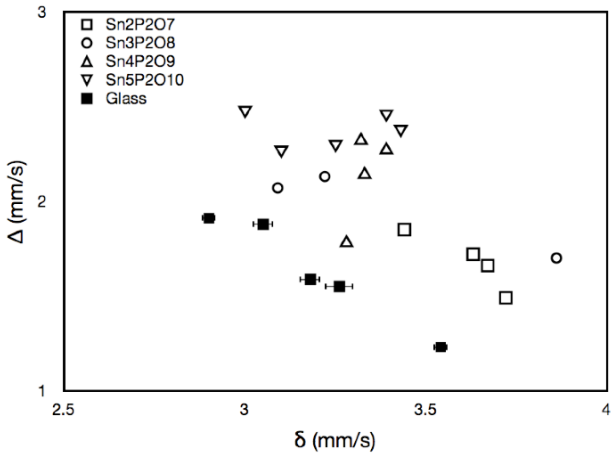

Figure 6.2: Correlation between the tin isomer shift and quadrupole splitting in various stannous phosphate compounds.

The mean center shift, quadrupole splitting and Gaussian width of the fitted resonances are reported in Table 6.1. For the two-component fit, the dominant component represents around 90% of the signal in all spectra. This component exhibits the same isomer shift and quadrupole splitting as the single-component fit. For the second components, each about 10% of the total intensity, the isomer shifts and quadrupole splitting evolved randomly with the composition, contrary to the dominant component, the values of which varied linearly with composition. More importantly, the weak second components are much wider than the dominant components, and in addition have slightly different isomer shifts and larger quadrupole splittings. A similar phenomenon was observed in the case of pure iron after mechanical grinding, and in that work the contribution of the second component was explained by the environment of the iron atoms at interfaces [169]. The grinding effect was also studied on tin dioxide and revealed its reduction due to the mechanical action [170]. Similarly the broad second component is interpreted here as due to surface effects, and will not be considered further in the discussion below. The results of computed ^{119}Sn Mössbauer parameters are compiled in table 6.2. In the

Compound	Site	Calc.		Expt.		$\bar{d}_c$	d_f
		IS	QS	IS	QS		
SnO_2 [171, 172]	1	0	0.52	0	0.499		
$Sn_2P_2O_7$ [173]	1	3.72	1.49			2.18	2.85
	2	3.63	1.72			2.16	3.00
	3	3.44	1.85			2.13	3.24
	4	3.67	1.66			2.14	3.15
$Sn_3P_2O_8$ [174, 175]	1	3.22	2.13	2.92	1.85	2.12	2.96
	2	3.09	2.07	2.92	1.85	2.10	3.05
	3	3.86	1.70	3.53	1.22	2.24	2.85
$Sn_4P_2O_9$ [176]	1	3.39	2.27			2.15	3.02
	2	3.33	2.14			2.15	2.75
	3	3.32	2.32			2.20	2.51
	4	3.28	1.78			2.12	2.98
$Sn_5P_2O_{10}$ [176]	1	3.39	2.46			2.20	2.51
	2	3.00	2.48			2.15	2.75
	3	3.43	2.38			2.17	2.84
	4	3.10	2.27			2.12	3.20
	5	3.25	2.30			2.15	2.75
SnO [172, 177]	1	2.78	1.40	2.678	1.36		

Table 6.2: Computed center shift and quadrupole splitting (calculated at 0, and measured isomer shifts and quadrupole splittings of several stannous crystals. The measurements at room temperature take into account the second-order Doppler effect.

literature, four tin phosphate crystal structures were found, including $Sn_2P_2O_7$ [173], $Sn_3P_2O_8$ [174], $Sn_4P_2O_9$ [176], and $Sn_5P_2O_{10}$ [176]. The latter two structures have open frameworks with large channels, and tin in quite uncommon trigonal planar geometries; we decided therefore to exclude these two structures from comparison with the glasses as their structures seem too unlike what is found in condensed amorphous systems. These data are plotted in Figure 6.2 as a correlation of quadrupole splitting QS as a function of isomer shift IS, together with the measured values for the glasses.

^{31}P NMR

The ^{31}P NMR spectra show the trends as were observed by Bekaert *et al.* and by Holland *et al.* [178,179]. The spectra show unresolved, but in most cases asymmetric lines, whose position shifts downfield with increasing tin content. Fits to two components for each spectrum also follow the known positions and trends for Q^0, Q^1, Q^2, and Q^3 peak positions, themselves shifting slightly down field with tin content, but staying within the known ranges [178]. We find Q^0 between -15 and -10 ppm, Q^1 between -20 and -23 ppm, Q^2 between -30 and -35 ppm, and Q^3 around -44 ppm. The fractions of the Q-species also follow the trends discussed previously based on charge balances, as here the Sn^{4+} contributions are small [178, 179].

Stress optic response

The stress optic response of the compositions studied here are listed in Table 6.3. Similarly to the lead oxide, an addition of SnO decreases the value of the stress optic coefficient. The zero-stress optic compositions is found at $x = 0.56$.

x_{SnO}	C (Brewsters)
0.55	0.2
0.60	-0.8
0.65	-1.3
0.75	-2.4

Table 6.3: Stress optic coefficient of the tin phosphate glasses.

6.1.4 Discussion

In order to use the empirical model to predict the zero stress optic coefficient, it is necessary to determine the bond lengths and coordination number around each

cation. For phosphorus, as discussed previously, this is simple, as the coordination number is exactly four and the bond lengths hardly vary in these coordination numbers. The ^{119}Sn Mössbauer spectra however show that the tin environment changes notably over the composition range studied, with the isomer shift changing from 3.54 mm.s^{-1} to 2.90 mm.s^{-1}. The computed and measured isomer shifts in crystal models summarized in Table 6.2 show very broadly a similar trend as SnO content is increased, though with some marked differences. Close inspection of the crystal structures cited for these studies shows that in all the tin phosphates, the tin atoms are closely bonded to three oxygens and more distantly to 1–3 more. The close distances range from 2.1 to 2.3 Å, while the longer distances range from 2.85 to 3.25 Å. The large shifts, as are found in the glasses at low SnO content, are found in the crystal sites when the three short bonds are at the long end of their range and the longer bonds are relatively short; this circumstance leads to the greatest total electron density at the tin site and hence the largest shift. The smallest shifts are associated with sites in which the three short bonds are all relatively short. It is important here to note that the range of the short bonds is small, while the range of the long bonds is large. Evidently a small decrease in the short bonds is not enough to compensate for a large increase in the long bonds, and the isomer shift decreases. The trend observed in the quadrupole splittings supports the above suggestion. Figure 6.2 shows a negative correlation between the quadrupole splittings and the isomer shifts, such that larger splittings are found in sites with smaller shifts and conversely. This trend is observed both in our computational results on $Sn_2P_2O_7$ and $Sn_3P_2O_8$ and in the experimental results for $Sn_3P_2O_8$ [175] and the glasses. The primary difference between the computations and the experiments is an evident systematic overestimation of both IS and QS, however, the compositional trend is reproduced accurately. The experimental results on $Sn_3P_2O_8$ closely bracket the results on the glasses. One would expect sites with more nearly equal bond lengths to have smaller quadrupole splittings, due to their more nearly tetrahedral or octahedral symmetry, and these sites are also the ones with the larger shifts. Similarly, the sites with small

shifts are those with three short bonds and a longer one, thus a greater deviation from symmetry and a larger quadrupole splitting.

Implicit in the above discussion is the assumption that the contacts at longer distances (Sn-O contacts of 2.85–3.25 Å) are truly bonds in the chemical sense. To test this assumption the AIM formalism was used to analyze the computed electron density distributions of $Sn_2P_2O_7$ and $Sn_3P_2O_8$. We found that most of the Sn-O contacts out to 3.25 Å do in fact show bond critical points, albeit with density about of about 10–20% that of the bond critical points of the three short bonds. These long contacts can thus indeed be counted as weak chemical Sn-O bonds.

Based on the above observations the Mössbauer spectra in the glasses are interpreted as indicative of an average tin site consisting of three short oxygen contacts and one longer, weak contact. At low SnO content, the short bond distances are very roughly 2.3 Å while the longer distances are about 2.85 Å, and as SnO is added, the short distances decrease to 2.1 Å and the longer distances increase to 3.25 Å. Note that by ^{119}Sn NMR, Holland *et al.* also concluded a tin coordination number of three [179], which would correspond to the three short bonds we posit. They also observed that the ^{119}Sn chemical shift skew increased with SnO content, which could arise from an increasingly asymmetric environment, as we see also (but more directly) from the tin quadrupole splitting. The more detailed interpretation we obtain arises mainly from the relative simplicity of interpreting and modeling Mössbauer spectra of ^{119}Sn as compared to ^{119}Sn NMR spectra.

The above structural model for the tin sites may be incorporated into the empirical model of the stress-optic response in several ways, as summarized in Table 6.4. The first, termed Model A, is the empirical model as originally proposed. Data for tin is incorporated through its crystal structure, for which the coordination number is 4 and the bond lengths are 2.22 Å. This model predicts zero-stress optic response at 69% SnO content, much higher than the 56% found experimentally [106]. In Model B, the longer Sn-O bonds of the glasses deduced from the Mössbauer spectra are ignored completely; in this case the contribution of SnO to the stress optic

response is substantially overestimated, leading to the prediction of zero-stress optic response at only 34%. If only the coordination number is allowed to increase from 3 to 4, Model C results, which is also in poor agreement with experiment. In Model D, the average bond length is increased as well, through a weighted average of short and long bonds. This model agrees very well with experiment. From the

Model	Bond length (Å)	N_c	Predicted Zero Stress Optic Composition
A	2.22	4	0.69
B	2.2	3	0.34
C	2.2	4	0.71
D	2.4	4	0.55

Table 6.4: Predicted compositions for zero-stress optic response, based on the empirical model and different treatments of the tin environment. Experimentally, tin phosphate glass shows zero-stress optic response at a composition of 0.56.

point of view of the empirical model, Models A and C overestimate the content of SnO needed to achieve zero-stress optic response because they both combine moderate bond lengths with larger coordination numbers. Thus the bonds are not very metallic, hence not polarizable, and the units are hard to deform anisotropically. Both conditions together are not very amenable to the necessary negative stress optic response needed to offset the positive stress optic response of the phosphate. In Model B, the coordination number is reduced but the bonds are unchanged, leading to a model of SnO that is exhibits significantly more negative stress response than is realistic and hence a gross underestimation of the amount of SnO needed of balance the phosphate response. In model D the metallicity of the long bonds are taken into account as well, again through their length, and the result is that when this level of structural detail is accounted for, the model is in good agreement the measured zero-stress optic composition.

6.1.5 Conclusion

In this section, we showed that the very simple empirical model for the composition dependence of the stress optic response in glass remains valid even when the modifying cation is in a complex environment consisting of variable contact lengths, provided that these structural features are incorporated into the model. Mössbauer spectra of tin were interpreted in detail through comparison with experimental data and first principles calculations on model systems to deduce that the tin sites are comprised of three short and one or two longer oxygen contacts; when incorporated into the empirical model, a prediction for the zero-stress optic composition in good agreement with experiment was obtained. It remains to investigate in more detail the physics of the stress optic response and why the simple empirical model works as well as it does.

6.2 Other binary tin-containing glass systems

6.2.1 Tin silicate $(SnO)_x$ - $(SiO_2)_{1-x}$

Among the tin-containing binary glasses, the tin silicate system has also been demonstrated to give a zero-stress optic composition for $x = 0.47$ [106]. The addition of tin oxide decreases the stress optic coefficient with the same "strength" as the lead oxide. In the lead silicate system, $C = 0$ occurs at $x_{PbO} = 0.45$ (see section 5.2.1). The tin oxide can be considered as the best potential substitute to PbO. In addition, tin(II) increases the refractive index of the glass and does not affect its transparency. The glass preparation has to be done under O_2-free atmosphere to avoid the oxidation of SnO to SnO_2 which brings a white color to the glass, and, according to the empirical model, contributes to a positive stress optic coefficient. From the prediction of the empirical model the zero-stress optic composition should be found at $x = 0.63$, which is a significant difference of about 34% with the experimental value.

In this glass the silicon atoms remain in a tetrahedral site surrounded by four oxygens no matter the amount of SnO. The $Si-O$ bond length does not suffer major variations, its value remains between 1.61 Å and 1.64 Å in the range of composition $0.20 \leq x \leq 0.80$ [180, 181]. ^{119}Sn Mössbauer spectroscopy shows a minor decrease in the isomer shift with the increase of tin oxide, which reveals the stability of the tin environment through the composition [182]. The quadrupole splitting decreases indicating that the tin atoms are getting into a site slightly more distorded when the amount of SnO increases. In spite of these variations, the local environment of the tin atoms also remains very stable through the range of compositions. The $Sn-O$ bond length was determined at 2.12 Å and does not vary [181]. The tin atoms are located on top of a triangle based pyramid. Therefore the coordination number of the tin atoms in the glass is 3, whereas it is 4 in the SnO crystal [183]. The tin remains with a low coordination number at low and high SnO content in the $(SnO)_x$-$(SiO_2)_{1-x}$ system. Tin is mainly covalent throughout the range of compositions, and no major structural modifications can be observed between the compositions with a positive stress optic coefficient and the ones with a negative stress optic coefficient. However it should be noted that a small amount of [SnO_4] square based pyramid units has been detected at high tin oxide content [180]. The existence of [SnO_3] pyramids in a network of [SiO_4] tetrahedra is possible only if some oxygens are shared between three cations (either Si_2OSn or $SiOSn_2$), which contravenes the second of Zachariasen's rules of glass formation [180, 181]. By using the coordination numbers and cation-oxygen bond lengths given previously for the tin and the silicon, the empirical model predicts a zero-stress optic composition at $x = 0.33$, which overestimate the contribution of the tin. The presence of tin four-fold coordinated should have an impact on the photoelastic response of the glass. Unfortunately no quantification of the two tin species was found in the literature. Furthermore, the empirical model takes into consideration the cations' coordination number but not the oxygen's coordination, which is assumed to be 2 in all oxide glasses. The presence of oxygen in coordination 3 might affect the quality of the theoretical results given by the model.

6.2.2 Tin borate $(SnO)_x$ - $(B_2O_3)_{1-x}$

No tin borate glass was prepared in the laboratory therefore no photoelastic data were acquired. No information about it could be found in the literature. However a few words could be said about its structure which remains partially unsolved. Tin borate glasses have been studied with various spectroscopic methods, such as ^{11}B NMR [184–186], ^{119}Sn NMR [185], ^{119}Sn Mössbauer [184, 187], Infrared [187] and neutron diffraction [186].

NMR and Mössbauer spectroscopy

The ^{11}B NMR results show similarities with the lead borate glass system. The introduction of SnO in the borate glass gives rise to the creation of $[BO_4]^-$ units at low content. The N_4 fraction increases to reach a maximum value at $x = 0.50$, and then decreases but the $[BO_4]^-$ units does not completely disappear [184,185]. The amount of tetrahedral boron is much less in the tin borate glass ($N_4(\text{max}) \approx 28\%$) than in the lead borate glass ($N_4(\text{max}) \approx 55\%$). It should be noted that the glasses synthesized by Holland *et al.* and by Hannon *et al.* were prepared in alumina crucibles, resulting in a small, but significant, amount of Al_2O_3 in the samples [186]. The presence of alumium oxide should affect the amount of $[BO_4]^-$ in the glass, these units being substituted by $[AlO_4]^-$ [188]. A comparison with the data obtained by Hayashi *et al.* [184], who prepared the samples in carbon crucibles, shows very good agreement and the small amount of Al_2O_3 seems to not affect the NMR results. For high tin compositions ($x > 0.5$) the N_4 fraction is decreasing. It could be expected that the $B - O$ bond length decreases with the boron's coordination number as observed in lead borate glass [148], but it remains almost constant in the range $0.40 \leq x \leq 0.70$. This unusual behavior does not fit the current model of glass structure and it remains unexplained [186]. Among the borate glasses, this phenomenon is observed only in the tin binary system, but it was also detected in germanate glasses such as caesium germanate [189, 190]. From ^{119}Sn Mössbauer spectroscopy [184, 187] and

^{119}Sn NMR, it seems clear that the tin atoms are acting mainly covalently. The static NMR spectra reveals an increasing Chemical Shift Anisotropy which tends to become identical to the CSA of the crystalline SnO [185]. The isomer shift and quadrupole splitting values also suggest a tin of coordination 3 in an asymmetric site [187]. The tin behavior is more ambiguous at low content. It seems to be a combination of asymmetric [SnO_3] units and highly symmetrical sites with high coordination [186]. In the whole range of compositions, $0.127 \leq x \leq 0.581$, the values of the quadrupole splitting are mostly greater than 1.7 mm.s^{-1} indicating a tin atom in an asymmetric environment. On the other hand, the ^{119}Sn static NMR spectra show a low CSA at low tin content typical of tin atoms in a symmetrical environment [185]. Tin and boron's coordinations and the cation-oxygen bond length were obtained from neutron diffraction and ^{11}B NMR [186].

Discussion

The use of these data in the empirical model reveals that all the glasses in the range of compositions $0.187 \leq x \leq 0.657$ should have a negative stress optic coefficient. By comparing the structure of the tin borate glasses with the structure of the lead borate glasses, it does not seem possible for low tin compositions to exhibit negative stress optic coefficients. It was shown in the previous sections that the empirical model gives accurate prediction of the photoelastic response of glass if detailed and precise data are provided. The $B-O$ bond length's unusual evolution and the ambiguous behavior of tin at low content remain to be solved. Nevertheless, it appears from all the studies previously mentioned that the tin has a coordination number of 3 and is acting covalently at high content. This is in good agreement with the implication of tin in the glass network, which is required to avoid the devitrification of the glass at high tin content. Also, by comparison with the lead borate glass, it can be predicted that high tin glasses should have an negative stress optic coefficient. Unfortunately the zero-stress optic composition cannot be predicted or estimated,

and only experiment data could provide an answer.

6.3 Tin borophosphate

$$(SnO)_x \text{ - } (B_2O_3)_y \text{ - } (P_2O_5)_{1-x-y}$$

In terms of the photoelastic response and optical properties, tin oxide appears to be the best candidate to substitute lead oxide in glass. Unfortunately its strong tendency to oxidize into SnO_2 makes its preparation more challenging than lead-containing glasses. The detailed study of the tin phosphate glasses presented in section 6.1 does not mentioned the chemical durability of these glasses. In fact no test of durability were performed on these samples, but it is well known that phosphate glasses are highly hygroscopic. These samples did not show any strong reactivity with atmospheric moisture and they were easily kept in a desiccator with no visible degradation of the material. Phosphate and borate glass systems are known to be hygroscopic, but the incorporation of a slight amount of B_2O_3 into a phosphate glass greatly improves the chemical durability [191–194]. Because of this interesting property, some tin borophosphate glasses were prepared and their structure and potoelastic response were investigated. One of the objectives of the work presented in this thesis was to find a glass that could compete with the Schott SF57 lead-containing glass in terms of the physico-chemical properties. Therefore the physical properties, or more precisely the optical properties, of the tin borophosphate samples were compared with the properties of the SF57 glass.

6.3.1 Experiment

Glass preparation

The glass samples were prepared from SnO (Sigma-Aldrich), $NH_4H_2PO_4$ (Sigma-Aldrich, 98+%, A.C.S. reagent) and B_2O_3 (Sigma-Aldrich, 99%). The samples were

prepared with specific $x_{B_2O_3}/x_{P_2O_5}$ ratios for different amounts of SnO. The reagents were weighted and mixed into an alumina crucible. The crucibles were then placed into the drybox's antechamber where the oxygen was removed by pumping out the air. The vacuum was made for one hour, then the antechamber was refilled with nitrogen and the vacuum was made again for another hour. This operation was repeated three times to be sure to remove all of the oxygen that could be trapped in the powders during the preparation. The drybox was not equipped with any oxygen detection device, only the pressure into the antechamber could be measured. Finally the crucibles were transferred into the drybox itself. All the glasses were prepared following the same general procedure: the crucible was placed into a box furnace preheated at 1050°C, then quenched at room temperature and immediately transferred onto a hot plate between 300°C and 350°C to prevent the glass from cracking. Glasses with molar fractions from 0.45 to 0.65 in SnO were prepared. Three series were successfully obtained for specific $x_{B_2O_3}/x_{P_2O_5}$ ratios of 0.2, 0.4 and 0.6. These compositions are reported on a ternary diagram (Figure 6.3). From here these series of samples are called 0.2, 0.4 and 0.6 series in reference to this ratio. The samples were annealed at a temperature between 300°C and 400°C, and then were cut and polished for stress optic measurements. Diamond pastes of different particle sizes from 15 μm down to 1 μm were used to polish the samples. The compositions of the glasses prepared by Lim *et al.* [195] are also reported on the ternary diagram of Figure 6.3. In their work, Lim *et al.* focused on the effect of the addition of B_2O_3 to the glass. They prepared two series of samples starting with a tin phosphate composition of 66.7 SnO - 33.3 P_2O_5 to which they added B_2O_3 according to the formulas:

- Series I: x B_2O_3 - (100-x)(66.7 SnO - 33.3 P_2O_5) $0 \leq x \leq 25$
- Series II: x B_2O_3 - 66.7 SnO - ((33.3-x) P_2O_5) $0 \leq x \leq 16$

In these two series, the addition of B_2O_3 reduces the aqueous corrosion rate by a factor of 10 [195]. These compositions are close to the samples prepared in this work,

therefore it is expected to obtain samples with good durability.

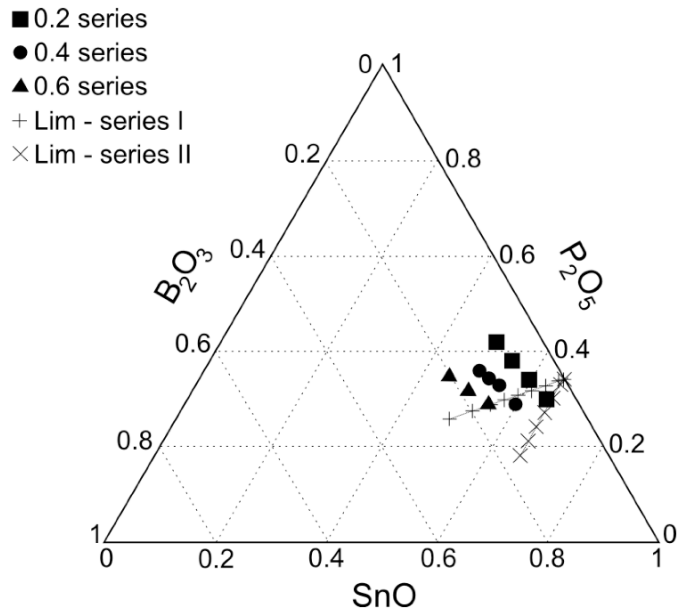

Figure 6.3: Ternary diagram of the glass compositions prepared for this work, and the compositions made by Lim *et al.*

Composition analysis

Attempts were made to analyze the exact composition of the glass samples by double-EDS analysis. Unfortunately, perturbation between the different elements, mainly due to the presence of boron atoms, resulted in poor signal quality and irrelevant quantitative results. All elements present in the glass were detected (B, O, P, Sn and Al from alumina crucible), but the proportion of each was not consistent from one measurement to the next leading to high uncertainties. As a consequence, the following discussion will be done only in a qualitative way, taking into account the nominal compositions.

Density measurements

All sample density measurements were performed using the Archimedes principle. The immersion liquid used was distilled water. Water was used instead of ethanol because of improved water corrosion resistance of the borophosphate glasses [195].

Absorption measurements

Absorption measurements were performed using the Varian Cary 5000 Spectrometer in the range of wavelength 300 nm (near UV) to 3300 nm (mid infrared). Only homogeneous samples with well polished faces were used for these measurements.

Refractive index

The refractive index was measured using an Atago Abbe refractometer. The typical refractive index was measured at wavelength 589 nm. The refractive indices at 486 nm and 656 nm were also recorded to calculate the dispersion and Abbe number of the glasses. The Abbe refractometer requires samples of specific size, therefore the refractive index was measured only for the biggest samples.

Stress optic measurements

The stress optic coefficient of each sample was determined by the Sénarmont method of compensation described in section 4.1.

^{119}Sn Mössbauer Spectroscopy

Room temperature ^{119}Sn Mössbauer effect spectra were obtained using a $Ca^{119m}SnO_3$ source and a Wissel System II Mössbauer spectrometer operating in constant acceleration mode. Center shifts were referenced to $CaSnO_3$ and the spectra were fitted

with the *Recoil* software package [159]. For the Mössbauer experiment, the glass samples were ground under O_2-free atmosphere in a mortar.

^{11}B Nuclear Magnetic Resonance Spectroscopy

All samples were crushed and packed in 2.5 mm rotors. The ^{11}B magic angle spinning (MAS) NMR was performed on a Bruker Avance NMR spectrometer with a 16.4 T magnet (700 MHz proton Larmor frequency, 224.68 MHz ^{11}B Larmor frequency). The samples were spun at 10 and 22 kHz to determine center bands and to identify spinning sidebands. The $NaBH_4$ resonance served as a secondary chemical shift standard at -42.1 ppm relative to $BF_3.Et_2O$ and was used to determine the pulse power. For the ^{11}B MAS NMR spectrum, 64 scans were accumulated using a pulse length of 0.4 μs at 78 kHz amplitude strength, chosen short for uniform excitation. Pulse repetition times between 1 and 5 s were determined to be sufficient for these samples. Because of the substantial boron background, mostly from the rotors, the spectrum of an empty rotor was subtracted.

^{31}P Nuclear Magnetic Resonance Spectroscopy

The ^{31}P NMR experiments were performed on a Bruker Avance NMR spectrometer with a 9.4 T magnet (162.02 MHz ^{31}P Larmor frequency) using a magic-angle spinning probe and 2.5 mm diameter sample rotors. The ^{31}P NMR chemical shift scale was referenced externally against $NH_4H_2PO_3$ at 0.81 ppm as a secondary reference. The 90 degree pulse time was also determined on this sample. The final 1-d magic-angle spinning spectra were acquired with a pulse of 0.75 μs (corresponding to a 20 degree flip angle) at 74 kHz rf field strength and 60 s recycle delay. Samples were spun at 25.0 kHz. Line shape simulations were performed using the program Dmfit [160] and XEDPLOT (Bruker software package).

6.3.2 Results

Density measurements

In all three series the density increases with the increase of SnO (Figure 6.4). No density data were found in the literature for this glass system, therefore no comparison is possible to obtain an estimate of the actual compositions. At similar tin content, the intermediate series 0.4 has the lowest density. For each sample the molar

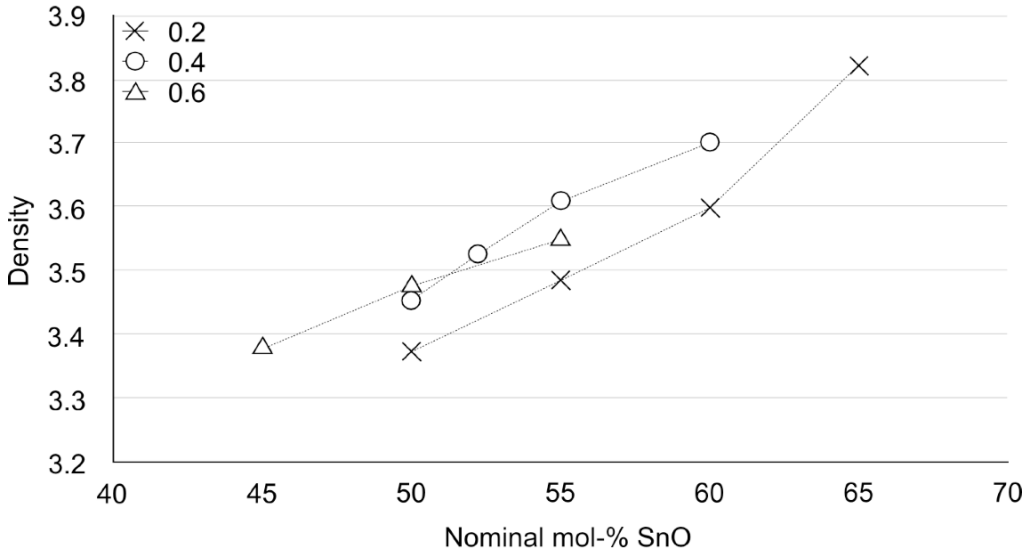

Figure 6.4: Density of the three series of tin borophosphate glasses. The results are presented here in function of the nominal composition of the samples. The uncertainty on the densities is ±0.001.

volume was calculated from the composition and density (Table 6.5), and its value decreases for all series of samples. These molar volumes were calculated from the nominal compositions, therefore no accurate interpretations and no final conclusions can be given based on these values. Nevertheless, it is interesting to note the sudden decrease of the molar volume in the 0.2 series from $x = 0.55$ to 0.60, whereas the values decreases continuously for the other two series.

Series	Nominal composition SnO	B_2O_3 (mol-%)	P_2O_5	Density ±0.001	Molar Volume ($cm^3.mol^{-1}$)
0.2	50.00	8.33	41.67	3.373	40.1883
	55.00	7.50	37.50	3.473	39.0287
	60.00	6.67	33.33	3.599	35.4399
	65.00	5.83	29.17	3.822	35.3063
0.4	50.00	14.29	35.71	3.454	37.8848
	52.50	13.57	33.93	3.525	37.1776
	55.00	12.86	32.14	3.609	36.3647
	60.00	11.43	28.57	3.701	35.5652
0.6	45.00	20.63	34.38	3.377	37.4705
	50.00	18.75	31.25	3.476	36.6141
	55.00	16.88	28.12	3.549	36.0695

Table 6.5: Density and molar volume for the three series of borophosphate glasses

Optical properties

The absorption spectra for the two series 0.2 and 0.4 are shown in Figure 6.5. The intensity of the signal is dependent of the quality of the glass. All glasses were not of similar homogeneity and the polishing may vary from sample to sample affecting the absorption and/or reflection of the glass. Therefore, the absorption coefficient are reported in arbitrary units, and the amplitudes of each signal cannot be compared. The absorption edge in the near-UV is observed at ∼320 nm. This edge is independent of the composition for the 0.4 series, whereas a slight shift from higher to lower energy with the increase of SnO is detected for the 0.2 series. All glasses show a peak of absorption in the mid-IR range (2750–2800 nm) which is shifted from lower to higher energy when the amount of SnO increases for both series. The amplitude of the IR shift is more significant than for the UV-edge. For the 0.2 and 0.4 series the shift of the absorption peak in the mid-IR is estimated at 10 nm/mol-% SnO and 17 nm/mol-% SnO respectively. In both series, two broad absorption bands centered at about 2250 nm and 2600 nm are present in the samples with the lowest

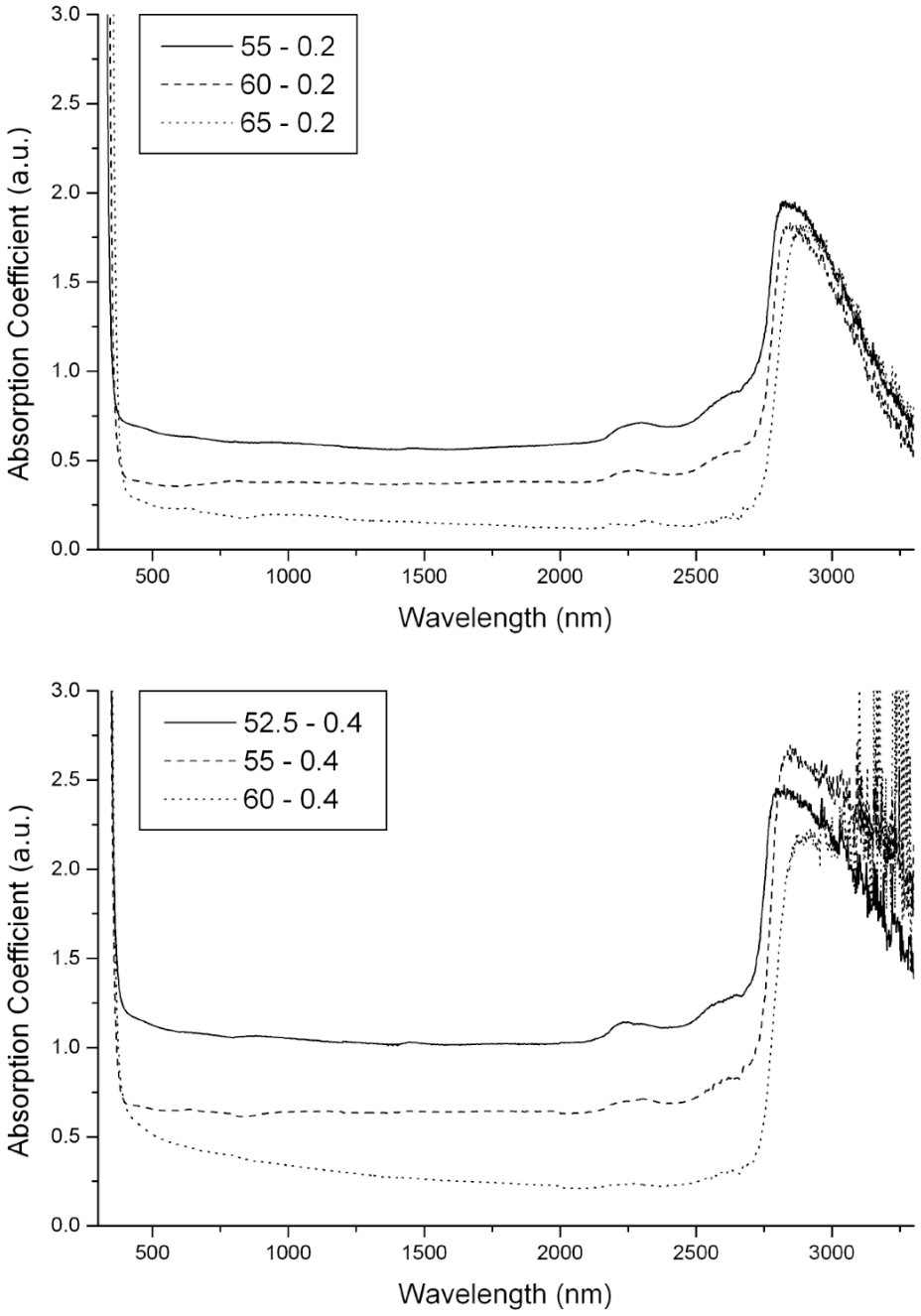

Figure 6.5: Absorption spectra of the tin borophosphate glasses with molar ratio $x_{B_2O_3}/x_{P_2O_5}$ equal to 0.2 and 0.4

amount of tin oxide. Their amplitude decreases with the addition of SnO, and they almost totally disappear for the high tin compositions. Contrary to the near-UV edge and the IR peak, these bands are not shifted with evolution of the composition. These spectra are in very good agreement with the transmission spectra from Lim *et al.* [195] .

The refractive index increases with the addition of SnO as expected. The addition of B_2O_3 also slightly rises its value. The refractive index at 589 nm, 486 nm and 656 nm are presented in Table 6.6. From these values the Abbe number V is calculated according to the formula:

$$V = \frac{n_{589} - 1}{n_{486} - n_{656}} \tag{6.1}$$

In this equation, $n_{486} - n_{656}$ represents the glass dispersion in the visible range. The Abbe number is used to plot the Abbe diagram which relates the refractive index to the Abbe number. This diagram gives a quick idea of the refractive and dispersive properties of a glass which can be classified in one of the 21 categories. The tin borophosphate samples belongs to the dense flint (SF) category corresponding to glasses with low Abbe number and high refractive index. Values for the Schott SF57 glass are also reported in Table 6.6 as a reference for comparison.

Stress optic coefficients

Negative stress optic compositions were achieved for the 0.2 and 0.4 series. In the 0.6 series, the stress optic coefficient is significantly reduced when SnO is added, and it can be expected that a glass with 60 mol-% SnO should be close to obtaining a zero-stress optic coefficient. A glass of such composition was achieved, but it was broken while cutting and polishing. The next attempts to prepare it resulted in milky white glasses. This color may come from the crystallization of the glass due to a low cooling rate (the inside of the drybox becoming quite warm during the melting process), or more probably from the oxidation of some Sn(II) into Sn(IV). Tin oxide

Series	Nominal composition SnO	B_2O_3 (mol-%)	P_2O_5	n_{589} ±0.0005	n_{486} ±0.0005	n_{656} ±0.0005	Abbe Number	Dispersion
0.2	50.00	8.33	41.67	1.6923	1.7087	1.6865	29.8405	0.0222
	60.00	6.67	33.33	1.7352				
	65.00	5.83	29.17	1.7848	1.8141	1.7745	19.8182	0.0396
0.4	50.00	14.29	35.71	1.7065	1.7234	1.6998	29.9364	0.0236
	55.00	12.86	32.14	1.7415	1.7613	1.7341	27.2610	0.0272
	60.00	11.43	28.57	1.7651	1.7869	1.7564	25.0852	0.0305
SF57 [196]	lead-containing glass			1.84666	1.87202	1.83650	23.8361	0.0355

Table 6.6: Refractive indices of some tin borophosphate glasses at 589 nm, 486 nm and 656 nm. From these values the Abbe number and the dispersion in visible are calculated. Data about the Schott SF57 are also provided for comparison.

participates to the glass network at high composition, but tin dioxide gives rise to a devitrification, and at low content it can also bring a white color to the glass. The stress optic coefficient are reported in Table 6.7. Figure 6.6 shows the relationship between the stress optic coefficient and the measured densities (from 6.3.2).

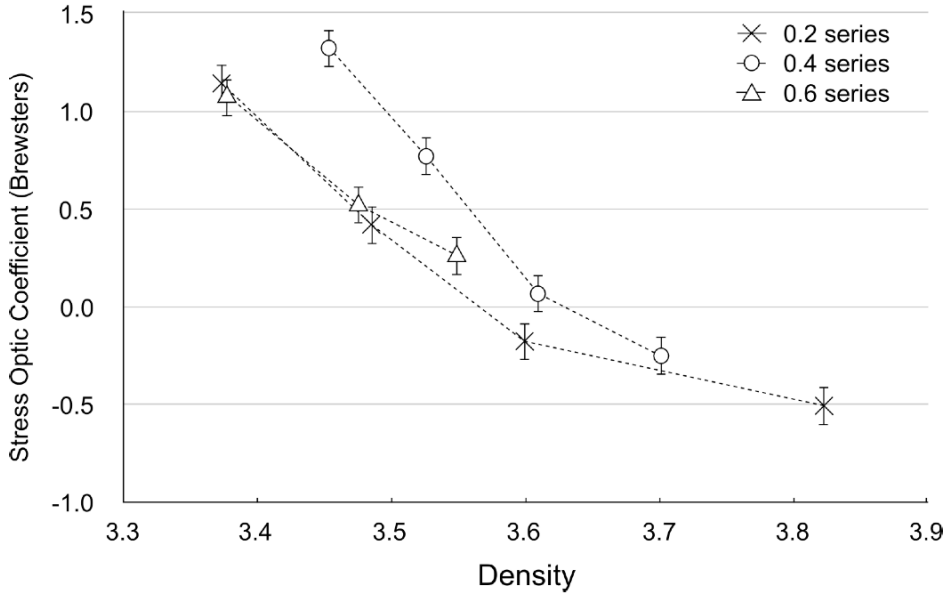

Figure 6.6: Stress optic coefficient vs. density.

Series	Nominal composition SnO	B_2O_3 (mol-%)	P_2O_5	Stress Optic Coefficient (Brewsters)
0.2	50.00	8.33	41.67	1.14
	55.00	7.50	37.50	0.42
	60.00	6.67	33.33	-0.18
	65.00	5.83	29.17	-0.51
0.4	50.00	14.29	35.71	1.32
	52.50	13.57	33.93	0.77
	55.00	12.86	32.14	0.07
	60.00	11.43	28.57	-0.25
0.6	45.00	20.63	34.38	2.35
	50.00	18.75	31.25	1.43
	55.00	16.88	28.12	0.54

Table 6.7: Stress optic coefficient of three series of the tin borophosphate glasses

Mössbauer spectroscopy

The values of the isomer shift IS, the quadrupole splitting QS, and the relative intensity are reported in Table 6.8. Some variations exist for the isomer shift and quadrupole splitting of the singlet and doublet. The isomer shift for the singlet is always in the range -0.30 to -0.40 $mm.s^{-1}$ but only the values for the 0.4 series seems to follow a continuous variation (increase) with the composition. The isomer shift of the doublet evolve more randomly and do not reveal any trend. On the other hand, the quadrupole splitting always increases with the addition of SnO for the three series of glass. The Mössbauer spectra reveals the existence of a doublet centered around 2.3 $mm.s^{-1}$ and a singlet around -0.4 $mm.s^{-1}$ for all samples. The doublet represents the majority of the signal with an intensity of about at least 90%. The relative intensities evolve quite randomly with the compositions.

Series	SnO (mol-%)	Singlet		Doublet		
		IS ($mm.s^{-1}$)	Relative Intensity (%)	IS ($mm.s^{-1}$)	QS ($mm.s^{-1}$)	Relative Intensity (%)
0.2	50	-0.41(6)	4.8(8)	+3.25(7)	1.54(5)	95.2(9)
	55	-0.39(5)	5.3(5)	+3.19(5)	1.57(7)	94.7(7)
	60	-0.38(5)	9.2(7)	+3.23(5)	1.62(5)	91.0(9)
	65	-0.35(5)	10.3(4)	+3.21(5)	1.65(6)	89.8(5)
0.4	50	-0.40(5)	9.2(3)	+3.25(5)	1.61(5)	90.8(4)
	55	-0.37(5)	6.8(8)	+3.25(5)	1.61(5)	93.0(9)
	60	-0.34(5)	10.2(5)	+3.22(5)	1.63(6)	89.7(5)
0.6	45	-0.41(5)	5.7(5)	+3.25(5)	1.62(7)	94.2(6)
	50	-0.24(5)	12.7(7)	+3.23(7)	1.61(5)	87.3(8)
	55	-0.37(5)	10.1(5)	+3.26(5)	1.62(7)	89.9(6)

Table 6.8: Isomer shift, quadrupole splitting and relative intensity obtained for the tin borophosphate. The uncertainty on the last digit is given in the brackets.

^{11}B Nuclear Magnetic Resonance Spectroscopy

The ^{11}B Nuclear Magnetic Resonance Spectroscopy revealed the presence of $[BO_3]$ and $[BO_4]^-$ units in the samples (see Table 6.9). At low B_2O_3 content, only the boron 4-fold coordinated is present, but the fraction of $[BO_3]$ increases with the addition of boron oxide, in good agreement with the general behavior of borophosphate glasses [191–193,197,198]. For each sample, only one peak is present in the range 10-13 ppm corresponding to the $[BO_3]$ species, whereas two to three peaks can be observed in the range 0 to -3.90 ppm associated with the $[BO_4]^-$ species. The overall number of peaks ($[BO_3]$ + $[BO_4]^-$) and their respective chemical shifts increases with the addition of tin oxide.

^{31}P Nuclear Magnetic Resonance Spectroscopy

All spectra obtained for the ^{31}P Nuclear Magnetic Resonance Spectroscopy gave one peak that could be decomposed in two gaussians. The results of the deconvolution

Series	SnO	B3		B4					
		δ	Fraction	Peak 1		Peak 2		Peak 3	
	(mol-%)	(ppm)	(%)	δ (ppm)	Frac. (%)	δ (ppm)	Frac. (%)	δ (ppm)	Frac. (%)
0.2	50	-	0	-3.70	99.03	-1.03	0.97	-	0
	55	-	0	-3.63	93.94	-1.37	6.06	-	0
	60	-	0	-3.66	92.76	-1.09	7.24	-	0
	65	-	0	-3.43	60.08	-1.24	25.86	-0.22	14.06
0.4	50	10.41	3.06	-3.79	80.63	-1.46	12.68	-0.05	3.63
	55	11.59	5.82	-3.62	65.71	-1.35	20.33	0.05	8.14
	60	12.60	14.37	-3.55	44.09	-1.38	20.32	-0.35	21.22
0.6	45	11.03	8.27	-3.85	65.11	-1.74	14.92	-0.65	11.70
	50	12.66	14.80	-3.69	46.25	-1.57	20.89	-0.43	18.06
	55	12.56	23.28	-3.54	29.41	-1.54	18.89	-0.38	28.42

Table 6.9: ^{11}B NMR results of the three series of tin borophosphate glasses

is presented in Table 6.10. In the binary tin phosphate glass, the Q^n species can be assigned to specific ranges of the chemical shifts and a gap exits between each range [179]. In the tin borophosphate, no clear gap can be observed, no clear limit can be defined, therefore the choice has been made to not assign the Q^n species to specific chemical shift. As a general rule, the chemical shift decreases with the increasing number of bridging-oxygens n [199–202]. In the zinc borophosphate and lead borophosphate glasses, the Q^2 species were associated to a downfield shift from a chemical shift of -30 ppm and -25 ppm respectively [203]. From this statement, it can be considered that only Q^2 and Q^1 species are present in the samples, except for the glass with $x = 0.50$ of series 0.2 which might contain some Q^3 ($\delta = -34.95$ ppm). No clear distinctions can be made to know what is the limit between the range of chemical shifts corresponding to Q^2 and the range corresponding to Q^1. In a general trend, the addition of SnO increases the chemical shift which can be interpreted as an increases of non-bridging oxygens. At low tin content, the addition of B_2O_3 also increases the chemical shift, but this effect is weakened at high tin content.

Series	SnO (mol-%)	δ (ppm)	Relative Intensity (%)	Width (ppm)	δ (ppm)	Relative Intensity (%)	Width (ppm)
0.2	50	-34.95	13.6	15.08	-25.85	86.4	15.46
	55	-25.9	57.4	17.67	-22.79	42.6	13.75
	60	-21.31	100	16.79	-	-	-
	65	-17.11	72.3	15.46	-13.05	27.7	11.51
0.4	50	-28.79	26.2	16.09	-21.71	73.8	15.69
	55	-24.08	39.8	15.38	-17.8	60.2	14.19
	60	-22.93	31.2	14.61	-15.66	68.8	13.38
0.6	45	-25.83	68.9	17.08	-20.84	31.1	14.90
	50	-23.28	70.8	16.6	-18.29	29.2	12.5
	55	-22.87	48.8	15.17	-16.94	51.2	12.82

Table 6.10: ^{31}P NMR results of the three series of tin borophosphate glasses

6.3.3 Discussion

On the absorption spectra, the near-UV edge remains unchanged for all samples. Only the peak of absorption at about 2850 nm is slightly shifted to lower energies with the increase of tin oxide in the glass. The absorption spectra are in good agreement with the transmission spectra obtained by Lim *et al.* which also show the two bands at 2250 nm and 2600 nm [195]. These bands are present for their two series of samples containing 10 mol-% B_2O_3 with the same intensity; however they do not exist for the tin phosphate glass 66.7 SnO - 33.3 P_2O_5. Therefore, these two absorptions can be associated with the presence of boron in the glass. It should be noted that for the 0.2 series, no significant changes are observed in the visible range. For the 0.4 series, the sample at $x = 0.60$ shows a constant increase of absorption at short wavelengths starting from 1500 nm. Such a variation would probably give rise to a coloration of the glass because of the difference of absorption at 700 nm and 400 nm, but the glass was colorless. The poor homogeneity of the glass might affect the measurement of the absorption. In terms of refractive properties, the tin-containing glasses prepared here have a lower refractive index than the

Schott glass, but they also have a lower dispersion in the visible range, especially when the amount of B_2O_3 increases. From the stress optic measurements it can be estimated that the zero-stress optic glass for the 0.4 series should have a refractive index near 1.75 which is lower than the Schott SF57. Lim *et al.* achieved a tin borophosphate glass with a refractive index slightly higher than 1.84 of composition 66.7 SnO - 13 B_2O_3 - 20.3 P_2O_5 [195]. This composition has a high amount of SnO and a $x_{B_2O_3}/x_{P_2O_5}$ ratio of 0.64. The tin oxide brings the high refractive properties, but such a high amount would result in a negative stress optic glass. To obtain a zero-stress optic glass with a refractive index close to 1.84, the $x_{B_2O_3}/x_{P_2O_5}$ ratio should also be increased.

No accurate composition analysis were obtained for these series of samples, however density measurements were performed. As expected the addition of tin in the glass increases the density. The 0.4 series shows higher density than the 0.2 series, but the 0.6 series shows more or less the same densities as the 0.2 series. It is easy to interpret the density in terms of composition in a binary system, it is more ambiguous in a ternary system. The calculation of the molar mass would suggest that glasses from series 0.2 and 0.6 are different, but these values were calculated from the nominal compositions. Without an accurate determination of the composition, no final conclusion can be made. The plot of the stress optic coefficient in function of the densities (Figure 6.6) highlight even more the similarities between the 0.2 and 0.6 series. Only the last glass of the 0.6 series ($x = 0.55$) shows different properties than the samples of the 0.2 series. One possibility to explain such similarities is the loss of P_2O_5 by volatilization while preparing the samples of the 0.2 series, which would increase the $x_{B_2O_3}/x_{P_2O_5}$ ratio.

Typically the isomer shift for Sn(II) ranges from +2.30 mm.s^{-1} and +4.44 mm.s^{-1}and the isomer shift for Sn(IV) ranges from -0.4 mm.s^{-1} and +1.9 mm.s^{-1} [204]. Therefore the doublet can easily be attributed to SnO. The isomer shift and quadrupole splitting remains quite constant for all compositions with values of 3.2 mm.s^{-1}and 1.6 mm.s^{-1}respectively. These values are quite similar to the isomer shift and

quadrupole splitting of the tin phosphate glass 66 SnO - 33 P_2O_5 (see section 6.1.3 Table 6.1). From these previous results, it can be determined that the Sn(II) forms short bonds with three oxygens and one additional longer bond with a fourth oxygen. The association of an isomer shift of about 3.25 mm.s^{-1} with a quadrupole splitting of 1.6 mm.s^{-1} is also characteristic of a tin(II) acting mainly covalently [204]. The small variations of the Mössbauer parameters reveals a tin environment that remains constant for the different compositions.

The case of the singlet is more surprising. This doublet could be attributed to the presence of tin dioxide in the glass, but the isomer shift of SnO_2 should be located at 0.0±0.1 mm.s^{-1}. Here the isomer shift is clearly lower, at the lowest possible value for Sn(IV), revealing a strong ionic character [204]. The Sn(IV) isomer shift can be predicted with the following equation:

$$\delta = 1.92 - 0.795\Delta\chi_p - 0.1775(\Delta\chi_p)^2 \tag{6.2}$$

with $\Delta\chi_p$ the difference of Pauling electronegativity between the tin and the bonded atom [204]. According to this equation and taking an electronegativity of 1.9 for the tin atom, the atom bonded to Sn(IV) should have an electronegativity of 3.91 to give an isomer shift of -0.4 mm.s^{-1}. The electronegativity of fluorine is exactly 3.90 [205], and such a low isomer shift was only observed in tin fluoride compounds such as SnF_4, Sn_3F_8, and Sn_2F_6 [206]. The glasses were prepared from B_2O_3, $NH_4H_2PO_4$, and SnO, while traces of Al_2O_3 might also be present due to the preparation in alumina crucibles, but the starting reagents and final glasses were never in contact with fluorine-containing compounds. This low isomer shift also reveals a strong ionic behavior of the Sn(IV). The glass at $x = 0.50$ for the 0.6 series has the highest relative intensity for the singlet. Assuming this peak comes from the presence of SnF_4 in the glass, the molar fraction of tin fluoride would be about 6.35 mol-%. This sample was analyzed by Energy Dispersive X-Ray spectroscopy and ^{19}F NMR spectroscopy to detect the fluorine, but no signal was recorded from both techniques. No more analysis were performed to understand the origin of this low isomer shift.

The NMR parameters reported in Table 6.9 and Table 6.10 clearly show the structural differences between the 0.2 and 0.6 series. Therefore, in spite of a similar densities and stress optic coefficients, the glasses of the two series actually seem to be different. Without any accurate composition analysis, no final statement can be made. The easiest way to correlate the ^{11}B and ^{31}P NMR chemical shift would be to compare the values with data obtained from a crystalline tin borophosphate of known structure. Unfortunately such crystal does not exist. However, data about the crystalline BPO_4 are available in the literature, and the tin borophosphate glasses show similarities with the sodium borophosphate glasses [207]. The BPO_4 crystal structure is made of a three dimensional network of vertex-sharing $[BO_4]^-$ and $[PO_4]^+$ tetrahedra [208]. The ^{11}B MAS NMR spectrum of BPO_4 gives a single peak at -4 ppm corresponding to the $B(OP)_4$ units (tetrahedral boron which shares oxygens with four phosphorus atoms); and ^{31}P MAS NMR spectrum reveals a single peak at -29.8 ppm from the $P(OB)_4$ (tetrahedral phosphorus which shares its oxygens with four boron atoms) [209]. The structure of sodium borophosphate glasses was determined by comparing the NMR data from the glass with data from the crystal of known structure $Na_5B_2P_3O_{13}$ [207]. The complete resolution of borophosphate glasses is quite challenging and requires 2D NMR experiments in addition of MAS experiment to properly assign the signals to the correct P and B species [207, 210]. At low boron content, only $[BO_4]^-$ units are present in the glass. They share their oxygens only with phosphorus atoms to connect the $P-O-P$ chains with each other [191–193, 197, 198, 211]. By comparison with the BPO_4 crystal and sodium borophosphate glass, the ^{11}B chemical shift in the range [-3.70 to -3.43 ppm] can be attributed to $[B(OP)_4]$ units, and the chemical shifts at [-1.74 to -1.03 ppm] and [-0.65 to -0.05 ppm] correspond to $B(OP)_3(OB)$. In this last structural unit the boron in the second sphere of coordination can be in two slightly different geometries giving rise to two different chemical shifts. The uncertainty about the the exact composition of the samples limits the interpretation of the glass structure. For this reason, no new estimation of the zero-stress optic composition will be calculated from the empirical

model taking into account the amount of SnO_2 (or SnF_4) and $[BO_4]^-$.

6.3.4 Conclusion

The synthesis of the tin borophosphate glasses was initiated to find a new family of zero-stress optic glass which was successfully achieved. A binary glass system offers only one zero-stress optic composition, but a ternary system extends the possibility to a range a compositions. The glasses were transparent and colorless with a high refractive index. No test of durability was performed but the borophosphate glasses are known for their good chemical resistance [195]. These glasses make potential candidates to substitute lead-containing glasses. The main disadvantage of these tin-containing glasses is their preparation under O_2-free atmosphere to avoid the oxidation of SnO into SnO_2. The glasses where prepared in the small range $0.45 \leq x \leq 0.65$ with three different $x_{B_2O_3}/x_{P_2O_5}$ ratios (0.2, 0.4, and 0.6). For all the samples, the Sn(II) remains in a constant environment with a covalent behavior similar to the tin in 67 SnO - 33 P_2O_5. It is bonded to four oxygens with three short bonds and one longer bond. The ^{11}B MAS NMR revealed the presence of $[BO_4]^-$ units only at low boron content and the appearance of $[BO_3]$ units as the amount of B_2O_3 increase. This is in good agreement with the behavior of borophosphate glasses. In the same way, the evolution of the phosphorus chemical shift follow a classical trend from high field to low field (increase of the number of non-bridging oxygens) as the amount of SnO increases. Unfortunately no composition analysis was obtained, limiting the interpretation from the spectroscopic experiments. Also, the Mössbauer spectroscopy revealed the presence of ionic Sn(IV) in the glass. Its isomer shift corresponds to a tin(IV) bonded to fluorine, but Energy Dispersive X-Ray spectroscopy and ^{19}F NMR spectroscopy did not detect the presence of fluorine in the glass. The structure of borophosphate glass is known to be very complicated to solve [207], and the tin borophosphate glasses are no exception. More experiments, such as two-dimensional NMR and a complete and accurate composition analysis, should

be performed to obtain more details about the structure of these glasses. Similarly to the tin binary glasses, the environment of the tin atoms remains quite stable, the tin remaining mainly covalent for positive and negative stress optic coefficients.

6.4 Summary

The study of the tin binary glasses revealed the dominant covalent nature of the tin at low and high content. Similarly to the lead-containg glasses, a negative stress optic coefficient occurs when the additive acts mainly covalently. Therefore Mueller's theory cannot explain the structural origin of the photoelastic response of the tin-containing glasses. The structural study of the tin phosphate glasses revealed the constant coordination of the tin and the variation of the $Sn-O$ bond length. By taking into account these variations the error of the prediction calculated with the Zwanziger's empirical model is reduced from 25% to 2%. The accuracy of the model is also increased in the case of the tin silicate glass.

New zero-stress optic glass properties were discovered in tin borophosphate glasses. The glasses combined some interesting properties such as transparency and no coloration, high refractive index, low dispersion in the visible range, and a probable good chemical durability according to the literature. The structural analysis revealed the presence of ionic Sn(IV) probably bonded to fluorine, but EDS analysis and ^{19}F NMR spectroscopy did not detect any fluorine in the sample. The environment of this Sn(IV) and the detailed structure of the glass remains partially unsolved.

Chapter 7

Antimony-containing glasses

Antimony can assume two different oxidation states, Sb(III) and Sb(V), leading to the existence of two different antimony oxides: Sb_2O_3 and Sb_2O_5. Antimony(V) oxide Sb_2O_5 is generally considered a glass network former because of its high field strength (1.76) [30]. Antimony(III) oxide Sb_2O_3 has a much lower field strength (0.73) [30,212], and should be considered as an intermediate oxide. Nevertheless, pure Sb_2O_3 glass has been successfully prepared [108], but its synthesis remains extremely challenging and requires conditions combining both fast remelting and cooling down conditions [108, 212]. By definition, an oxide that is able to produce a glass on its own is a glass former, therefore Sb_2O_3 can as well be considered as a glass network former. Similar to tin oxide, antimony(III) oxide has a d/N_c ratio greater than 0.5 Å, therefore it can be considered as a potential candidate to enter in the composition of new zero-stress optic glass. In this chapter the cases of antimony phosphate, antimony borate, and antimony borophosphate glass systems are presented.

7.1 Antimony phosphate system $(Sb_2O_3)_x$-$(P_2O_5)_{1-x}$

7.1.1 Experiment

Glass preparation

The antimony phosphate glasses were one of the very first glasses prepared for this thesis. This project was initiated with the objective to extend a previous study of the photoelastic response in lead-free binary glass systems [106]. The glass samples were prepared following a procedure derived from De Vicente *et al.* [213]. The starting reagents Sb_2O_3 (Sigma-Aldrich, 99%) and $NH_4H_2PO_4$ (Sigma-Aldrich, 98+%, A.C.S. reagent) were mixed in an alumina crucible and placed in a box furnace preheated at 200°C. The temperature was increased by 100°C every 30 minutes until 700°C. If the crucible was placed directly at high temperature, the loss of ammonia and water from the ammonium dihydrogen phosphate would create a foam causing the mixture to overflow out of the crucible. This loss of water and ammonia was also observed in the preparation of the tin phosphate and tin borophosphate glasses. The presence of antimony with the ammonium dihydrogen phosphate seems to amplify the phenomenon. Melnikov *et al.* performed a thermal analysis (Differential Thermal Analysis and Thermogravimetry) of the reaction between Sb_2O_3 and $NH_4H_2PO_4$ and suggested the following mechanisms [214]:

at 200°C: $$n\mathrm{NH_4H_2PO_4} \longrightarrow (\mathrm{NH_4PO_3})_n + n\mathrm{H_2O}$$

at 488°C: $$6(\mathrm{NH_4PO_3})_n + \mathrm{Sb_2O_3} \longrightarrow 2n\mathrm{Sb(PO_3)_3} + 3n\mathrm{H_2O} + 6n\mathrm{NH_3}$$

Therefore, a slow increase of temperature is required to avoid a loss of reagent. The mixture was liquid at 700°C but too viscous to be poured out of the crucible and to give an homogeneous glass. To decrease the viscosity, the temperature was

increased up to 1000°C for the samples at $x \geq 0.40$. Five compositions were attempted with $x = 0.25, 0.30, 0.35, 0.40, 0.45$, and 0.55. For $x \leq 0.30$, the glasses had to be quenched onto a hot plate at 100°C in order to decrease the cooling rate and to avoid the glass breaking; for $x = 0.35$, the glass was easily quenched at room temperature, and for $x \geq 0.40$ the glasses were quenched onto brass plates cooled in liquid nitrogen. Even in these conditions, it remained difficult to obtain a glass with no partial crystallization on the edges of the samples. A bulk glass thick enough for stress optic measurements was obtained for most of the compositions except for the samples with the highest content in Sb_2O_3, $x = 0.45$ and $x = 0.55$. In these two cases the glasses were obtained by pressing the molten glass between two brass plates cooled in liquid nitrogen. These two samples were too thin for a stress optic measurement. All the compositions gave transparent glasses with an increasing yellow color as the amount of antimony oxide increased. All the samples also contained bubbles. It should be mentioned that the sample at $x = 0.45$ also contained tiny white crystals. Glasses with compositions $x \leq 0.35$ are easy to prepare but much harder to store for long term analysis, whereas the compositions at $x \geq 0.40$ are much harder to obtain but easier to preserve in a desiccator. Only one sample for each composition at $x = 0.40, 0.45$, and 0.55 was prepared, but two to three samples had to be prepared for the compositions with low antimony content, some glasses having been lost while stored or coated for composition analysis. The samples were cut and polished using ethanol as a lubricant instead of water.

Composition analysis

No composition analysis was successfully performed on these samples. Four attempts were made to analyze the samples by Energy-Dispersive X-ray Spectroscopy (EDS) coupled with Scanning Electron Microscopy (SEM) at the SEM-FIB laboratory in the Dalhousie Engineering School and at the Microprobe laboratory in the Earth Science department (Dalhousie University). For every attempt, schedule or technical

problems occurred. The samples had to be stored longer than expected and ended up absorbing moisture and being too degraded for any measurement.

Refractive index

The refractive index was measured using an Atago Abbe refractometer. The typical refractive index was measured at wavelength 589 nm.

Stress optic measurements

The stress optic coefficient was measured for only three samples ($x = 0.30, 0.35,$ and 0.40) using the Varian spectrometer. The glass with 25 mol-% Sb_2O_3 was too hygroscopic and absorbed water by the time it was cut and polished and the samples with 45 and 55 mol-% Sb_2O_3 were not thick enough for the measurement. The phase difference induced by the stress was measured using the Sénarmont method of compensation described in section 4.1.

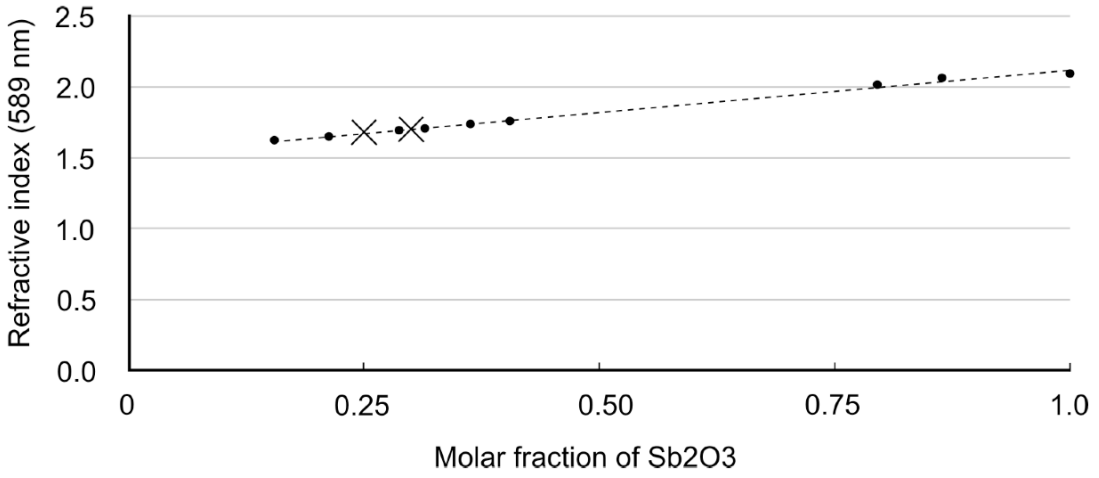

Figure 7.1: Refractive index at 589 nm of the antimony phosphate glass. Data obtain for the glasses at 25 and 30 mol-% (×) are compared with data from the literature (• and dashed line) [108, 215]. The uncertainty on the refractive index measurement is ± 0.001.

7.1.2 Results

Refractive indices

The refractive index at 589 nm and 20°C was measured for two compositions, $(Sb_2O_3)_{0.25}$ - $(P_2O_5)_{0.75}$ and $(Sb_2O_3)_{0.30}$ - $(P_2O_5)_{0.70}$, with an Abbe refractometer. The results are compared with values from the literature [108, 215] in Figure 7.1.

Stress optic measurements

The results are given in Table 7.1 and Figure 7.2. The compositions given are the nominal compositions. The addition of Sb_2O_3 decreases the stress optic coefficient, and the sample for $x = 0.40$ shows a negative value.

$\mathbf{x}_{Sb_2O_3}$ **mol-%**	**C (Brewsters)**
0.30	2.46(3)
0.35	2.00(3)
0.40	-0.66(3)

Table 7.1: Stress optic coefficient of the antimony phosphate glasses. The uncertainty on the last digit is given in brackets.

7.1.3 Discussion

The preparation of this binary glass system from antimony oxide and ammonium dihydrogen phosphate by the classic melting/quenching technique did not give the expected results. On one hand the glasses with a low content of antimony (high content of phosphorus) are very hygroscopic, and on the other hand the compositions with a high content of antimony were extremely difficult to prepare. According to the empirical model, a glass containing only Sb_2O_3 and P_2O_5 should have zero-stress optic properties at about $x = 0.41$ which corresponds to the glass composition that requires extremely fast quenching. A glass with a negative stress optic coefficient was

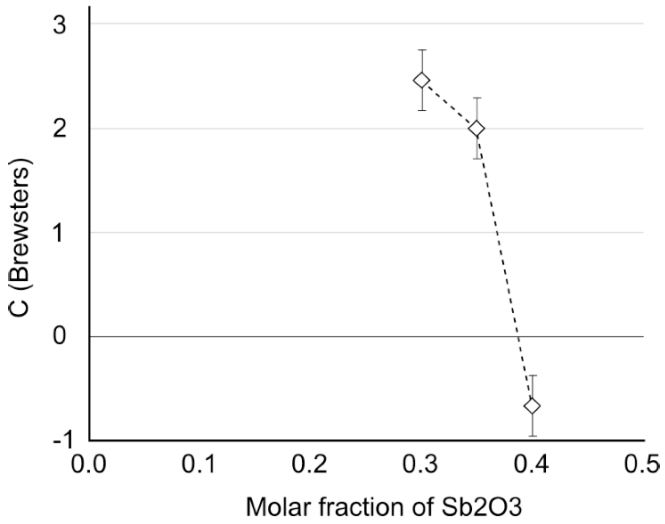

Figure 7.2: Stress optic coefficient of the antimony phosphate glasses

successfully obtained with nominal composition $x = 0.40$. Unfortunately, composition analysis could not be performed on these glasses due to their high hygroscopic nature. Some phosphorus pentoxide can be lost by volatilization during the melting process, therefore it can be expected that the glasses contain less P_2O_5 than the nominal composition. A comparison of the refractive indices with the literature suggests that at low Sb_2O_3 content, the samples are very close to the nominal compositions. Antimony phosphate glasses with a high content of antimony were already prepared in the binary system $(Sb_2O_3)_x$-$(SbPO_4)_{1-x}$ [216] which can also be formulated $(Sb_2O_3)_{1+x}$-$(P_2O_5)_{1-x}$. For this system, the glass samples are also prepared by the melting/quenching technique: Sb_2O_3 and $SbPO_4$ are melted between 700°C and 900°C for 10 minutes in air and quenched at room temperature. The starting antimony oxide can be bought from Sigma-Aldrich, but the antimony orthophosphate $SbPO_4$ has to be prepared in the laboratory from $SbCl_3$ and H_3PO_4 in a three day long procedure [217]. The glass compositions prepared by Nalin *et al.* are listed in Table 7.2. No attempt was made to prepare the antimony phosphate glass according to this long and complicated procedure.

Sb_2O_3	$SbPO_4$	Sb_2O_3	P_2O_5
0.90	0.10	0.95	0.05
0.80	0.20	0.90	0.10
0.70	0.30	0.85	0.15
0.60	0.40	0.80	0.20
0.50	0.50	0.75	0.25
0.40	0.60	0.70	0.30
0.30	0.70	0.65	0.35

Table 7.2: List of the $(Sb_2O_3)_x$-$(SbPO_4)_{1-x}$ samples prepared by Nalin *et al.* and their equivalent in the $(Sb_2O_3)_{1+x}$-$(P_2O_5)_{1-x}$ system.

7.1.4 Conclusion

This antimony phosphate system is one among other antimony glasses that can be prepared. In spite of the strong hygroscopic nature of the samples, some physical properties were measured. The main problem encountered was the storage of the samples and their handling in air. The first series of samples prepared were stored in a desiccator but they absorbed moisture from the silica gel desiccant. The glasses with the highest content in P_2O_5 turned white overnight. The successful synthesis of a Sb-containing glass with a negative stress optic coefficient is encouraging and proved that zero-stress optic coefficient glass can be obtained from Sb_2O_3 without preparation under O_2-free atmosphere.

7.2 Antimony borate system $(Sb_2O_3)_x$-$(B_2O_3)_{1-x}$

The antimony borate system gives a zero-stress optic coefficient for $x = 0.43$ [106]. But this experimental value was obtained from two samples prepared in air. At high temperature Sb(III) can be partially oxidized into Sb(V) [218] and according to the empirical model Sb_2O_5 contributes to a positive stress optic coefficient whereas

Sb_2O_3 contributes to a negative stress optic coefficient. The presence of Sb(V) in the glass should affect the photoelastic response of the glass and might be one of the explanation for the large difference between the empirical results ($x = 0.20$ for $C = 0$ Brewsters) and the experimental value. In this section, an attempt was made to prepare antimony glass samples under O_2-free atmosphere with the aim of testing the empirical model and to understand the origin of the difference between the empirical and experimental results.

7.2.1 Experiment

Glass preparation

To avoid the partial oxidation of Sb(III) in Sb(V) at high temperature, the glasses were prepared into a drybox under O_2-free atmosphere.

The starting reagents Sb_2O_3 (Sigma-Aldrich, 99%) and B_2O_3 (Sigma-Aldrich, 99%) were weighted and mixed in platinum crucibles. The crucibles were transferred into a drybox filled with nitrogen following the same procedure described in section 6.3.1. The crucibles were placed for an hour in a furnace preheated at 500°C then the temperature was increased at 1050°C. After 15 minutes, the glasses were quenched into a brass mold at 500°C to avoid a fast cooling that would give rise to a phase separation in the glass. The glass is left in the mold until it cooled down to room temperature. The samples obtained were yellow and transparent with no visible phase separation but with some inhomogeneities. Three samples were successfully obtained with nominal compositions $x = 0.35, 0.50$, and 0.65. From these three samples, it is expected to have one positive stress optic coefficient, one close to zero (positive or negative) and one negative coefficient as the amount of Sb_2O_3 increases.

Stress optic measurements

The stress optic coefficient was measured for the three samples ($x = 0.30, 0.35$, and 0.40) using the light table. The phase difference induced by the stress was measured according to the Sénarmont method of compensation described in section 4.1.

Density measurements

All density measurements were performed using the Archimedes principle. The immersion liquid used was 99+mol% ethanol. Water was not used because of the hygroscopic character of the glasses, particular those with low antimony content. Due to the slight variation of the density of ethanol depending on temperature, a series of values for the density of ethanol were taken from the literature [128].

^{11}B Nuclear Magnetic Resonance Spectroscopy

All samples were crushed and packed in 2.5 mm rotors. The ^{11}B magic angle spinning (MAS) NMR was performed on a Bruker Avance NMR spectrometer with a 16.4 T magnet (700 MHz proton Larmor frequency, 224.68 MHz ^{11}B Larmor frequency). The samples were spun at 10 and 22 kHz to determine center bands and to identify spinning sidebands. The $NaBH_4$ resonance served as a secondary chemical shift standard at -42.1 ppm relative to $BF_3.Et_2O$ and was used to determine the pulse power. For the ^{11}B MAS NMR spectrum 64 scans were accumulated using a pulse length of 0.4 μs at 78 kHz amplitude strength, chosen short for uniform excitation. Pulse repetition times between 1 and 5 s were determined to be sufficient for these samples. Because of the substantial boron background, mostly from the rotors, the spectrum of an empty rotor was subtracted.

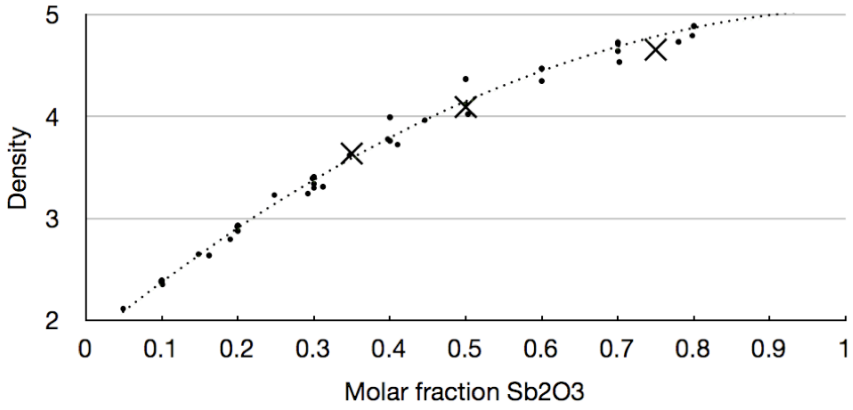

Figure 7.3: Density of the antimony borate glass. The experimental data (×) are compared with data from the literature (•). From the trend of the densities found in the literature, the real composition of the samples are estimated at $x = 0.36, 0.48,$ and 0.68. The uncertainty on the measurement is ± 0.001.

7.2.2 Results

Stress optic measurements and densities

The results of the density measurements are reported in Figure 7.3 and they are compared with data found in the literature [150, 215, 219–225]. By comparison with these data, the composition of the glass samples can be estimated at $x = 0.36, 0.48$ and 0.68 (± 0.05) which is fairly close to the nominal compositions. The values of the stress optic coefficient fulfill the expectations with values of 2.84, 0.85 and -1.96 Brewsters in order of increasing Sb_2O_3 content. The results are reported in Figure 7.4 in function of the compositions estimated from the densities. According to these values, a zero-stress optic glass can be achieved for the composition $(Sb_2O_3)_{0.55}$ - $(B_2O_3)_{0.45}$, which is a greater amount of Sb_2O_3 than previously reported [106]. The error of the empirical model is now 63%.

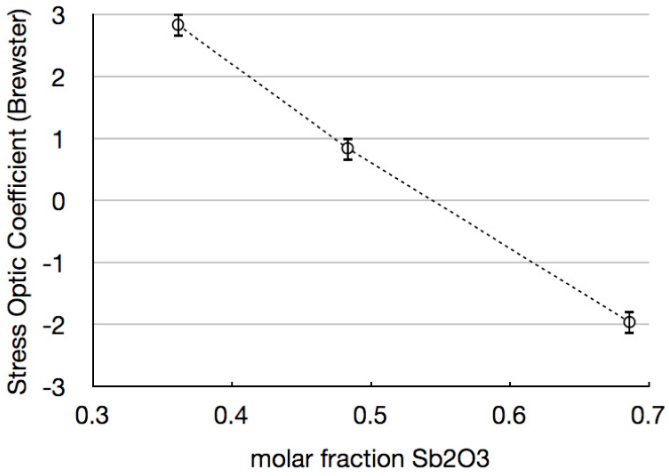

Figure 7.4: Stress optic coefficient of the antimony borate glasses. The molar fraction are calculated by comparing the densities with the literature. The zero-stress optic composition is found at $x = 0.55$.

^{11}B Nuclear Magnetic Resonance Spectroscopy

The spectra of the ^{11}B NMR experiments presented in Figure 7.5 reveal two peaks at about 15 ppm and 1.5 ppm attributed to $[BO_3]$ and $[BO_4]^-$ units respectively. The chemical shift and relative intensities from the peaks integration of the two boron species are presented in Table 7.3 in function of the composition estimated from the density measurements. The results are in good agreement with the literature [218, 226] with an maximum amount of $[BO_4]^-$ units at x $\sim$ 0.5.

7.2.3 Discussion

For this series of antimony borate glasses, the zero-stress optic composition was found to be at higher antimony content than the composition previously reported by Zwanziger *et al.* [106]. In this last publication, the samples were prepared in air at 1100°C therefore a partial oxidation of Sb(III) in Sb(V) can be assumed. In the two polymorph forms of Sb_2O_3 (orthorhombic and cubic), the $Sb - O$ bond length

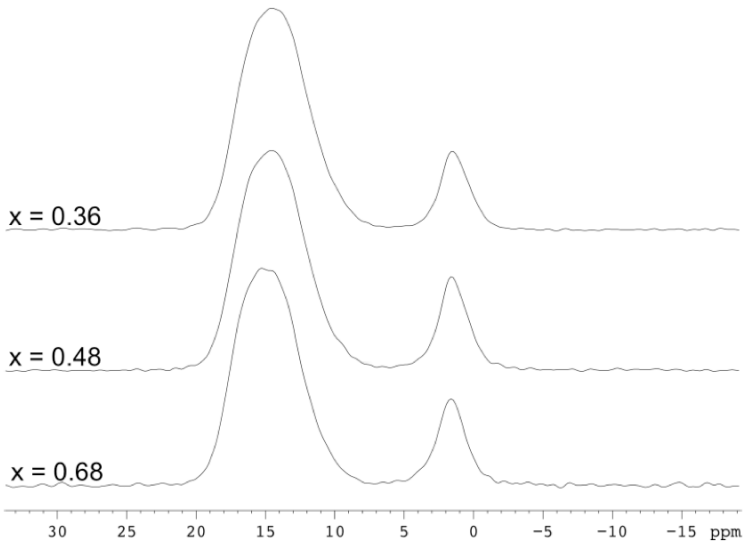

Figure 7.5: ^{11}B MAS NMR spectra for the antimony borate glasses. The molar fraction indicated corresponds to the molar fraction in Sb_2O_3 estimated from the density measurements.

is 2 Å and the antimony is on top of a triangle-base pyramid [227, 228]. In Sb_2O_5 the antimony is in the center of an octahedron site, and the mean $Sb - O$ bond length is also about 2 Å [229]. According to these data, the d/N_c ratio for Sb_2O_3 is 0.67 and 0.33 for Sb_2O_5. The preparation of a series of glasses under O_2-free atmosphere should reduce the value of the stress optic coefficient with respect to the results obtained by Zwanziger *et al.* The glass samples for the present work were prepared using the same drybox as for the preparation of the tin borophosphate glasses presented in section 6.3. The tin Mössbauer results revealed the presence of Sn(IV) in these glasses, therefore it can be assumed that a significant amount of oxygen remained in the drybox in spite of the 3 hour vacuum process. The presence of remaining oxygen during the synthesis of the antimony borate glasses would give rise to the oxidation of Sb(III) into Sb(V) and then would explain the variation of composition for the zero-stress optic glass. Attempts were made to perform ^{121}Sb Mössbauer spectroscopy but no results were obtained. These results would be of great

$x_{density}$	$[BO_3]$		$[BO_4]^-$	
	δ (ppm)	Relative intensity (%)	δ (ppm)	Relative intensity (%)
0.36	14.55	86.5	1.53	13.5
0.48	14.54	83.0	1.57	17.0
0.68	15.25	83.2	1.61	16.8

Table 7.3: ^{11}B MAS NMR chemical shifts and relative intensities for the antimony borate glasses

.

help in identifying and quantifying the antimony species present in the glass. The amount of $[BO_4]^-$ units in the glass is the highest for the sample at $x_{nominal} = 0.50$ in good agreement with the literature [226]. The evolution of the N_4 fraction in the antimony borate system is similar to the lead borate glasses, however the fraction of $[BO_4]^-$ units in the antimony glass is about five times less than in the lead glass. It can be suggested that the antimony is acting mainly covalently through the whole range of compositions, with a small fraction acting ionically at low Sb content. No solid conclusion can be made about the antimony's behavior without proper analysis of its local environment.

7.2.4 Conclusion

The synthesis of antimony borate glasses gave a negative stress optic coefficient at high antimony content. However the composition of the zero-stress optic glass composition is found at a higher Sb_2O_3 content than from the work of Zwanziger *et al.* [106] in spite of a preparation under O_2-free atmosphere. The ^{11}B MAS NMR study reveals a behavior similar to the lead in the lead borate system. No direct analysis of the antimony was performed, preventing any definitive conclusion about antimony's behavior and environment.

7.3 Antimony borophosphate

$(Sb_2O_3)_x$ - $(B_2O_3)_y$ - $(P_2O_5)_{1-x-y}$

In spite of the well-known properties of antimony to give a yellow color to the glass [217,230], compositions of antimony borophosphate glasses were synthesized for many reasons:

- The opportunity exists to obtain a transparent or slightly yellow glass.
- To find compositions with zero-stress optic properties or negative stress optic coefficient and to compare these results with the prediction of the empirical model.
- At high temperature Sb(III) in Sb_2O_3 is partially oxidized to Sb(IV) giving Sb_2O_4 [218], therefore by comparing results of samples prepared in air and samples prepared under O_2-free atmosphere, the contribution of antimony(III) and antimony(IV) could be evaluated.

7.3.1 Glass preparation

The samples were prepared under O_2-free atmosphere in a drybox filled with nitrogen. A box furnace, a hot plate, and all tools required to work at high temperature were transferred into the drybox. Due to space limitation, the balance and reagent could not be placed in the box. Therefore the reagents were weighted and mixed in air, then the crucibles were transferred into a drybox filled with nitrogen following the same procedure described in section 6.3.1.

The starting reagents Sb_2O_3 (Sigma-Aldrich, 99%), $NH_4H_2PO_4$ (Sigma-Aldrich, 98+%, A.C.S. reagent) and B_2O_3 (Sigma-Aldrich, 99%) were mixed in an alumina crucible and placed in a box furnace preheated to 300°C and then the temperature was increased by 100°C every 15 minutes until 600°C. This slow increase of temperature is required to avoid the mixture overflowing out of the crucible as explain in section 7.1.1 and to give more time for the ammonium dihydrogen phosphate to be

decomposed in phosphorus pentoxide by loss of water at 200°C and loss of water and ammonia at 488°C [214]. The mixtures were left between 30 to 60 minutes at 600°C, then the temperature was increased to 1050°C. After 30 minutes, the glass was quenched at room temperature or onto a hot plate up to 400°C depending on the composition. Most glasses were also placed back into a furnace or onto the hot plate at a temperature between 150°C and 400°C and slowly cooled down to room temperature by turning the heating device off. In a general way, glasses with a high content of antimony ($x \geq 0.45$) needed to be quenched at room temperature and glasses with a ratio $x_{B_2O_3}/x_{P_2O_5}$ lower than 0.8 or greater than 1.3 had to be slowly cooled to avoid cracking, breaking, or exploding in tiny pieces. The samples were annealed at a temperature between 400°C and 500°C. All the compositions which gave a glass are reported in Figure 7.6.

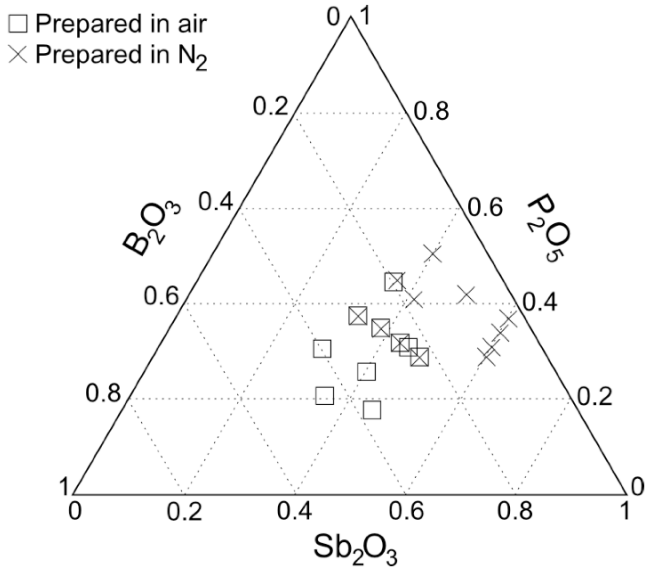

Figure 7.6: Nominal compositions of the antimony borophosphate glasses prepared in air and under O_2-free atmosphere.

7.3.2 Results and discussion

In order to keep a consistent organization to the work, the compositions were prepared with three specific $x_{B_2O_3}/x_{P_2O_5}$ ratios equal to 0.8, 1.3 and 2.2 for the glasses made in air; and 0.8 and 0.45 for the glasses prepared under O_2-free atmosphere. These compositions follow a line in the ternary diagram of the glass system (Figure 7.6) and different glass compositions were prepared along these lines corresponding to different amount of antimony oxide.

Surprisingly, most of the glasses prepared in air were transparent and colorless, even the samples with a significant amount of antimony oxide ($x = 0.45$). However, no glass with a negative stress optic coefficient or with zero-stress optic properties was found in the range of compositions tested, whereas the empirical model predicts the existence of zero-stress optic glass for molar fractions in Sb_2O_3 from 0.20 ($x_{P_2O_5} = 0$) to 0.41 ($x_{B_2O_3} = 0$).

As seen previously, the boron can adopt a trigonal or tetrahedral configuration however, the empirical model only takes into account the trigonal form of boron (only configuration in the crystalline B_2O_3). The d/N_c ratio for the tetragonal configuration is smaller than 0.5 Å (0.37 Å, coordination 4 and B-O bond length 1.47 Å [135]) therefore it should contribute to a positive stress optic coefficient. The preparation of the sample in air might also give rise to the presence of antimony(V) in the glass with a coordination number of 6 and an antimony-oxygen bond length of 1.99 Å, which also leads to a d/N_c ratio smaller than 0.5 Å. No ^{11}B NMR or ^{121}Sb Mössbauer spectroscopy were performed on these samples to detect and quantify the presence of boron 4-fold coordinated and antimony(V), but it can be assumed that their presence prevents the existence of zero-stress optic properties among these samples.

The amount of $[BO_4]^-$ units in the system is an intrinsic property of the material. In order to decrease this amount, another reagent such as Al_2O_3 has to be added to the composition, but this new reagent would also affect the photoelastic property of the glass. On the other hand, the elimination of Sb(V) can easily be performed by

preparing the glass under O_2-free atmosphere.

Twelve different compositions were prepared in a drybox filled with nitrogen. Two of these compositions crystallized, all of the others gave yellow transparent glasses. Only compositions giving a glass are reported on Figure 7.6. The difference of coloration between the glasses made in air and the ones obtained in the drybox might be due to a reduction of the amount of antimony(V) in the glass. In spite of the preparation in the drybox, none of the samples show zero-stress optic properties or a negative stress optic coefficient. The main objective of this project was to find new zero-stress optic compositions, but such glasses were not achieved with this glass system. No further analysis or work was performed on this glass system. Because of the differences between the predictions from the empirical model and the experimental values, the structural study of this glass system might be of scientific interest. The different species of boron and phosphorus can be easily and rapidly quantified by NMR. The presence and quantification of Sb(III) and Sb(V) can also be performed by Mössbauer spectroscopy. However antimony Mössbauer spectroscopy is experimentally harder to achieve than tin or iron Mössbauer spectroscopy. It also requires a longer time of acquisition per sample (usually many days). The study of this glass system over a wide range of compositions for glasses prepared in air and in a drybox would require many months, possibly years, to be completed.

7.3.3 Conclusion

No zero-stress optic composition was found for the antimony borophosphate glass system. The preparation of samples in air probably gives rise to the oxidation of Sb_2O_3 in Sb_2O_5, lowering the effect of the antimony in the glass. The samples prepared under O_2-free atmosphere had a brighter yellow color but still did not give zero-stress optic glass. No structural analysis was performed for these ternary glasses.

7.4 Summary

Among all the glass systems prepared for this thesis, the antimony-containing glasses were the hardest to study. The antimony phosphate system gives highly hygroscopic glasses which prevents their handling in air and limits the possibilities of analysis. However one sample prepared in air gave a negative stress optic coefficient, unfortunately its exact composition could not be obtained. The antimony borate system also gave a glass with a negative stress optic coefficient and the zero-stress optic composition was estimated to be at ∼55 mol-% Sb_2O_3. This amount of antimony oxide is much higher than the composition found by Zwanziger *et al.* and the value predicted by the empirical model [106]. No direct analysis of the antimony could be performed to detect the possible presence of Sb(V) in the glass. However the ^{11}B MAS NMR revealed similarities with the lead- and tin-borate glass systems but with a lower fraction. These results suggest a covalent nature for the antimony throughout the ranges of composition similar to the tin in the tin borate system. Many attempts were made to find zero-stress optic glasses in the antimony borophosphate system without success. Furthermore the glasses prepared under O_2-free atmosphere had a yellow color and are assumed to contain only Sb(III). No structural analysis was performed of these series of glasses.

Chapter 8

Zinc- and cadmium-containing glasses

From the crystal structure, the d/N_c ratio of P_2O_5 is equal to 0.38 Å, and this ratio is equal to 0.50 Å for ZnO [106]. The stress optic coefficient of pure P_2O_5 cannot be determined by the Sénarmont method of compensation. The application of a stress on the glass results on an inelastic deformation, but from lead-, tin- and antimony-containing glasses it clearly appears that pure amorphous P_2O_5 has a positive stress optic coefficient. Zinc oxide is a glass network modifier, not a glass network former. It cannot give a glass on its own, but hypothetically, a pure ZnO glass would have zero-stress optic properties according to the empirical model (Equation 3.14). It would be expected that the stress optic coefficient in the $(ZnO)_x$-$(P_2O_5)_{1-x}$ system becomes closer to zero as the molar fraction in ZnO increases, but it was reported that its value actually increases with x [29]. The addition of zinc oxide in a borate glass seems to decrease the value of the stress optic coefficient as expected from the empirical model [28]. The zinc phosphate glass system offers a chance to study a case where the trend given by the empirical does not fit the experimental results. The first goal is to study

the relationship between photoelasticity and structure in the zinc phosphate system $(ZnO)_x$-$(P_2O_5)_{1-x}$, as well as in the zinc borate glass system $(ZnO)_x$-$(B_2O_3)_{1-x}$ where the empirical model seems to be correct. In addition, cadmium phosphate $(CdO)_x$-$(P_2O_5)_{1-x}$ and cadmium borate $(CdO)_x$-$(B_2O_3)_{1-x}$ glasses were also prepared. The structure of the glass samples can be investigated by ^{31}P NMR, ^{11}B NMR and ^{113}Cd NMR; unfortunately the only NMR active zinc nuclei is ^{67}Zn, but its poor sensitivity usually results in broad signal (∼500 ppm) [231]. Also ^{67}Zn Mössbauer spectroscopy is experimentally challenging to perform due a low signal to noise ratio [232]. The study of the local environment of the zinc atoms was realized with the help of the literature.

8.1 Experiment

8.1.1 Glass preparation

Phosphate glass

The starting reagent to prepare these glasses were ZnO (Sigma-Aldrich, 99%), CdO (Sigma-Aldrich, 99%), and $NH_4H_2PO_4$ (Sigma-Aldrich, 98+%, A.C.S. reagent). The powders were mixed into an alumina crucible and placed in a preheated box furnace at 500°C for 4 hours; the crucible was then transferred in another box furnace between 1000°C and 1200°C depending on the composition. After 20 minutes the glass was quenched at room temperature onto a brass plate. The zinc-containing glass at 60 mol-% ZnO was quenched onto an aluminum plate cooled at 4°C. The cadmium-containing glass at 50 mol-% CdO was transferred into a furnace at 300°C after being quenched to avoid cracking. All of the samples were annealed in the range of temperature from 320°C to 375°C. Four zinc phosphate glasses $(ZnO)_x$-$(P_2O_5)_{1-x}$ with nominal composition $x = 0.30, 0.40, 0.50$, and 0.60 were obtained. For the cadmium phosphate system $(CdO)_x$-$(P_2O_5)_{1-x}$, three samples were obtained at nominal

compositions $x = 0.30, 0.40$, and 0.50. Attempts were made to prepare bulk samples with higher and lower amounts of additive, but the solids crystallized immediately during the quenching. All the glasses were transparent and colorless but contained bubbles.

Borate glass

The starting reagent to prepare these glasses were ZnO (Sigma-Aldrich, 99%), CdO (Sigma-Aldrich, 99%), and B_2O_3 (Sigma-Aldrich, 99%). The powders were mixed in a platinum crucible and placed in a preheated box furnace at about 1200°C. After 30 minutes, the glass was quenched onto a brass plate at room temperature and then immediately transfered onto a hot plate at 320°C. All the samples were annealed in the range of temperature from 490°C to 530°C. For the zinc borate system $(ZnO)_x$-$(B_2O_3)_{1-x}$, four samples were obtained with nominal compositions $x = 0.30, 0.40, 0.50$, and 0.60. For the cadmium borate system $(CdO)_x$-$(B_2O_3)_{1-x}$, three samples were obtained at nominal compositions $x = 0.40, 0.45$, and 0.50. All the glasses were transparent and colorless.

8.1.2 Composition analysis

The samples were analyzed by Double-EDS analysis at the Microprobe laboratory (Dalhousie University - Earth Science Department) to obtain an accurate analysis of the composition. Unfortunately all the glasses were damaged by the measurements. During the measurement the surface of the glass that received the electron beam burnt and released gases. After many trials, no relevant analysis was obtained. The gas released at the impact location is probably due to water absorbed by the samples, and in the case of the phosphate glasses, water and ammonia trapped in the glass (from the decomposition of $NH_4H_2PO_4$).

8.1.3 Density measurements

The density was measured only for the zinc and cadmium borate glasses. The density measurements for the phosphate glasses would not be relevant because of the presence of bubbles inside the samples. All sample density measurements were performed using the Archimedes principle. The immersion liquid used was 99+mol% ethanol. Water was not used because of the hygroscopic character of the glasses. Due to the slight variation of the density of ethanol depending on temperature, a series of values for the density of ethanol were taken from the literature [128].

8.1.4 Stress optic measurements

The stress optic coefficient of each samples was determined by the Sénarmont method of compensation described in section 4.1. The measurements for all the samples presented in this section were performed only with the light table.

8.1.5 ^{11}B Nuclear Magnetic Resonance Spectroscopy

All samples were crushed and packed in 2.5 mm rotors. The ^{11}B magic angle spinning (MAS) NMR was performed on a Bruker Avance NMR spectrometer with a 16.4 T magnet (700 MHz proton Larmor frequency, 224.68 MHz ^{11}B Larmor frequency). The samples were spun at 10 and 22 kHz to determine center bands and to identify spinning sidebands. The $NaBH_4$ resonance served as a secondary chemical shift standard at -42.1 ppm relative to $BF_3.Et_2O$ and was used to determine the pulse power. For the ^{11}B MAS NMR spectrum 64 scans were accumulated using a pulse length of 0.4 μs at 78 kHz amplitude strength, chosen short for uniform excitation. Pulse repetition times between 1 and 5 s were determined to be sufficient for these samples. Because of the substantial boron background, mostly from the rotors, the spectrum of an empty rotor was subtracted.

8.1.6 ^{31}P Nuclear Magnetic Resonance Spectroscopy

The ^{31}P NMR experiments were performed on a Bruker Avance NMR spectrometer with a 9.4 T magnet (162.02 MHz ^{31}P Larmor frequency) using a magic-angle spinning probe and 2.5 mm diameter sample rotors. The ^{31}P NMR chemical shift scale was referenced externally against $NH_4H_2PO_3$ at 0.81 ppm as a secondary reference. The 90 degree pulse time was also determined on this sample. The final 1-d magic-angle spinning spectra were acquired with a pulse of 0.75 μs (corresponding to a 20 degree flip angle) at 74 kHz rf field strength and 60 s recycle delay. Samples were spun at 25.0 kHz. Line shape simulations were performed using the program Dmfit [160] and XEDPLOT (Bruker software package).

8.1.7 ^{113}Cd Nuclear Magnetic Resonance Spectroscopy

All ^{113}Cd magic angle spinning (MAS) NMR experiment were carried out on a Bruker Avance NMR spectrometer with a 9.4 T magnet (400.24 MHz proton Larmor frequency, 88.769 MHz ^{113}Cd Larmor frequency) using a probe head for 4 mm rotor diameters. The samples were spun at 12.00 kHz. Between 2040 and 2400 scans were accumulated with single pulse excitation using a pulse length of $\pi/4$ at 54 kHz rf field strength. The recycle delays were 30 s following the reference of Hussin [233]. The chemical shift scale was referenced externally against 0.1 molar $Cd(ClO_4)_2 \cdot 6\,H_2O$.

8.2 Results

8.2.1 Density measurements

The results of the density measurements for the borate glasses are shown in Figure 8.1, and they are compared with data from the literature in each case [150, 215, 234–244]. For both systems the density increases significantly with the addition of a glass modifier. At low nominal ZnO content, the densities for the zinc borate glasses

are too high, and an estimation of the real compositions can be calculated from the trend of the values. According to this method, the composition for the Zn-containing glasses at $x = 0.30, 0.40, 0.50$, and 0.60 are closer to $x = 0.51, 0.58, 0.61$, and 0.63 respectively. For the Cd-containing glasses, only the sample at $x = 0.45$ does not agree with the literature. According to the trend its real composition is actually closer to $x = 0.54$.

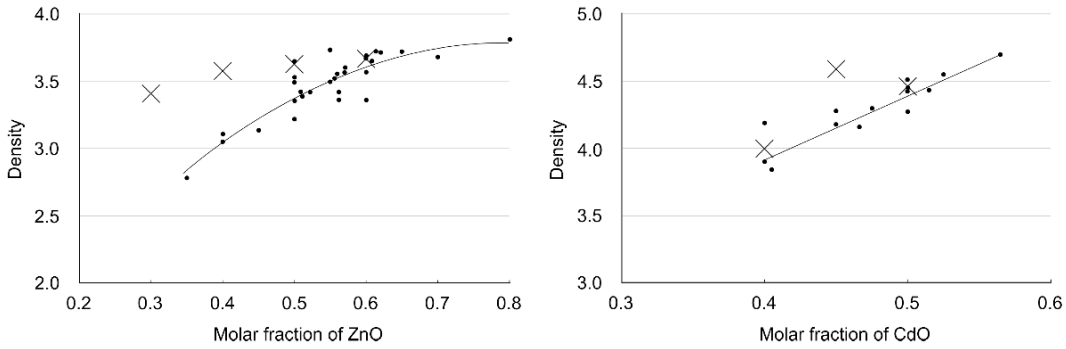

(a) Zinc glasses (b) Cadmium glasses

Figure 8.1: Densities of the zinc borate glass (a) and cadmium borate glass (b) in function of their nominal compositions. The experimental values (×) are compared with data from the literature (•) [150,215,234–244] and a trend is plotted from these data (solid line). The uncertainty on the measurements is ±0.001.

8.2.2 Stress optic measurements

The stress optic coefficient was determined for all the samples except the cadmium borate at $x = 0.45$. This last sample was not homogeneous enough to give a consistent value of C. The density was measured only for the borate glasses, therefore the choice was made to plot the stress optic coefficients in function of the nominal compositions in order to plot the results for the borate and the phosphate glasses. The results for the zinc-containing glasses are plotted on Figure 8.2. Furthermore, these glasses are compared with the value obtained by Matusita *et al.* [28, 29] who

prepared their samples according to an experimental procedure close to the procedure presented above. It can be expected that the differences between nominal and real composition of Matusita's glasses and the present samples might be of the same amplitude. Matusita *et al.* did not provide any compositional analysis of their glasses. Their results are given in function of the nominal composition.

From both zinc and cadmium phosphate glasses, the stress optic coefficient in-

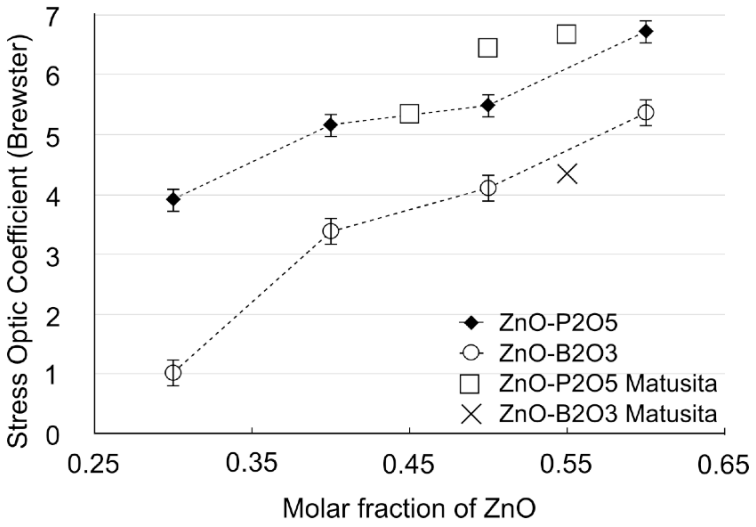

Figure 8.2: Stress optic coefficient of the zinc-containing glasses in function of their nominal compositions. The experimental values are compared with data from Matusita *et al.* [28, 29] and a trend is plotted from these data (solid line).

creases with the amount of additive. A decrease was expected from the empirical model. The stress optic coefficients for the zinc phosphate glasses are in fairly good agreement with the work of Matusita *et al.*. The value of the coefficient for the cadmium phosphates at $x = 0.40$ and 0.50 are identical, with values of 4.66 and 4.64 Brewsters respectively. The case of two binary glasses of the same system with different compositions and the same stress optic coefficient has not been observed so far. It is more likely that these two cadmium phosphate glasses have the same composition. The stress optic coefficient of the zinc borate also increases with the addition of zinc in the glass, following a similar trend to the zinc phosphate. Among

the four series of samples, only the cadmium borate sees its stress optic coefficient decreasing with the addition of glass modifier.

8.2.3 ^{11}B Nuclear Magnetic Resonance Spectroscopy

The ^{11}B Nuclear Magnetic Resonance spectroscopy spectra for the zinc and cadmium glasses all contained one peak at about 15 ppm and one peak at about 1 ppm corresponding to $[BO_3]$ and $[BO_4]^-$ respectively. The position and relative intensity of each peak (from the area integration) are reported in Table 8.1. As the amount of additive increases the position of both peaks are shifted downfield. The values for the cadmium glass at $x = 0.45$ and 0.50 are very close, contributing to the conclusion that the two samples might have a similar composition, as previously suggested by the density measurements. For the zinc borate glass, the fraction of $[BO_3]$ units increases with the addition of ZnO in good agreement with the work of Kajinami *et al.* [246], whereas it decreases in the cadmium borate glasses.

x	$[BO_3]$		$[BO_4]^-$	
(nominal)	δ (ppm)	Fraction (%)	δ (ppm)	Fraction (%)
$(ZnO)_x$-$(B_2O_3)_{1-x}$				
30	14.61	65.7	0.81	34.3
40	14.66	68.0	0.99	32.0
50	15.12	70.8	1.13	29.2
60	15.14	72.4	1.15	27.6
$(CdO)_x$-$(B_2O_3)_{1-x}$				
40	14.62	51.3	0.59	48.7
45	15.58	46.7	0.92	53.3
50	15.32	47.0	0.86	53.0

Table 8.1: ^{11}B NMR data for the zinc- and cadmium-containing glasses. Both glass systems are fitted with one peak corresponding to $[BO_3]$ ($\sim$ 15 ppm) and one peak corresponding to $[BO_4]^-$($\sim$ 1 ppm).

8.2.4 ^{31}P Nuclear Magnetic Resonance Spectroscopy

The ^{31}P Nuclear Magnetic Resonance spectroscopy revealed the presence of Q^3, Q^2 and Q^1 phosphorus in all the samples for both zinc and cadmium glasses (Table 8.2) in good agreement with the literature [233, 247, 248]. In the zinc phosphate the amount of Q^3 species decreases significantly with the addition of ZnO. This variation is first balanced by the increase of Q^2, and then by the sudden raise of Q^1 at high zinc content. In the cadmium glasses, the samples at $x = 0.30$ and 0.40 show a close similarity to their phosphorus species with a majority of Q^2 species and a significant amount of Q^3. $[PO_4]$ units with only one bridging-oxygen are barely present in these two glasses. The number of Q^1 species increases significantly at $x = 0.50$ and the amount of Q^1 units created is very close to the number of Q^3 that disappeared.

x	Q^3		Q^2		Q^1	
(nominal)	δ (ppm)	Fraction (%)	δ (ppm)	Fraction (%)	δ (ppm)	Fraction (%)
$(ZnO)_x$-$(P_2O_5)_{1-x}$						
30	-45.12	35.8	-33.89	61.6	-14.60	2.61
40	-43.72	21.4	-32.28	74.5	-16.46	4.1
50	-46.43	1.9	-30.90	90.8	-13.78	7.3
60	-52.51	1.3	-30.75	68.6	-12.39	30.1
$(CdO)_x$-$(P_2O_5)_{1-x}$						
30	-44.73	36.5	-31.29	61.3	-12.73	2.2
40	-42.51	27.5	-28.73	70.7	-12.77	1.8
50	-34.81	17.2	-25.7	72.4	-6.40	10.39

Table 8.2: Assignment of the Q^n species from the ^{31}P NMR chemical shifts. Both glass sytems contain Q^3, Q^2 and Q^1 species. The fraction of Q^3 decreases whereas the number of Q^1 increases with the increase of additive in the phosphate glass.

8.2.5 ^{113}Cd Nuclear Magnetic Resonance Spectroscopy

The ^{113}Cd Nuclear Magnetic Resonance spectroscopy was successfully performed on five samples. Each spectrum shows a broad peak shifted from lower to higher chemical shift as the cadmium is added to the composition (Figure 8.3). A deconvolution

of the peaks into several gaussians was not performed here because of a low signal to noise ratio, especially for the phosphate glasses. Only one gaussian was used to fit each spectrum, even in the case of the $(CdO)_{0.40}$-$(B_2O_3)_{0.60}$ where the spectra seems to be a combination of two components. This provides a general trend of the cadmium's behavior through the different compositions. The chemical shift and width of the peaks are reported in Table 8.3.

x (nominal)	δ (ppm)	FWHM (ppm)
$(CdO)_x$-$(P_2O_5)_{1-x}$		
30	-90	116
40	-61	139
50	-61	128
$(CdO)_x$-$(B_2O_3)_{1-x}$		
40	-31	263
50	12	263

Table 8.3: Chemical shift and width of the gaussian used to fits the ^{113} Cd NMR spectra.

8.3 Discussion

Once again, the composition analysis of the glasses produced some difficulties related to the hygroscopic nature of the samples, and the possible presence of gas trapped close to the surface. The density measurements gave an idea of the final composition of each sample and their deviation from the nominal composition for the borate glasses. For the zinc borate, the samples seem to have a higher amount of ZnO than expected. This might be due to the loss of some B_2O_3 by volatilization at high temperature. In spite of these differences of composition, the sample at $x = 0.30$ is still the one with the least ZnO and the sample at $x = 0.60$ the one with the most ZnO. This is not the case for the cadmium borate system. The real compositions for the samples at $x = 0.30$ and 0.50 are quite close to their nominal compositions, but

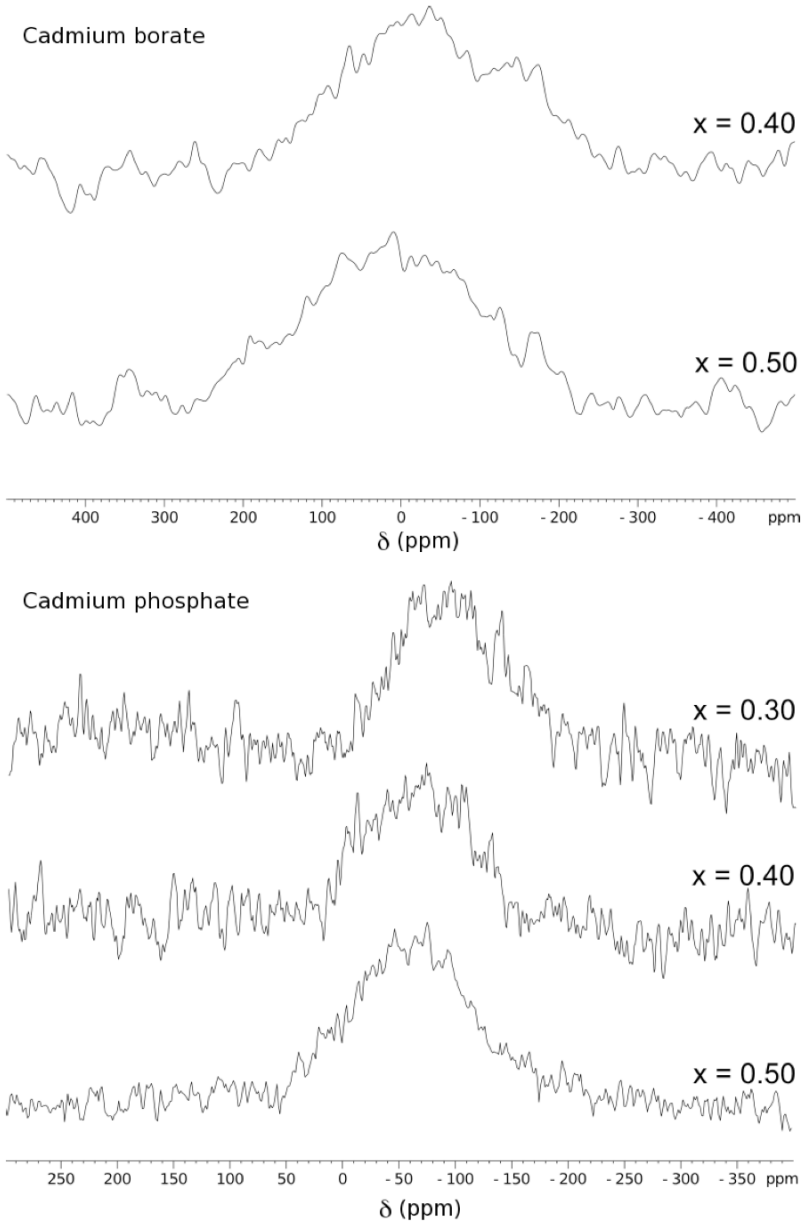

Figure 8.3: ^{113}Cd NMR spectra for the borate and phosphate glasses.

for the one at 45 mol-% the real amount of ZnO is estimated at ∼54 mol-%. From the crystalline structure of the zinc oxide and the cadmium oxide, their d/N_c ratio is calculated at 0.50 Å and 0.38 Å respectively [106, 249].

The structure of the zinc phosphate glass was studied using X-ray and neutron diffraction, Nuclear Magnetic Resonance spectroscopy, and molecular dynamics [248, 250–254]. All studies agreed on the stability of the coordination number and oxygen's bond length of both cations for the whole range of compositions (typically $0.35 \leq x \leq 0.70$). The coordination number of phosphorus was found at 4 and the $P-O$ bond length at 1.5 Å, which is typical of phosphate glasses as mentioned in previous sections (section 5.2.2, and section 6.1). The $Zn-O$ bond length is subject to minor variations from 1.94 Å at low zinc content to 2.00 Å at high zinc content [253]. Discussion still exists about zinc's exact coordination number in this glass system. Most of the studies agree on the fact that the zinc is in coordination 4 similar to the ZnO crystal structure [248, 250–253]. A recent study using x-ray and neutron diffraction determined a coordination close to 5 in the range of composition $0.49 \leq x \leq 0.70$, with the presence of $[ZnO_5]$ polyhedra in the structure [254]. With a coordination 4 and a bond length 1.94 Å the d/N_c ratio for the zinc atom is 0.49 Å; with a coordination 5 and the same bond length this ratio becomes 0.39 Å. The d/N_c ratio for P_2O_5 is 0.38 Å, therefore in the case of coordination 4 for the zinc, the addition of ZnO should slightly increase the results of the empirical model, which means that the stress optic coefficient should slightly decrease. In the case of a coordination 5 for the zinc, the d/N_c ratio for both cations is almost identical, therefore the addition of ZnO in the glass should not affect the value of the stress optic coefficient. None of these situations can explain the significant variation of the stress optic coefficient of the zinc phosphate system.

In the zinc borate glass system, the coordination number for zinc and $Zn-O$ bond length also remain constant through the different compositions ($0.40 \leq x \leq 0.65$) with values of 4 and 2.00 Å respectively [246]. According to the NMR results, the

empirical model becomes:

$$(1-N_4)(1-x)\frac{d(\mathrm{B_3})}{3}+(N_4)(1-x)\frac{d(\mathrm{B_4})}{4}+x\frac{d(\mathrm{ZnO})}{N_c(\mathrm{ZnO})}=0.5\ \text{Å} \qquad (8.1)$$

where the value of the N_4 fraction corresponds to the fraction of $[BO_4]^-$ given in Table 8.1, x is the molar fraction of ZnO, d(B_3) and d(B_4) are the $B-O$ bond length in $[BO_3]$ and $[BO_4]^-$ respectively, d(ZnO) is the $Zn-O$ bond length, and N_c the zinc's coordination number. The results of this equation are reported in Table 8.4 based on the nominal composition ($x_{nominal}$) and the compositions deduced from the densities ($x_{density}$). The results given by the empirical model increase with the addition of ZnO to become closer to 0.5 Å. Therefore the stress optic coefficient should slightly decrease but, once again, this is not the case.

$x_{nominal}$	Empirical Model (Å)	$x_{density}$	Empirical Model (Å)
0.30	0.448	0.51	0.464
0.40	0.457	0.58	0.470
0.50	0.465	0.61	0.473
0.60	0.473	0.63	0.475

Table 8.4: Results of the empirical model for the zinc borate glass for the nominal compositions and estimated compositions from the densities.

The structure of the binary cadmium phosphate glass system is not very well known, and the most complete work about it was published by Hussin *et al.* who studied the structure using ^{31}P MAS NMR, ^{27}Al MAS NMR and ^{113}Cd Static and MAS NMR experiments [233]. They were able to obtain an accurate composition analysis of their samples prepared in the range $0.25 \leq x \leq 0.60$. The results from the ^{31}P NMR experiment presented in Table 8.2 are in good agreement with their work. By comparing the fraction and chemical shifts of the Q^n species, it can be estimated that the composition of the samples from the present work are quite close to their nominal compositions with a deviation of the CdO molar fraction of $\pm 5\%$. The ^{31}P NMR shows a decrease of the number of bridging oxygens, but as mentioned

earlier, the coordination number and $P-O$ bond length remains constant for the phosphorus atom in phosphate glasses. The ^{113}Cd NMR spectra are also in good agreement with the work of Hussin *et al.*, unfortunately no accurate data about the evolution of the cadmium's coordination number and $Cd-O$ bond length can be extracted from the spectra. Therefore no attempt was made to correlate the glass structure with the results of the empirical model. These spectra reveal an increase of the mean chemical shift similar to the lead NMR spectra for the lead borate system. Conversely to this last system, the increase of the chemical shift is associated with an increase of the stress optic coefficient. From the shape and mean chemical shift of the two samples at $x = 0.40$ and 0.50, it can be stated that these two samples have the same structure and composition as assumed from the stress optic coefficient values.

The data obtained from the ^{11}B NMR and ^{113}Cd NMR spectroscopy are not sufficient to test the empirical model, or to make any conclusion about the evolution of the cadmium's behavior within the composition. No relevant additional data were found in the literature to help understand the photoelastic response of this glass system. In this case, the variation of the chemical shift does not appear as clearly as in the cadmium phosphate glass. More investigations are required to know the exact local environment of the cations, especially the zinc.

8.4 Summary

For the four glass systems $(ZnO)_x$-$(P_2O_5)_{1-x}$, $(CdO)_x$-$(P_2O_5)_{1-x}$, $(ZnO)_x$-$(B_2O_3)_{1-x}$, and $(CdO)_x$-$(B_2O_3)_{1-x}$, the empirical model is unable to predict the evolution of the photoelastic response. The structure of the zinc phosphate glasses remains very stable throughout the range of compositions, the coordination and bond lengths for the two cations remains constant. In the zinc borate, the local environment of the zinc atom also remains stable through the compositions, only the N_4 fraction undergoes

slight variations. These variations cannot explain the evolution of the stress optic coefficient. The study of the Cd-containing glasses did not provide the information necessary to explain the photoelasticity of the borate and phosphate glasses.

Chapter 9

Discussion

9.1 The theory of photoelasticity

9.1.1 Mueller's theory of photoelasticity

The correlation between the structure and the photoelastic response of lead-, tin-, and antimony-containing glasses presented in the previous chapters reveals the dominant covalent nature of these three elements in glasses with a negative stress optic coefficient. These results contradict the expectations arising from Mueller's theory of photoelasticity which states that the cation brought by the oxide modifier should act mostly ionically in a glass with a negative stress optic coefficient. Mueller based his work on the previous independent attempts of Hertzfeld [104, 105] and Banerjee [103] to explain the origin of the photoelasticity in NaCl and KCl crystals. In these works, the structural deformation of the lattice under pressure was considered to be the only phenomenon occurring in the crystals. This deformation was called *"lattice effect"* by Mueller who introduced another effect corresponding to the deformation of the electronic clouds due to the motion of the atoms in the structure, some bonds being

strengthened and others weakened [26]. This second effect, called the *"atomic effect*, was added to explain the difference between the calculations taking into account the lattice effect only and the experimental values. To be rigorous it would be necessary to calculate independently the contribution of both effects, but technical limitations made it impossible to calculate the atomic effect. Therefore, to derive his theory, Mueller calculated the contribution of the lattice effect and compared it with the experimental data. The difference was assumed to be the atomic effect's contribution. This procedure is risky because it requires a perfect knowledge of the mechanics related to the lattice deformation, and any mistake in the calculations can invalidate the entire theory. Unfortunately a major error was introduced at the very beginning of Mueller's derivation of the theory with a misinterpretation of the lattice's deformation. Twice in his article from 1938, Mueller stated that under a tensile stress the *"distance between the neighboring atoms becomes larger in the direction of strain, while it does not change in the direction normal to it"* [26]. The Poisson's coefficient ν of a material under stress is given by the ratio of its deformation in the direction normal to the stress over the deformation parallel to the stress:

$$\nu = -\frac{\frac{\Delta l_n}{l_n}}{\frac{\Delta l_p}{l_p}} \tag{9.1}$$

with l_n and l_p lengths of the samples normal and parallel to the stress respectively. According to this equation and Mueller's statement, the Poisson's ratio of NaCl and KCl should be zero, but these ratios for the two crystals are in fact 0.164 and 0.101 respectively [255].

9.1.2 Weyl's model

The model of deformation of the ions in the stressed glass does not follow a simple expansion in the direction of the strain as suggested by Mueller (see Figure 3.5). Weyl proposed another model taking into account the electrostatic interactions between

anions and cations [256]. In this model, the sign of the electric charge and the polarizability of the ions are the main parameters defining the photoelastic response of a material. The electrostatic strength between two point charges can be described by the Coulomb's law:

$$F = \frac{q_+ q_-}{4\pi r^2 \epsilon_0} \tag{9.2}$$

where q_+ and q_- are the charge of the cation and the anion, r is the distance between the two charged particles and ϵ_0 is the permittivity of vacuum. When a tensile stress is applied on the material, the distance between the ions increases in the direction of the stress and decreases in the direction normal to it. Therefore the electrostatic interaction is strengthened in the direction perpendicular to the stress and weakened in the direction of the stress. To simplify the concept, it will be first assumed that the cation are rigid particles and only anions can be deformed because of their greater polarizability. In this case, the electronic cloud of the oxygens will be elongated in the direction perpendicular to the tensile stress because of the stronger interaction (see Figure 9.1 b). With such a configuration, shorter bonds and elongation of the electronic cloud, the electron density in the direction perpendicular to the stress becomes greater than the density in the direction of the stress. In the case of a glass containing polarizable cations, such as Pb^{2+}, the deformation of the electronic cloud of the oxygens remains the same as in Figure 9.1 b. The cations are subjected to the high and close electron densities of the anions and their electrons are repelled in the direction of the strain (Figure 9.1 c).

9.1.3 The Polarizability ratio

According to Weyl, in absence of polarizable cations, the sign of the birefringence is given by the direction of the deformation of the anions and becomes positive [256]. Weyl's model highlights the importance of the polarizability of the ions and two parameters influencing the atomic effect can be distinguished: the polarizability and the polarizing power. The polarizability is the ability of the ion to be deformed and

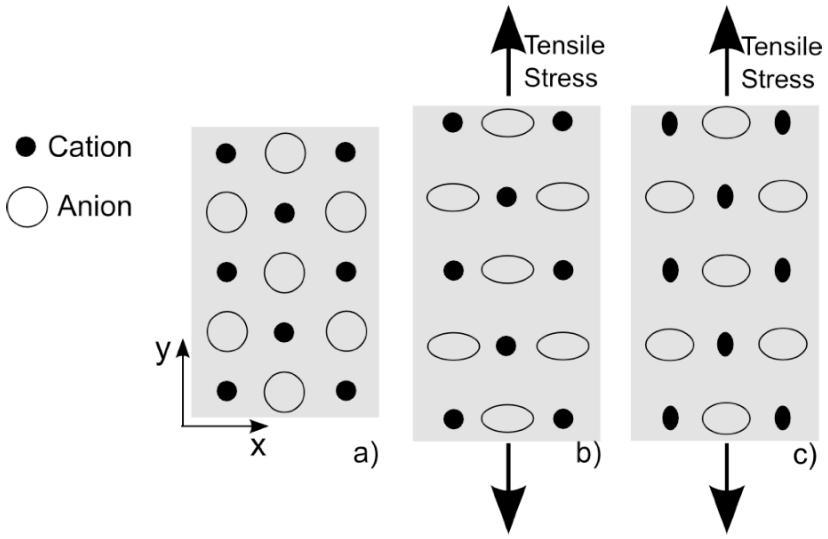

Figure 9.1: Deformation of the electronic cloud of anion and cations according to Weyl's model.

it is defined by:

$$\alpha = \frac{p}{E} \tag{9.3}$$

with p the induced dipole and E the external electric field. The polarization is often given in $Å^3$. The polarizing power is the ion's ability to deform the surrounding ions and is defined by:

$$P = \frac{z}{r^2} \tag{9.4}$$

with z the formal charge and r the ionic radius.

These two effects are related to each other: a small ion with a high charge (*"rigid"* ion) would have a small polarizability but a strong polarizing power, whereas a large ion with a small charge (*"soft"* ion) would have a high polarizability but a poor polarizing power. It is important to separate these two characteristics.

By definition the birefringence is the result of the difference between the extraordinary and ordinary refractive indices. The refractive index can be calculated from the Drude-Voigt formula of dispersion [257]:

$$n^2 - 1 = \frac{4\pi N e^2}{m} \sum_i \frac{f_i}{\omega_i^2 - \omega^2} \tag{9.5}$$

with n the refractive index, N is the number of molecule per unit volume, e and m are the electronic charge and mass respectively, f_i is the oscillator strength of the resonant electrons, ω_i is the resonance frequency of electrons i and ω is the considered frequency. The term Nf_i represents the number of resonant electrons per unit volume, or electron density, therefore if the electron density increases, the refractive index increases. In the case of a rigid cation, the application of a tensile stress increases the electron density in the ordinary direction, the ordinary refractive index becomes greater than the extraordinary refractive index, and the birefringence becomes negative ($\Delta n = (n_e - n_o)$) and not positive as stated by Weyl. According to Equation 3.11, if a tensile stress ($\sigma < 0$) induces a negative birefringence, the stress optic coefficient has to be positive which is the case for all glasses with small and charged cations. The three glass formers SiO_2, B_2O_3 and P_2O_5 contain rigid cations and have a positive stress optic coefficient; 3.47 and 11 Brewsters for the silicate and borate glasses respectively [27,28]. The stress optic coefficient of the phosphate glass cannot be determined experimentally because of its softness. The substitution of rigid cations by softer cations would decrease the ordinary electron density because of a lower polarizing power, and it would increase the extraordinary electron density because of the higher polarizability. To verify this statement, a relation between the polarizability of the cations and the stress optic coefficient of some glass formers can be made. Because all glasses are oxide glasses, it could be assumed that the effect of the oxygens would be the same in all glasses. Dimitrov *et al.* created a classification of oxides based on the polarizability of their ions, and it appears from their work that the oxygen's polarizability varies from oxide to oxide [258, 259]. Therefore, for an oxide of formula M_xO_y, the contribution to the photoelastic response called ξ would be given by:

$$\xi = \frac{x\alpha_M}{y\alpha_{O^{2-}}} \tag{9.6}$$

with α_M and $\alpha_{O^{2-}}$ the polarizability of the cation and the oxygen respectively in the oxide. The number of each ion brought by the oxide has to be taken into consideration because of their contribution to the extraordinary and ordinary electron densities. According to the previous statements, it is expected to obtain low ξ values for positive stress optic coefficients and increasing values with decreasing stress optic coefficient. The ξ ratio is calculated for some glass formers from the data given by Dimitrov *et al.* and the results are shown in Table 9.1. The stress optic coefficients C of B_2O_3, SiO_2 and TeO_2 are already known fom the literature [27,28,107], they are also reported in Table 9.1. The value of the stress optic coefficient seems to decrease

Oxide M_xO_y	α_A (Å^3) [259]	$\alpha_{O^{2-}}$ (Å^3) [259]	$\xi = \frac{x\alpha_A}{y\alpha_{O^{2-}}}$	C (Brewsters)
B_2O_3	0.002	1.345	0.0018	11 [28]
P_2O_5	0.021	1.350	0.0062	
SiO_2	0.033	1.427	0.0116	3.47 [27]
V_2O_5	0.122	2.643	0.0185	
GeO_2	0.137	1.720	0.0398	
TeO_2	1.595	2.401	0.3322	0.64 [107]

Table 9.1: Polarizability ratio and stress optic coefficient of some glass formers

with the increase of the ξ ratio. To verify this assumption the stress optic coefficient of additional glass formers needs to be determined. A germanium dioxide glass was successfully prepared according to the procedure of Sakaguchi *et al.* [260]. If the trend given by the ξ ratio is reliable, the value of the stress optic coefficient for GeO_2 should be close but smaller than the stress optic coefficient of the silicon dioxide. The synthesis of a pure V_2O_5 requires ultra-fast quenching techniques and could not be achieved [261]. As mentioned previously, the stress optic coefficient of pure P_2O_5 cannot be determined experimentally with the Sénarmont method. Therefore, only the stress optic coefficient of the germanium dioxide could be measured and it was found to be 3.01 ± 0.05 Brewsters in good agreement with the expectation. The stress optic coefficient is plotted in function of the ξ ratio in Figure 9.2. The ξ ratio is given on the x-axis on a logarithmic scale. Although only four points can be plotted, the

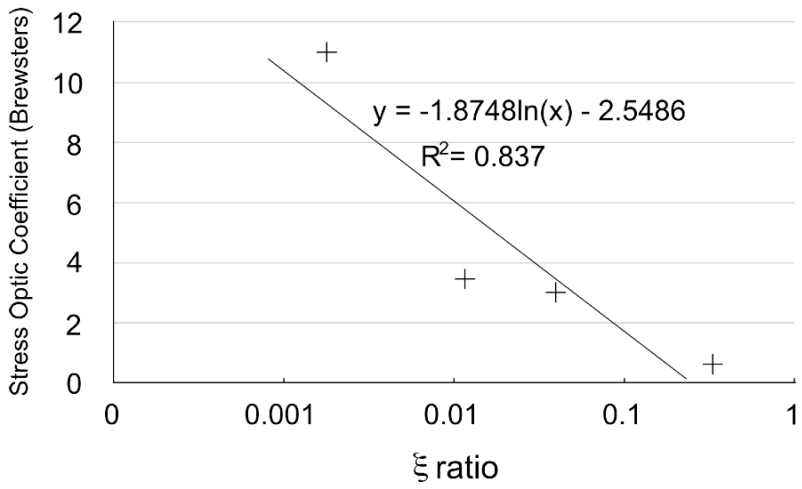

Figure 9.2: Polarizability ratio ξ and stress optic coefficient of some glass formers. The ξ ratio are given on a logarithmic scale.

graphic in Figure 9.2 shows that the stress optic coefficient roughly follows a natural logarithm trend. Therefore, the ξ ratio might give an idea of the contribution on the photoelastic response of a glass for each oxide, similar to the d/N_c ratio in the empirical model. A low value of the ξ ratio means a high contribution of the oxygens' deformation, that is to say a contribution to positive stress optic coefficient, and a high ξ value means a contribution to a low stress optic coefficient. The values for the ξ ratio for six MO type oxides (M = Mg, Ca, Sr, Ba, Sn, and Pb) are presented in Table 9.2 and the value e^{ξ} is also calculated to provide an simpler way to compare the numerical results: a value of 1 results in a poor cationic polarizability and a poor contribution to a decreasing stress optic coefficient. The higher the e^{ξ} value, the stronger the contribution to decrease the stress optic coefficient. The stress optic coefficient of binary $(MO)_x$ - $(P_2O_5)_{1-x}$ glasses of the same compositions are compared in Figure 9.3. The ratio of the cation and oxygen polarizabilities indicates that the contribution to a negative stress optic coefficient of the oxides increases in the order MgO < CaO < SrO < BaO < SnO < PbO. These results are in perfect agreement with the experimental values shown in Figure 9.3. In a similar way as

the empirical model, the e^{ξ} value is tested to see if a specific value characterizes the zero-stress optic coefficient with the formula $\sum_i x_i e^{\xi}$. The results varies from 1.42 for the 17 BaO - 83 TeO_2 glass to 1.80 for the 49 PbO - 51 B_2O_3 glass, therefore this model does not bring any improvement compared to the empirical model.

Oxide MO	α_M (Å^3)	$\alpha_{O^{2-}}$ (Å^3) [259]	$\xi = \frac{x\alpha_A}{y\alpha_{O^{2-}}}$	e^{ξ}
MgO [259]	0.094	1.687	0.056	1.057
CaO [259]	0.469	2.420	0.194	1.214
SrO [259]	0.861	3.150	0.273	1.314
BaO [259]	1.595	3.741	0.426	1.532
SnO [262]	2.587	3.179	0.814	2.257
PbO [259]	3.623	3.381	1.073	2.623

Table 9.2: e^{ξ} value of some simple oxides

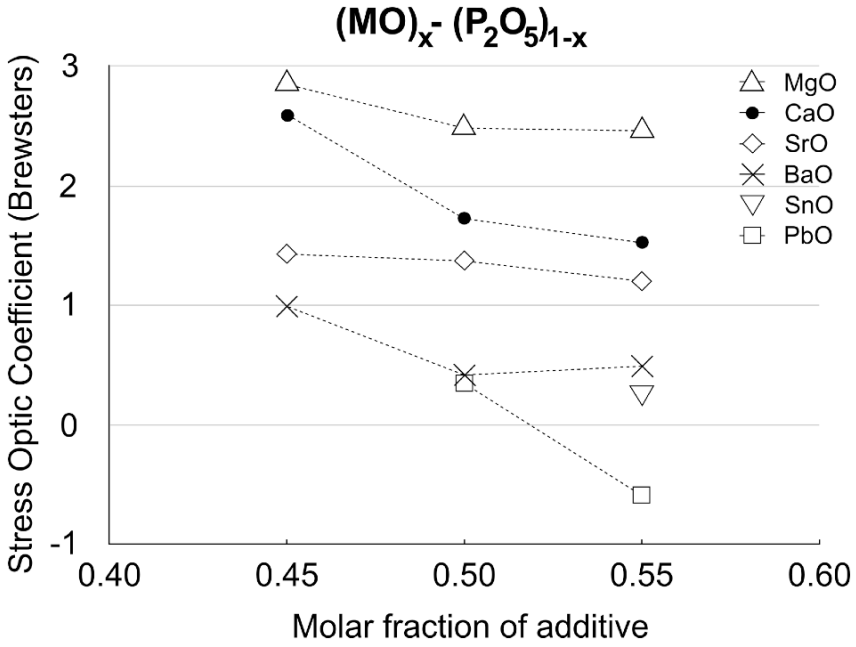

Figure 9.3: Stress optic coefficient in binary $(MO)_x$ - $(P_2O_5)_{1-x}$ glasses with M = Mg, Ca, Sr, Ba, Sn, and Pb [29, 106, 150, 151].

However, the estimation of the contribution of the oxides from the ξ ratio seems to give better results than the d/N_c ratio. For example, Zwanziger *et al.* demonstrated that the glass composition 17 BaO - 83 TeO_2 gives a zero-stress optic coefficient [107]. The d/N_c ratio for BaO and TeO_2 is 0.46 Å and 0.50 Å respectively, therefore the addition of BaO in a telluride glass should slightly increases the stress optic coefficient, whereas it decreases it. The e^{ξ} value for BaO is 1.532 and 1.394 for the tellurium dioxide, therefore the contribution of BaO to decrease the stress optic coefficient is stronger than TeO_2, consequently the addition of barium oxide should decrease C as observed experimentally. The photoelastic response is related to the polarizability of the oxides, and Weyl's model is verified experimentally, but this model concerns only the ionic deformation.

9.1.4 Deformation of covalent bonds

From the experiments presented in this thesis, two important conclusions can be made about the correlation of the glass structure and the photoelastic response of the lead-, tin-, and antimony-containing glasses:

- In the case of a positive stress optic coefficient, the metallic element brought by the oxide modifier can act either ionically (lead-containing glass) or covalently (tin-containing glass).
- In the case of a negative stress optic coefficient, the metallic element brought by the oxide modifier always acts covalently.

Therefore Weyl's model cannot fully explain the origin of a negative stress optic coefficient. In his theory, he postulated that strong deformation of polarizable cations can exceed the effect of the anions and the stress optic coefficient becomes negative. On Figure 9.1, the deformation of the oxygens is perpendicular to the tensile stress because, in general, anions are more polarizable than cations. In the case of the lead oxide, the polarizability of Pb^{2+} is greater than the polarizability of O^{2-} (see Table 9.2). Therefore the deformation of the Pb^{2+} should now be the one perpendicular to

the tensile stress and the oxygens should be deformed in the direction of the stress. According to this model, under a tensile stress, the ordinary electron density is always greater than the extraordinary electron density. If the anion and cation show the same polarizability, then the deformations in both directions balance each other and produce a zero-stress optic coefficient. Therefore, in the case of ionic compounds the introduction of highly polarizable cations can reduce the stress optic coefficient but will never give a negative value.

In the case of covalent bond, Mueller's model of bond deformation shown in Figure 3.6 is actually more suitable. Ions tend to maximize the interaction with the surrounding charged particles giving rise to a high coordination, whereas covalent bonds are based on electron exchange and are directional interactions. The elastic deformation of covalent crystals is a complex problem. Physics models developed to date can only solve the deformation of specific compounds, such as the Keating model suitable for crystals made only of elements of the IVa group [263]. A more qualitative approach is presented here based on Mueller's model. Under the application of a tensile stress, two phenomenon are likely to occur in the structure: variation of the bond length and variation of the bond angle as shown in Figure 9.4. In both cases, the atoms are displaced in the structure corresponding to the lattice

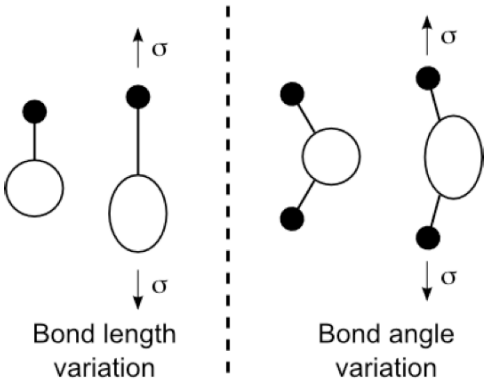

Figure 9.4: Structural variation of covalent bonds: bond length variation and bond angle variation

effect defined by Mueller. The shape of the atom is also modified which corresponds to the atomic effect. The bond variation tends to move the atoms farther apart in the direction of the stress, but the interatomic distance decreases in the ordinary direction. If only this effect is taken into consideration, the density of electron decreases in the direction of the stress and increases in the direction perpendicular to the stress. Based on the Drude-Voigt formula (Equation 9.5), the birefringence Δn becomes negative under the action of a negative stress (tensile stress). In this case the stress optic coefficient is positive. A covalent bond is made of an exchange of electrons between the two atoms, it can be considered that the atoms would also be elongated in the direction of the stress, the amplitude of the deformation depending on the polarizability of the element. This deformation corresponds to the atomic effect.

The bond angle variation would mostly affect the shape of the atoms as illustrated in Figure 9.4. The electronic cloud is elongated in the direction of the strain, making the number of electrons per unit volume greater in the extraordinary direction than in the ordinary direction. The birefringence Δn becomes positive under a tensile stress ($\sigma < 0$), therefore the stress optic coefficient is negative. From this point of view, the displacement of the atoms in the structure (i.e. lattice effect) contributes to a positive stress optic coefficient, whereas the deformation of the atoms (atomic effect) contributes to a negative stress optic coefficient, conversely to Mueller's conclusions. The Poisson's ratios of some binary lead glasses are given in Table 9.3. According to these values, the deformation in the the ordinary directions is three to four times smaller than the deformation in the extraordinary direction. Therefore, the variation of the extraordinary refractive index is of greater influence on the birefringence than the variation of the ordinary refractive index.

Similar to the ionic deformation, the polarizability of the elements plays an important role in the photoelastic response of covalent compound. According to this model of deformation, the stress optic coefficient should decrease with the addition of highly polarizable cations which corresponds to the experimental results. The

$(PbO)_x$-$(SiO_2)_{1-x}$		$(PbO)_x$-$(B_2O_3)_{1-x}$		$(PbO)_x$-$(P_2O_5)_{1-x}$	
x	ν [264]	x	ν [265]	x	ν [266]
33	0.230	25	0.268	29.3	0.300
40	0.237	35	0.275	34.1	0.300
50	0.259	45	0.276	42.0	0.300
58	0.265	55	0.283	50.5	0.300
67	0.276	65	0.285	54.6	0.300
70	0.286	70	0.287	58.8	0.300

Table 9.3: Poisson's ratio of binary lead glasses

polarizability dependence of the photoelastic response in the case of ionic and covalent bonds also explains the good agreement of the values of the ξ ratio with the experimental observations for the different oxides.

More can be told about the correlation of the polarizability of the oxide and the photoelasticity of a glass. In his article, Mueller mentioned the difference between the natural and induced deformations of the atoms in the structure. The natural deformation is the geometry of an atom's site in the unstressed material, whereas the induced deformation is the variation of the environment due to the application of a stress. The natural deformation seems to have a significant importance in the photoelastic response of a glass, as observed in the cases of the lead borate and the tin phosphate systems. In the lead borate glass, the evolution of the ^{207}Pb static NMR (Figure 5.4) shows an increase of the chemical shift anisotropy when the stress optic coefficient decreases. For a negative stress optic coefficient, the symmetry of the lead environment is lower than for a positive stress optic coefficient, in good agreement with a covalent behavior. In the tin phosphate glass, the quadrupole splitting for the tin atoms is greater for a negative stress-optic glass than for a positive stress-optic glass (Table 6.1), which also reveals a lower symmetry. Based on this two studies, it seems that the metallic element brought by the oxide modifier should have a great natural deformation to be able to give rise to a negative stress optic coefficient.

9.2 Classification of the oxides

The amorphous nature of glass makes it difficult to establish a standard pattern of glass structure similar, for example, to the Bravais lattice in crystal. According to Zachariasen's random network theory and Lebedev's crystallite hypothesis, the glass structure can be derived from the crystalline structure of the oxide entering into the compostition. Depending on the ionic or covalent nature of the bond, Weyl's model or Mueller's model of deformation should be adopted. But no bond is 100% ionic or 100% covalent, therefore the structural variation of the solid would partially follow both models in function of the degree of ionicity. Barr investigated the O 1s binding energy of simple oxides M_xO_y, and evaluated the degree of ionicity of the $M-O$ bonds based on his results [267]. The binding energy of the different oxides varies from 528.0 eV to 533.5 eV which allowed him to classify the oxides into three categories:

1. Semicovalent oxides: oxides with a O 1s binding energy in the range 530.5 - 533.5 eV. They include most of the glass formers (SiO_2, B_2O_3, P_2O_5, GeO_2).
2. Normal ionic oxides: oxides with a O 1s energy at 530 ± 0.4 eV, their ionicity is estimated between 76% and 89%. Most transition metals belong to this category. More surprisingly Na_2O also belongs here, whereas one would expect it to belong in the third category.
3. Very ionic oxides: oxides with a low binding energy in the range 529.5 - 528.0 eV, their ionicity is greater than 90%. It includes oxides such as SrO, Cs_2O, CdO and BaO.

According to Barr's study, PbO has an O 1s binding energy at 529.7 eV, which classifies it as a very ionic oxide. PbO has a litharge structure with the lead on top of a square based pyramid. A low coordination number and directional bonds are more characteristic of a covalent behavior than an ionic behavior [268].

From a polarizability approach, Dimitrov and Sakka established a similar classification of simple oxides [258]:

1. Oxides with a low polarizability between 1 and 2 Å^3. The glass formers with the highest stress optic coefficient belong to this category (SiO_2, B_2O_3, P_2O_5, GeO_2).
2. Oxides with a polarizability in the range 2-3 Å^3. Most transition metallic oxides belong to this category.
3. Oxides with a high polarizability greater than 3 Å^3. The oxides contributing to strongly decreasing the stress optic coefficient belong to this category, such as PbO, BaO, SnO, Bi_2O_3 and Sb_2O_3.

Dimitrov and Sakka found a good correlation between the polarizability and the O 1s binding energy of simple oxides with two similar classifications based on different properties. In a general trend these classifications also give a good idea of the contribution of the oxides to the stress optic coefficient. The first category (low polarizability, high O 1s binding energy) includes most of the glass formers with a high and positive stress optic coefficient. The third category (high polarizability, low O 1s binding energy) includes all of the oxides known to strongly decrease the stress optic coefficient. The definitions given by Barr about the three categories could be contested, particularly the third category considered as *"very ionic oxides"*. From Dimitrov and Sakka's work, lead oxide PbO, antimony(III) trioxide Sb_2O_3, tin oxide SnO and bismuth(III) trioxide Bi_2O_3 should all belong to the last category but their crystalline structure are more relevant of covalent compounds [135,227,228,262,268,269].

The second category mainly regroups the transition metals. Almost no data can be found in the literature about the influence of transition metals on the photoelastic response of glass. Only very few compositions of zinc borate and zinc phosphate glasses were prepared by Matusita *et al.*. Also binary zinc-borate/phosphate and binary cadmium-borate/phosphate systems were briefly investigated for this thesis. Surprisingly, none of these glasses follow the trend given by the empirical model in spite of the absence of bond length and coordination variation. Especially in the case of the zinc phosphate glass where the d/N_c ratio of both cations remains constant at all compositions. Even more surprising, an amount of about 50 mol-% of ZnO

into a borate glass gives a relatively low stress optic coefficient of 1.03±0.2 Brewsters whereas this coefficient is 11 Brewsters in a pure B_2O_3 glass. The addition of more ZnO results in an increase of the stress optic coefficient. No model so far can explain this evolution, and more investigation of this glass system, and of transition metal binary system in general, should be performed.

9.3 The empirical model

In the empirical model established by Zwanziger *et al.* the d/N_c ratio provides useful information about the contribution of the oxide on the photoelastic response of glass. From the data and the discussion presented previously, it is possible to gain understanding of why this model can predict the photoelastic response of a glass based on structural data. From the experiment, it was observed that elements acting ionically never give a negative stress optic coefficient. The reason for this is explained in section 9.1. Ionic interactions are usually characterized by a high coordination number resulting in a low d/N_c ratio. Conversely, covalent interactions are a directional exchange of electrons, they give rise to a lower coordination number and thus a higher d/N_c ratio. Therefore, the coordination gives an indirect indication of the degree of ionicity of the cation-oxygen interaction. A low d/N_c ratio corresponds to an ionic compound that can only contribute to a positive stress optic coefficient, whereas a high d/N_c ratio corresponds to a covalent compound that can give a positive or negative stress optic coefficient. In this last case, the cation-oxygen bond length brings the additional information required to achieve a good prediction. As mentioned previously, the O 1s binding energy of an oxide can be used to classify the simple oxides into three categories. It was observed that oxides with a high O 1s binding energy have a low polarization and contribute to a positive stress optic coefficient whereas oxides with a low O 1s binding energy have a high polarizability and contribute to a negative stress optic coefficient. Intuitively, it seems that the binding energy is related to the bond length: a low binding energy indicating a weak

interaction and therefore a long bond length. This assumption has been verified and the cation-oxygen bond length is related to the binding energy as shown in Table 9.4. Therefore the cation-oxygen bond length can also be related to the oxide's con-

	Bond length (Å)	References	O 1s Binding energy (eV) [267]
B_2O_3	1.37	[75]	533.2
P_2O_5	1.50	[86–88]	533.5
SiO_2	1.61	[68, 69]	532.8
GeO_2	1.72	[270]	531.3
ZnO	2.00	[246]	530.3
SnO_2	2.06	[106]	530.1
MgO	2.11	[20]	530.9
BaO	2.74	[28]	528.2
PbO	2.33	[135]	529.7

Table 9.4: Cation-oxygen bond length and O 1s binding energy of simple oxides. The bond length increases as the binding energy decreases.

tribution to the photoelastic response of a glass: a long bond length being in favor of a low stress-optic coefficient and vice versa. A long bond length increases the d/N_c ratio like a low coordination number.

The boron trioxide is the oxide with the highest stress optic coefficient, and the lead oxide is the oxide modifier with the strongest contribution to decreasing the stress optic coefficient. These are the two oxides with the strongest positive and negative contribution respectively and, according to Table 9.4, the difference in their bond length is less than 1 Å whereas the coordination number can vary from 6 (CdO) to 2 (HgO) [106]. Therefore the coordination number can be considered as the main parameter influencing the prediction by separating ionic and covalent compounds. Then the bond length adjusts the prediction. This principle is illustrated in Figure 9.5. This is a general rule with some exceptions, such as B_2O_3 which has a low cation coordination number of 3. It could be expected that the oxide would contribute to decreasing the stress optic coefficient, but the $B-O$ bond length is short enough to counter-balance the effect of the coordination so that the final contribution is to a

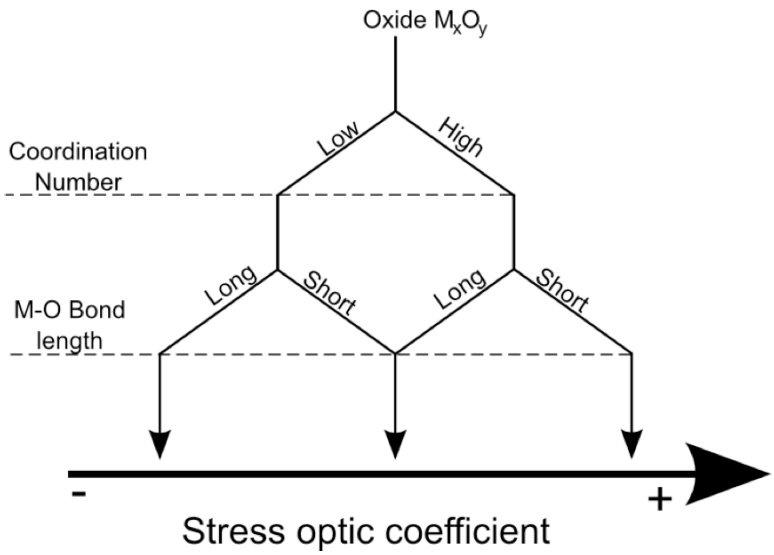

Figure 9.5: Contribution of the coordination number and cation-oxygen bond length in the Zwanziger's emprical model

very positive stress optic coefficient.

9.4 Strategy to design zero-stress optic glass

In function of its application, a glass needs to have a combination of properties. The zero-stress optic property is only one property among many others such as transparency, absence of color, or high chemical durability. Obtaining a glass with all the required properties is related to the combination of elements present in the glass, which makes all glasses unique in terms of composition and structure. Each glass requires unique experimental conditions to be prepared which affects the strategy adopted. From the experience and observation of preparing zero-stress optic glasses, a few general rules can be given to design new glasses with specific properties:

- All glass formers have a positive stress optic coefficient, therefore the first step is to find the oxide modifier suitable for the application that can decrease sufficiently the stress optic coefficient.

- Before looking for a zero-stress optic coefficient, attempts should be made to obtain a negative stress optic coefficient by introducing a large amount of oxide modifier. If such a glass can be prepared, it means that the glass system went from a positive to a negative stress optic coefficient, therefore at least one zero-stress optic composition exists for this system. The values obtained for the different compositions should give indications about the zero-stress optic compositions.
- In a binary system, only one zero-stress optic composition can be found. Such a system has one degree of freedom in terms of composition because the concentration of both oxides are related to each other. In a ternary system the degree of freedom becomes two and a range of zero-stress optic compositions could be found. These compositions follow a line in the ternary diagram of the glass, therefore it offers more possibilities to combine different properties by adjusting the glass composition. The degree of freedom to adjust the glass composition can be defined as the number of oxide constituent of the glass minus one.

According to the empirical model, the photoelastic response is an additive property which depends only on the oxides added to the glass composition. This statement is a simplification of the nature of the phenomenon but remains a good starting point. One of the objectives of this thesis was to design a glass that is able to replace the SF57 glass, therefore the new material should have: a zero-stress optic property, a high transparency, no color, a high index of refraction, a low dispersion and a high chemical durability. The tin borophosphate glasses prepared for this thesis contain all these properties, but their index of refraction remains slightly lower than the SF57 glass. Also, the tin-containing glasses have to be prepared under O_2-free atmosphere, which can be inconvenient and expensive in terms of production costs. Among the elements known to reduce the stress optic coefficient, lead needs to be substituted, thallium is highly toxic, tin(II) and antimony(III) are oxidized at high temperature and bismuth gives a dark color to the glass. None of the metallic oxides can fulfill

all the requirements for a low cost zero-stress optic glass. Each glass system requires specific conditions to be prepared and to give specific properties. To illustrate the strategy to design a new zero-stress optic glass, an example is given below. Before beginning, the desired properties have to be defined and ordered by importance:

1. Zero-stress optic
2. Preparation in air
3. Transparent and colorless
4. High index of refraction
5. High chemical durability

The barium tellurium glass system gives a zero-stress optic glass at 17 mol-% BaO [107]. As mentioned before, according to the empirical model the addition of barium into a TeO_2 glass should not decrease the stress optic coefficient whereas the polarizability model (e^{ξ} value) predicts that the stress-optic coefficient should decrease. Therefore, the polarizability model gives a better prediction and was used in this example to estimate the influence of each oxide. A high amount of tellurium brings a yellow color to the glass, therefore another glass former has to be used in addition of TeO_2 to minimize the coloration. The TeO_2 - SiO_2, TeO_2 - B_2O_3 and TeO_2 - P_2O_5 systems all present the phenomenon of immiscibility, giving rise to inhomogeneous glass or partial crystallization [271].

It was discussed earlier in this work that borophosphate glasses have a different structure than borate and phosphate glasses giving rise to good chemical durability due to the connexion of phosphate chains by boron tetrahedra. Because of these structural differences, attempts were made to work with telluride borophosphate glass. Also the tin borophosphate glasses presented in section 6.3 were transparent and colorless, therefore it can be expected that the addition of boron and phosphorus would decrease the yellow color of TeO_2. The low stress optic coefficient of barium-containing glasses can be combined with a borophosphate glass to obtain a transparent zero-stress optic glass. Initially, an attempt was made to prepare a

barium borophosphate glass but resulted in a gray and poorly transparent glass. To choose the composition of glass to prepare in the $(BaO)_x$ - $(TeO_2)_y$ - $(B_2O_3)_z$ - $(P_2O_5)_{1-x-y-z}$ system, the advantages and disadvantages of each oxide should be analyzed:

- BaO: decreases the stress optic coefficient but acts ionically and can bring a gray color. A high amount might result in coloring and crystallizing the glass.
- TeO_2: glass former with a low stress optic coefficient (0.64 Brewsters), it participates in lowering the stress optic coefficient and to the glass network. It brings a yellow color.
- B_2O_3: glass former with a very high stress optic coefficient (11 brewsters). Gives a transparent glass and good durability when it is combined with P_2O_5.
- P_2O_5: glass former with a positive stress optic coefficient. The actual stress optic coefficient cannot be determined with the Sénarmont method, but its e^{ξ} value is equal to 1.006 which is very close to the value for B_2O_3 (1.002). Its stress optic coefficient can be expected to also be very high. It gives a transparent glass and provides good durability when it is combined with B_2O_3.

Taking these features into account, many compositions were prepared and the lowest stress optic coefficient obtained was 0.2 Brewsters for the composition 46.5 BaO - 32.5 TeO_2 - 7.88 B_2O_3 - 13.13 P_2O_5. This glass is almost transparent with a very slight yellow/green color and an refractive index of 1.74.

Multicomponent glasses offer different degrees of freedom to adjust their compositions according to the required properties. In this case, the addition of BaO gives rise to a devitrification, unfortunately this oxide is the only one capable of decreasing the stress optic coefficient to negative values. The addition of TeO_2 could help to decrease the stress optic coefficient but it also increases the yellow/green color. One solution for future work on this glass would be the total or partial substitution of TeO_2 by Sb_2O_3. The antimony(III) oxide can be partially oxidized into antimony(V) oxide,

but the preparation of antimony phosphate and antimony borophosphate glasses demonstrated that Sb-containing glasses can be transparent with a low or negative stress optic coefficient. The work presented in this thesis focused on oxide glass, therefore the decrease of the stress optic coefficient was obtained to introduce highly polarizable cations in the composition. In a more general way, on top of adding highly polarizable cations, the introduction of poorly polarizable anions would also help to obtain zero-stress optic glasses. The introduction of fluorine in the glass would substitute part of the oxygen. The polarizability of F^- anions is lower than the polarizability of O^{2-}, therefore the stress optic coefficient would decrease because of a lower overall anionic polarizability as shown in Table 9.5. The introduction of fluorine in oxide glass has already been performed to decrease the stress optic coefficient [272]. Matusita *et al.* also measured the stress optic coefficient of some

Oxide MO	α_M^{2+} (Å^3)	α_O^{2-} (Å^3)	e^{ξ}	Fluoride MF_2	α_M^{2+} (Å^3)	α_F^{-} (Å^3)	e^{ξ}
MgO [259]	0.094	1.687	1.057	MgF_2 [274]	0.150	0.883	1.087
CaO [259]	0.469	2.420	1.214	CaF_2 [275]	0.544	1.164	1.263
PbO [259]	3.623	3.381	2.623	PbF_2 [276]	3.040	1.323	3.154

Table 9.5: Polarizability ratio of oxides and fluorides

ternary fluoride glasses and found out that these glasses have a very small stress optic coefficient always very close to zero [273].

Chapter 10

Conclusion and Future Studies

The recent works of Zwanziger *et al.* opened new possibilities of zero-stress optic glass compositions by demonstrating the contribution of some oxides (SnO, Sb_2O_3, BaO) to reduce significantly the stress-optic coefficient [106, 107]. Lead-, tin- and antimony-containing glasses were studied in binary silicate, borate and phosphate glasses to investigate the structural origin of the photoelastic response of these materials. The evolution of the structure of lead borate glasses was correlated to the variation of the stress optic coefficient over the range of compositions and this study revealed the poor reliability of Mueller's theory for this particular case. The lead is acting mainly ionically for a positive stress-optic coefficient whereas it is acting more covalently for a negative stress optic coefficient. From the literature, it appears that lead behaves similarly in binary phosphate and silicate glasses. The investigation of tin's behavior in phosphate glasses leads to a similar conclusion: the tin atoms are acting mostly covalently at low and high content whereas the stress-optic coefficient evolves from positive to negative values. Mueller's theory indicates that the tin should act mostly covalently for a positive stress-optic coefficient and ionically for a negative stress-optic coefficient. Tin's behavior remains also covalent in the

case of the tin silicate glass (see section 5.2.1). Experiments and literature about the antimony-containing glasses demonstrated that antimony(III) trioxide can provide zero-stress optic properties to a glass [106]. However, the high hygroscopic nature of antimony-phosphate glasses prevented any relevant structural and compositional analysis. Furthermore the investigation of antimony's environment was attempted with the help of ^{121}Sb Mössbauer spectroscopy with no success. Only the ^{11}B NMR spectroscopy gave indications about antimony's covalent nature over the range of compositions in the binary borate glass system. According to these data it appears that Mueller's theory of photoelasticity cannot explain the correlation between the glass structure and its photoelastic response. Therefore, this theory should not be used to determine structural parameters based on the photoelasticity of a material.

Conversely, the structural investigation of several glasses greatly improved the results provided by the Zwanziger's empirical model. Initially this model uses crystalline data of the oxides constituent of the glass to predict its photoelastic response in function of the composition. This model can predict the zero-stress optic composition of a binary glass with an error of about 15%, however in the case of the lead borate and tin phosphate glass systems this error is 33% and 23% respectively. The introduction of the coordination and bond length variations for the cations in the glass through the different compositions greatly reduces these errors to $\sim$2% in both cases. This model, which was initially established to design new zero-stress optic glasses, can also provide useful information about the glass structure and its impact on the photoelasticity of the material.

The ability of the Zwanziger's model to predict the photoelastic response is based on the ratio of the cation-oxygen bond length and the cation's coordination. A high coordination and short bond length are both directly and indirectly related to an ionic behavior whereas a low coordination and long bond length are related to a covalent interaction. From Weyl's and Mueller's model it was established that an ionic

behavior cannot give rise to a negative stress-optic coefficient whereas a covalent behavior can give rise to a positive or negative stress-optic coefficient. The oxide's ability to decrease the stress optic coefficient depends on the polarizability of both the cation and the oxygen. The efficiency of the oxide can be determined by the value e^{ξ} with ξ the ratio of the cation's polarizability by the oxygen's polarizability according to Equation 9.6. Similarly to the d/N_c ratio, the e^{ξ} value provides indications about the oxide's contribution on the stress optic coefficient: a low value is characteristic of an oxide contributing to a positive stress optic coefficient and a high value is characteristic of an oxide contributing to a negative stress optic coefficient. The ξ ratio seems to provide better evaluation of the effect of the oxides than the empirical model, but it does not bring any real improvement on the prediction of zero-stress optic glass compositions.

The correlation between polarizability and photoelasticity fits most of the cases, but the measurements of the stress-optic coefficient in zinc and cadmium binary phosphate and borate glasses does not obey any model in existence. All glasses follow the reverse trend predicted for them: the stress-optic coefficient increases when the Zwanziger's model and the ξ ratio suggest that it should decrease and vice versa. The brief structural investigation of these four glass systems did not provide any additional information to explain this behavior. Not much work has been done so far about the influence of the transition metals on the photoelastic response of glass and more investigations are required to verify if this behavior is common to all transition metals or only a characteristic of the elements of group II B (and thus related to the electronic structure).

Another part of the work was dedicated to the investigation of new zero-stress optic glasses combining high transparency, high refractive index, no coloration and a good chemical durability. A series of tin borophosphate glasses with this combination of properties was successfully achieved. Three series of glasses were prepared

with fixed $x_{B_2O_3}/x_{P_2O_5}$ ratio equal to 0.2, 0.4 and 0.6. The first two series gave a zero-stress optic glass and the 0.6 series was close but could not be achieved due to technical difficulties. These zero-stress optic glasses are perfectly transparent and colorless with a refractive index of about 1.74. According to Lim *et al.* [195], glasses with a higher $x_{B_2O_3}/x_{P_2O_5}$ ratio can be prepared, and they would give a refractive index up to 1.84, which is the refractive index of the Schott SF57 glass. The same work on the antimony borophosphate glasses was not as successful but all the experience acquired on all these projects gave rise to a global strategy to design new zero-stress optic glass. A series of barium telluride borophosphate glasses were prepared with the objective of obtaining another transparent and colorless zero-stress optic glass. The best result obtained so far is a glass with a stress optic coefficient of 0.2 Brewsters, a very light yellow/green color and a refractive index of 1.74. More work is required to eliminate the slight coloration, and to decrease slightly the stress optic coefficient. The main advantage of this glass is its preparation in air, conversely to the tin borophosphate that require an O_2-free atmosphere to be synthesized.

According to the ξ ratio, the stress optic coefficient can be decreased by increasing the cationic polarizability but also by decreasing the anionic polarizability. A partial substitution of the oxygen by fluorine should help to obtain new lead-free glasses with a low stress optic coefficient. This method should be tested on the barium telluride borophosphate at 0.2 Brewsters to finally obtain a zero-stress optic glass. For this system, a partial or total substitution of TeO_2 with Sb_2O_3 should also be tested. From the synthesis of the antimony borophosphate it was observed that the glasses prepared in air were very slightly yellow, but their color was not as bright as the color brought by TeO_2. The partial oxidation of Sb(III) to Sb(V) would also probably affect the stress optic coefficient.

Future projects should also focus on the transition metal elements in glass and their effect on the photoelastic response. In the present work, a close correlation was

established between the oxide's polarizability and the photoelastic response. However, this correlation is not verified in the case of the zinc and cadmium oxides, therefore, more work is required to investigate if this behavior is common to all transition metal elements or only to the elements of group II B. The synthesis of binary iron-containing glass would be ideal to investigate the structural dependence of the photoelastic response especially in silicate, borate and phosphate glasses. The local environment of the glass formers can be analyzed by NMR spectroscopy whereas the iron can be easily studied by ^{57}Fe Mössbauer spectroscopy. Also, one of the most interesting studies would be to investigate the evolution of the local deformation of the iron or tin atom under stress. The Mössbauer analysis of a thin film of tin- or iron-containing glass under a tensile stress could provide valuable information on the influence of the deformation (i.e. polarizability) of the atoms on the photoelastic response. Mössbauer experiments under tensile stress have already been performed for the study of several iron alloys [277–279]. However, the resistance and possible brittleness of the film might limit the possibilities of such experiment.

A brief study of the antimony borate glass was presented in section 7.2. The results obtained for the zero-stress optic coefficient were different than the value by Zwanziger *et al.*. The partial oxidation of Sb_2O_3 might be involved in this inconsistency of the results and a complete study involving ^{121}Sb Mössbauer spectroscopy and an accurate glass analysis is required for this glass system.

All the work presented in this thesis focused on obtaining a new lead-free zero-stress optic glass, but observations and conclusions resulting from the various experiments can also be used to design glasses with high birefringence. The recent work of Zhang *et al.* on the "invisibility cloak" for visible light using the birefringence properties of the calcite might increase the interest for this phenomenon [280, 281] in the next few years. The calcite has a fixed birefringence whereas a glass can have its birefringence modulated by the application of a pressure giving access to a better

control of the phenomenon and opening new possibilities. A glass with a high stress optic coefficient would give rise to a higher amplitude of birefringence. Also, from our knowledge so far, it can be estimated that the oxide glass with the lowest stress optic coefficient would belong to the system $(Sb_2O_3)_x$-$(PbO)_{1-x}$ with a high amount of lead (and yellow color), but the substituion of PbO with PbF_2 would give rise to an even lower coefficient.

The photoelasticity of glass remains one of the least known fields of investigation. The present thesis brings new elements about the structural origin of the photoelastic response of glass and opens new possibilities for the synthesis of glasses with future potential applications. Hopefully this work will contribute to the development of new environmentally friendly materials and allows the development of new technologies.

References

[1] M.W. Woolfson; *"Materials, Matter and Particles: A Brief History"*, Imperial College Press, London, 2010.

[2] E.A. Carter, M.A. Pasek, T. Smith, T.P. Kee, P.Hines, H.G.M. Edwards; *Anal. Bioanal. Chem.*, 2010, 397, 2647.

[3] K.J. Rao; *"Structural Chemistry of Glasses"*, Elsevier, 2002.

[4] H.E. Harper Jr., A.H. Knoll; *Geology*, 1974, 3, 175.

[5] W.E.G. Müller, X. Wang, Z. Burghard, J. Bill, A. Krasko, A. Boreiko, U. Schlossmacher, H.C. Schröder, M. Wiens; *J. Struct. Biol.*, 2009, 168, 548.

[6] Pliny the Elder; *"Naturalis Historia"*; Editions and translations: English. J. Bostock, M.D., F.R.S. H.T. Riley, Esq., B.A. London. Taylor and Francis, Red Lion Court, Fleet Street.1855.

[7] A. Macfarlane, G. Martin; *"Glass: A World History"*, The University of Chicago Press, Chicago, 2002.

[8] C.T. Gable, *"Murano Magic: Complete Guide to Venetian Glass, Its History and Artists"*, Schiffer books, 2007.

[9] C. MacLeod; *Tech. & Cult.*, 1987, 28, 4, 776.

[10] W. Klement, R.H. Willens, P.O.L. Duwez; *Nature*, 1960, 187, 869.

[11] J. Schroers, T.M. Hodges, G. Kumar, H. Raman, A.J. Barnes, Q. Pham, T.A. Waniuk; *Mater. Today*, 2011, 14, 1-2, 14.

[12] Ma. Poulain, Mi. Poulain, J. Lucas; *Materials Research Bulletin*, 1975, 10, 243.

[13] E. Le Bourhis; *"Glass: Mechanics and Technology"*, Wiley-VCH, Weinheim, 2008.

[14] R.M.A. Azzam; *Thin Sol. Films*, 2011, 519, 2584.

[15] R. Cline, M. Duelli, M. Greenberg; *Displays*, 2002, 23, 151.

[16] F. Pockels; *Ann. Phys.*, 1902, 7, 745.

[17] W.J. Smith; *"Modern Optical Engineering: The Design of Optical Systems"*, Spie Press, 2008.

[18] T. McMillan, P. Taborek, J.E. Rutledge; *Rev. Sci. Instrum.*, 2004, 75, 11, 5005.

[19] www.rohs.eu

[20] M. Tashiro; *J. Soc. Glass Technol.*, 1957, 353T.

[21] A.I. Rabukhin, G.V. Belousova; *Glass Ceram.*, 1992, 49, 458.

[22] H.G. Jerrard; *J. Opt. Soc. Am.*, 1948, 38, 35.

[23] W.F. Riley, A.J. Durelli; *"Introduction to photomechanics"*, Prentice-Hall Inc., 1965.

[24] H. Mueller; *J. Gen. App. Phys.*, 1935, 6, 6, 179.

[25] H. Mueller; *Phys. Rev.*, 1935, 47, 947.

[26] H. Mueller; *J. Am. Ceram. Soc.*, 1938, 21, 27.

[27] K. Matusita, C. Ihara, T. Komatsu, R. Yokota; *J. Am. Ceram. Soc.*, 1984, 67, 10, 700.

[28] K. Matusita, R. Yokota, T. Kimijima, T. Komatsu, C. Ihara; *J. Am. Ceram. Soc.*, 1984, 67, 4, 261.

[29] K. Matusita, C. Ihara, T. Komatsu, R. Yokota; *J. Am. Ceram. Soc.*, 1985, 68, 7, 389.

[30] H. Scholze; *"Glass: Nature, Structure and Properties"*, Springer-Verlag, New York, 1991.

[31] M.A. White; *"Properties of Materials"*, Oxford University Press, New York, 1999.

[32] J. Barton, C. Guillemet; *"Le Verre: Science et Technologie"*, EDP Sciences, Paris, 2005.

[33] A. A. Lebedev; *Trans. State Optical Inst.*, 1921 ,2, No. I0

[34] A. A. Lebedev; *Rev. d'Optique Theor. et Instr.*, 1926, 5, 4.

[35] M.L. Frankenheim, *Die Lehre von der Cohäsion*, 1835, Breslau.

[36] A.I. Stozharov, S.V. Nemilov; *Trudy Gos. Opt. Inst.*, 1985, 58, 2, 148.

[37] M. Mosbah, J.P. Duraud, R. Clocchiatti; *Nucl. Instrum. Meth. Phys. Research*, 1997, B 130, 1, 171.

[38] E.A. Porai-Koshits; *J. Non-Cryst. Solids*, 1990, 123, 1.

[39] K.S. Evstropiev, E.A. Porai-Koshits; *J. Non-Cryst. Solids*, 1972, 11, 170.

[40] I.S Patel, P.W. Schmidt, S.M. Ohlberg; *J. Appl. Crystallogr.*, 1971, 43, 1636.

[41] J.H. Konnert, J. Karle; *Science*, 1973, 179, 177.

[42] A.J. Leadbetter, A.C. Wright; *J. Non-Cryst. Solids*, 1972, 7, 23.

[43] J.C. Phillips; *Phys. Today*, 1982, 35, 2, 1.

[44] D.L. Evans, N.F. Borreli, P.M. Teter; *Science*, 1973, 181, 174.

[45] E.A. Porai-Koshits; *Fiz. Khim. Stekla*, 1977, 3, 292.

[46] F.L. Galeener, A.C. Wright; *Solid State Commun.*, 1986, 57, 677.

[47] W.H. Zachariasen; *J. Am. Ceram. Soc.*, 1932, 54, 3841.

[48] H. Krutter, O. Morningstar, B.E. Warren; *J. Am. Ceram. Soc.*, 1936, 19, 202.

[49] B.E. Warren, J. Biscoe, *J. Am. Ceram. Soc.*, 1938, 21, 49.

[50] J. Biscoe, B.E. Warren, *J. Am. Ceram. Soc.*, 1938, 21, 259.

[51] J. Biscoe, B.E. Warren, *J. Am. Ceram. Soc.*, 1938, 21, 287.

[52] B.E. Warren, B.S. Robinson, J. Biscoe; *J. Am. Ceram. Soc.*, 1939, 22, 180.

[53] G. Hägg; *J. Chem. Phys.* , 1935, 3, 42.

[54] W.H. Zachariasen; *J. Chem. Phys.* , 1935, 3, 162.

[55] E.A. Porai-Koshits, V.I. Averjanov; *J. Non-Cryst. Solids*, 1968, 1, 1, 29.

[56] E.A. Porai-Koshits, U.V. Mazurin; *Phase Separation in Glass*, North Holland, 1984.

[57] R. Roy; *Inter. J. Appl. Glass Sc.*, 2010, 1, 1, 3.

[58] A.R. Varshneya; *"Fundamentals of Inorganic Glasses"*, Academic Press, San Diego, 1994.

[59] P.J. Bray, M. Leventhal, H.O. Hooper; *Phys. Chem. Glasses*, 1963, vol. 4, No. 2, 47.

[60] F. Fayon, C. Bessada, A. Douy, D. Massiot; *J. Mag. Resonn.*, 1999, 137, 116.

[61] F. Fayon, C. Bessada, J.P. Coutures, D. Massiot; *Inorg. Chem.*, 1999, 38, 5212.

[62] K.H. Sun; *J. Am. Ceram. Soc.*, 1947, 30, 277.

[63] A. Dietzel; *Z. Electrochem.*, 1942, 48, 9.

[64] S.J. Stevens, R.J. Hands, J.H. Sharp; *J. Mat. Sc.*, 1997, 32, 2929.

[65] M.L. Huggins; *Phys. Rev.*, 1922, 19, 363.

[66] L.W. McKeehan; *Phys. Rev.*, 1923, 21, 503.

[67] T. Uchino; *J. Ceram. Soc. Jap.*, 2005, 113, 1,17.

[68] A.C. Wright; *J. Non-Cryst. Solids*, 1994, 179, 84.

[69] H.F. Poulsen, J. Neuefeind, H.B. Neumann, J.R. Schneider, M.D. Zeidler; *J. Non-Cryst. Solids*, 1995, 188, 63.

[70] F.L. Galeener; *J. Non-Cryst. Solids*, 1982, 49,1-3, 53.

[71] A. Pasquarello, R. Car; *Phys. Rev. Lett.*, 1998, 80, 5145.

[72] S.V. Berger; *Acta Cryst.*, 1952, 5, 389.

[73] S.V. Berger; *Acta Chem. Scand.*, 1953, 7, 611.

[74] S.L. Strong, R. Kaplow; *Acta Cryst.*; 1968, B24, 1032.

[75] G.E. Gurr, P.W. Montgomery, C.D. Knutson, B.T. Gorres; *Acta Cryst.*, 1970, B26, 906.

[76] H. Effenberger, C.L. Lengauer, E. Partthé; *Monat. Chem.*, 2001, 1515.

[77] A.H. Silver, P.J. Bray; *J. Chem. Phys.*, 1958, 29, 984.

[78] R.L. Mozzi, B.E. Warren; *J. Appl. Crystallogr.*, 1970, 251.

[79] C. Joo, U. Werner-Zwanziger, J.W. Zwanziger; *J. Non-Cryst. Solids*, 2000, 261, 282.

[80] M. Micoulaut, R. Kerner, D.M. Dos Santos-Loff; *J. Phys. Condens. Matter.*, 1995, 7, 8035.

[81] G.E. Jellison, L.W. Panek, P.J. Bray, G.B Rouse; *J. Chem. Phys.*, 1977, 66, 802.

[82] A.C. Hannon, R.N. Sinclair, A.C. Wright; *Physica*, 1993, A201, 375.

[83] R.A. Barrio, R. Kerner, M. Micoulaut, G.G. Naumis; *J. Phys. Condens. Matter.*, 1997, 9, 9219.

[84] A.R. Cooper; *J. Non-Cryst. Solids*, 1982, 49, 1.

[85] K. Trachenko, V.V. Brazhkin, G. Ferlat, M.T. Dove, E. Artacho; *Phys. Rev.*, 2008, B78, 172102.

[86] M. Jansen, B. Luër; *Z. Kristallogr.*, 1986, 177, 149.

[87] E.H. Arbid, B. Elouadi, J.P. Chaminade, J. Darriet; *J. Sol. State Chem.*, 1996, 127, 350.

[88] D. Stachel, I. Svoboda, H. Fuess; *Acta Crystallogr.*, 1995, C51, 1049.

[89] B.D. Sharma; *Inorg. Chem.*, 1987, 26, 454.

[90] D.W.J. Cruickshank, *Acta Cryst.*, 1964, 17, 679.

[91] F.L. Galeener, J.C. Mikkelsen; *Solid State Commun.*, 1979, 30, 505.

[92] J.J. Hudgens, S.W. Martin; *J. Am. Ceram. Soc.*, 1993, 76, 1691.

[93] R.K. Brow, D.R. Tallant, J.J. Hudgens, S.W. Martin, A.D. Irwin; *J. Non-Cryst. Solids*, 1994, 177, 221.

[94] K. Meyer, H. Hobert, A. Barz, D. Stachel; *Vibr. Spectrosc.*, 1994, 6, 323.

[95] K. Meyer, A. Barz, D. Stachel; *J. Non-Cryst. Solids*, 1995, 191, 71.

[96] U. Hoppe, G. Walter, A. Barz, D. Stachel, A.C. Hannon; *J. Phys. Condens. Matter*, 1998, 10, 261.

[97] U. Hoppe, G. Walter, R. Kranold, D. Stachel, A. Barz; *J. Non-Cryst. Solids*, 1995, 28, 192.

[98] R.E. Newnham; *"Properties of Materials: Anisotropy, Symmetry, Structure"*, Oxford University Press, 2005.

[99] B. Pokroy, A.N. Fitch, F. Marin, M. Kapon, N. Adir, E Zolotoyabko; *J. Struct. Biol.*, 2006, 155, 96.

[100] W. Voigt; *Ann. Physik*, 1901, 6, 459.

[101] O. Wiener; *Ber. deut. des, Wiss.*, 1910, 62, 255.

[102] H. Ambronn; *Goettinger Nachrichten*, 1919, 299.

[103] K.R. Banerjee; *Ind. Jour. Phys.*, 1927, 2, 195.

[104] K.F. Herzfeld; *J. Opt. Soc. Amer.*, 1928, 17, 26.

[105] K.F. Herzfeld, R.H. Lee; *Phys. Rev.*, 1933, 44, 625.

[106] M. Guignard, L.Albrecht, J.W. Zwanziger; *Chem. Mater.*, 2007, 19, 286.

[107] M. Guignard, J.W. Zwanziger; *J. Non-Cryst. Solids*, 2007, 353, 1662.

[108] E. Kordes; *Physik. Chem.*, 1939, 43, 173.

[109] L. Rivaollen, A. Revcolevschi, J. Livage, R. Collongues; *J. Non-Cryst. Solids*, 1979, 21, 171.

[110] R.E. Youngman, S. Sen, L.K. Cornellius, A.J.G. Ellison; *Phys. Chem. Glasses*, 2007, 44(2), 69.

[111] H. Masuda, R. Kimura, N. Sakamoto, K. Morinaga; *J. Jpn. Inst. Metals*, 1999, 63, 284.

[112] J. Fukunaga, K. Segawa, R. Ota; *Chem. Expr.*, 1990, 5, 5.

[113] M.H. Levitt; *"Spin Dynamics, Basics of Nuclear Magnetic Resonance"*, Wiley, 2001.

[114] J.B. Lambert, E.P. Mazzola; *"Nuclear Magnetic Resonance Spectroscopy, An Introduction to Principles, Applications, and Experimental Methods"*, Pearson Prentice Hall, 2004.

[115] R.K. Harris; *"Nuclear Magnetic Resonance Spectroscopy, A Physicochemical View"*, Longman Group UK Limited, 1986.

[116] M.J. Duer; *"Solid-State NMR Spectroscopy Principles and Applications"*, Blackwell Science Ltd, 2002.

[117] R.L. Mössbauer; *Z. Physik*, 1958, 151, 124.

[118] D.P.E. Dickson, F.J. Berry; *"Mössbauer Spectroscopy"*, Cambridge University Press, 1986.

[119] T.C. Gibb; *"Principles of Mössbauer Spectroscopy"*, Chapman and Hall Ltd, London, 1976.

[120] N.N. Greenwood, T.C. Gibb; *"Mössbauer Spectroscopy"*, Chapman and Hall Ltd, London, 1971.

[121] V. Martin, B. Wood, U. Werner-Zwanziger, J.W. Zwanziger; *J. Non-Cryst. Solids*, 2011, 357, 10, 2120.

[122] W.L. Konijnendijk, H. Verweij; *J. Am. Ceram. Soc.*, 1976, 59, 459.

[123] B.N. Meera, A.K. Sood, N. Chandrabhas, J. Ramakrishna; *J. Non-Cryst. Solids*, 1990, 126, 3, 224.

[124] B.N. Meera, J. Ramakrishna; *J. Non-Cryst. Solids*, , 1993, 159, 1-2, 1.

[125] K. Witke, T. Hübert, P. Reich; *Phys. Chem. Glasses*, 1994, 35, 1, 28.

[126] F.Busholtz, P.J. Bray; *J. Non-Cryst. Solids*, 1983, 54, 1-2, 43.

[127] T. Takaishi, J. Jin, T. Uchino, T. Yoko; *J. Am. Ceram. Soc.*, 2000, 83, 10, 2543.

[128] R. H. Perry; *"Perry's Chemical Engineers Handbook: 6th edition"*, McGraw Hill, New York, 1984.

[129] P. A. Beckmann, C. Dybowski, *J. Magn. Res*, 2000, 146, 379.

[130] H. B. George, C. Vira, C. Stehle, J. Meyer, S. Evers, D. Hogan, S. Feller, M. Affatigato; *Phys. Chem. Glasses*, 1999, 40, 326.

[131] K.J.D. MacKenzie, M.E. Smith; *"Multinuclear Solid-State NMR of Inorganic materials"*, Pergamon Materials Series, 2002.

[132] Youngman R., Zwanziger J.W., *J. Non-Cryst. Solids*, 1994, 168, 293.

[133] T. Fukazawa, M. Korekawa, Y. Fujita; *J. Non-Cryst. Solids*, 1996, 203, 102.

[134] J.L. Shaw, U. Werner-Zwanziger, J.W. Zwanziger; *Phys. Chem. Glasses*, 2006, Part B, 47,4, 513.

[135] J. Leciejewicz; *Acta Cryst.*, 1961, 14, 1304.

[136] F. Fayon, I. Farnan, C. Bessada, J. Coutures, D. Massiot, J.P. Coutures; *J. Am. Chem. Soc.*, 1997, 119, 6837.

[137] F. Fayon, C. Bessada, D. Massiot, I. Farnan, J.P. Coutures; *J. Non-Cryst. Solids*, 1998, 232-234, 403.

[138] D.L. Corker, A.M. Glazer; *Acta Cryst.*, 1996, B52, 260.

[139] E.M Rabinovitch; *J. Mater. Sci.*, 1976, 11, 925.

[140] M. Leventhal, P.J. Bray; *Phys Chem. Glasses*, 1965, 6, 113.

[141] R. Dupree, N. Ford, D. Holland; *Phys. Chem. Glasses*, 1987, 28, 78.

[142] A.M. Zahra, C.Y. Zahra, B. Piriou; *J. Non-Cryst. Solids*, 1993, 155, 45.

[143] L. Liu; Z. Phys., 1993, B 90, 393.

[144] V.O. Kabanov, T.M. Podol'skaya, O.V. Yanush; *Glass Phys. Chem.*, 1996, 22, 19.

[145] A.L. Shakhmin, A.M. Tyutikov; *Fiz. Khim. Stekla*, 1989, 16, 833.

[146] P.W. Wang, L. Zhang; *J. Non-Cryst. Solids*, 1996, 194, 129.

[147] F. Fayon, C. Landron, K. Sakurai, C. Bessada, D. Massiot; J. Non-Cryst. Solids, 1999, 243, 39.

[148] T. Takaishi, M. Takahashi, J. Jin, T. Uchino, T. Yoko; *J. Am. Ceram. Soc.*, 2005, 88, 6, 1591.

[149] S. Feller, G. Lodden, A. Riley, T. Edwards, J. Croskrey, A. Schue, D. Liss, D. Stentz, S. Blair, M. Kelley, G. Smith, S. Singleton, M. Affatigato, D. Holland, M.E. Smith, E.I. Kamitsos, C.P.E. Varsamis, E. Ioannou; *J. Non-Cryst. Solids*, 2010, 356, 304.

[150] O.V. Mazurin, M.V. Streltsina, T.P. Shvaiko-Shvaikovskaya; *"Handbook of Glass Data"*, Elsevier, New York, part B, 1985.

[151] M. Guignard, U. Werner-Zwanziger, J.W. Zwanziger; *J. Non-Cryst Solids*, 2008, 354, 7.

[152] G. Le Saoût, P. Simon, F. Fayon, A. Blin, Y. Vaills; *J. Raman Spectr.*, 2002, 33, 740.

[153] G.N. Greaves, S.J. Gurman, L.F. Gladden, C.A. Spence, P. Cox, B.C. Sales, L.A. Boatner, R.N. Jenkins; *Philos. Mag.*, 1988, B58, 3, 271.

[154] A. Lai, A. Musinu, G. Piccaluga, S. Puligheddu; *Phys. Chem. Glasses*, 1997, 38, 173.

[155] V. Martin, U. Werner-Zwanziger, J. Zwanziger, R. Dunlap; *Int. J. App. Glass Sc.*, 2011, (In Press).

[156] R.K. Brow, D.R. Tallant, J.J. Hudgens, S.W. Martin, A. D. Irwin; *J. Non-Cryst. Solids*, 1994, 177, 221.

[157] J.J. Hudgens, S.W. Martin; *J. Am. Ceram. Soc.*, 1994, 76, 1691.

[158] U. Hoppe, G. Walter, D. Stachel, *Silikattechnik*, 1990, 41, 227.

[159] K. Lagarec, D.G. Rancourt; *"Recoil-Mössbauer Spectral Analysis Software for Windows, v. 1.0"*, Technical report, University of Ottawa 1998.

[160] D. Massiot, F. Fayon, M. Capron, I. King, S. Le Calvé, B. Alonso, J. O. Durand, B. Bujoli, Z. Gan, G. Hoatson; *Magn. Reson. Chem.*, 2002, 40, 70.

[161] X. Gonze, B. Amadon, P.M. Anglade, J.M. Beuken, F. Bottin, P. Boulanger, F. Bruneval, D. Caliste, R. Caracas, M. Cote, T. Deutsch, L. Genovese, P. Ghosez, M. Giantomassi, S. Goedecker, D. Hamann, P. Hermet, F. Jollet, G. Jomard, S. Leroux, M. Mancini, S. Mazevet, M. J. T. Oliveira, G. Onida, Y. Pouillon, T. Rangel, G.M. Rignanese, D. Sangalli, R. Shaltaf, M. Torrent, M. Verstraete, G. Zerah, and J. W. Zwanziger; *Comput. Phys. Commun.*, 2009, 180, 2582.

[162] M. Torrent, F. Jollet, F. Bottin, G. Zérah, X. Gonze; *Comp. Mater. Sci.*, 2008, 42, 337.

[163] P.E. Blöchl; *Phys. Rev.*, 1994, B50, 17953.

[164] J.W. Zwanziger; *J. Phys.: Condens. Matter*, 2009, 21, 195501.

[165] J.W. Zwanziger, M. Torrent; *Appl. Magn. Reson.*, 2008, 33, 4477.

[166] M. Profeta, F. Mauri, C.J. Pickard; *J. Am. Chem. Soc.*, 2003, 125, 541.

[167] P. Pyykkö; *Mol. Phys.*, 2008, 106, 1965.

[168] J.P. Perdew, K. Burke, M. Ernzerhof; *Phys. Rev. Lett.*, 1996, 77, 3865.

[169] Y. Yang, M.A. Xueming, Y. Dong, H.E. Yizhen; *Chinese Phys. Lett.*, 1992, 9, 5, 266.

[170] S. Begin-Colin, G. Le Caër, A. Mocellin, C.Jurenka, M. Zandona; *J. Solid State Chem.*, 1996, 127, 98.

[171] W.H. Baur, A.A. Khan; *Acta Cryst.*, 1958, 11, 488.

[172] G.S. Collins; T. Kachnowski; N. Benczer-Koller; *Phys. Review B*, 1979, 19, 3.

[173] V.V. Chernaya, A.S. Mitiaev, P.S. Chizhov, E.V. Dikarev, R.V. Shpanchenko, E.V. Antipov, M.V. Korolenko, P.B. Fabritchnyi; *Chem. Mater.*, 2005, 17, 284.

[174] M. Mathew, L.W. Schroeder, T.H. Jordan; *Acta Cryst.*, 1977, B 33, 1812.

[175] R.C. Mercader, E.J. Baran, A.R. Lopez-Garcia; *J. Radioanal. Nucl. Chem.*, 1984, 85, 1, 13.

[176] L.Q. Fan, J.H. Wu, Y.F. Huang; *Z. Anorg. Allg. Chem.*, 2008, 634, 534.

[177] F. Izumi; *J. Sol. St. Chem.*, 1981, 38, 381.

[178] E. Bekaert, L. Montagne, L. Delevoye, G. Palavit, B. Revel; *Comptes Rendus Chimie*, 2004, 7, 377.

[179] D. Holland, A.P. Howes, M.E. Smith, A.C. Hannon; *J. Phys.: Condens. Matter*, 2002, 14, 13609.

[180] J.F. Bent, A.C. Hannon, D. Holland, M.M.A. Karim; *J. Non-Cryst. Solids*, 1998, 232-234, 300.

[181] D. Holland, A.P. Rowes, R. Dupree, J.A. Johnson, C.E. Johnson; *J. Phys. Condens. Matter.*, 2003, 15, S2457.

[182] K.F.E. Williams, C.E. Johnson, J.A. Johnson, D. Holland and M.M.A. Karim; *J. Phys.: Condens. Matter*, 1995, 7, 9485.

[183] J. Pannetier, G. Denes; *Acta Cryst.*, 1980, B36, 11, 2763.

[184] A. Hayashi, M. Nakai, M. Tatsumisago, T. Minami, Y. Himei, Y. Miura, M. Katada; J. Non-Cryst. Solids, 2002, 206, 227.

[185] D. Holland, M.E. Smith, A.P. Howes, T. Davies, L. Barret; *Phys. Chems. Glasses*, 2003, 44, 2, 59.

[186] A.C. Hannon, E.R. Barney, D. Holland; *Phys. Chem. Glasses*, 2009, 50, 5, 271.

[187] A. Paul, J.D. Donaldson, M.T. Donoghue, M.J.K. Thomas; *Phys. Chem. Glasses*, 1977, 18, 6, 125.

[188] B.C. Bunker, R.J. Kirkpatrick, R.K. Brow, G.I. Turner, C. Nelson; *J. Am. Ceram. Soc.*, 1991, 74, 1430.

[189] A.C. Hannon, D. Di Martino, L.F. Santos, R.M. Almeida; *J. Phys. Chem.*, 2007, 111, 3342.

[190] G.S. Henderson; *J. Non-Cryst. Solids*, 2007, 19, 254.

[191] R.K. Brow; *J. Non-Cryst. Solids*, 1996, 194, 267.

[192] R.K. Brow; *J. Non-Cryst. Solids*, 1997, 222, 396.

[193] L. Koudelka, P. Mosner; *Mater. Lett.*, 2000, 42, 194.

[194] R. Morena; *J. Non-Cryst. Solids*, 2000, 263-264, 382.

[195] J.W. Lim, M.L. Schmitt, R.K. Brow, S.W. Yung; *J. Non-Cryst. Solids*, 2010, 356, 1379.

[196] www.schott.com

[197] H. Yun, P.J. Bray; *J. Non-Cryst. Solids*, 1978, 30, 45.

[198] N.H. Ray; *Phys. Chem. Glasses*, 1975, 16, 75.

[199] A.R. Grimmer, U. Haubenreisser; *Chem. Phys. Lett.*, 1983, 99, 339.

[200] T.M. Duncan, D.C. Douglas; *Chem. Phys.*, 1984, 87, 339.

[201] L. Griffiths, A. Root, R.K. Harris, K.J. Packer, A.M. Chippendale, F.R. Tromans; *J. Chem. Soc. Dalton Trans.*, 1986, 2247.

[202] H. Eckert, *NMR Basic Principles Progr.*, 1994, 33, 125.

[203] L. Koudelka, P. Mošner, M. Zeyer, C. Jäger; *Phys Chem. Glasses*, 2002, 43C, 102.

[204] P.A. Flinn; in *"Mossbauer Isomer Shifts"*, North-Holland Publishing Company, 1978.

[205] J.G. Speight; *"Lange's Handbook of Chemistry (16th Edition)"*, McGraw-Hill, 2005.

[206] P.E. Lippens, J. Olivier-Fourcade, J.C. Jumas; *Hyperfine Interactions*, 2000, 126, 137.

[207] M. Zeyer-Düsterer, L. Montagne, G.Palavit, C. Jäger; *Sol. State Nucl. Magn. Reson.*, 2005, 27, 50.

[208] M. Schmidt, B. Ewald, Y. Prots, R. Cardoso-Gil, M. Armbrüster, I. Loa, L. Zhang, Y.X. Huang, U. Shwarz, R. Kniep; *Z. Anorg. Chem.*, 2004, 630, 5, 655.

[209] A.R. Grimmer, D. Müller, G. Gözel, R. Kniep; *Fresenius J. Anal. Chem.*, 1007, 357, 485.

[210] L. Koudelka, P. Mošner, J. Jirák, M. Zeyer-Düsterer, C. Jäger; *Phys. Chem. Glasses*, 2006, B47, 4, 471.

[211] E.T.Y. Lee, E.R.M. Taylor; *J. Phys. Chem. Solids*, 2005, 66, 47.

[212] Vogel, W.; Chemistry of Glass 1985 (Westerville, OH: American, Ceramic Society.

[213] F.S. De Vicente, M. Siu Li, M. Nalin, Y. Messaddeq; *J. Non-Cryst. Solids* 2003, 330, 168.

[214] P. Melnikov, F.J. dos Santos, S.B. Santagnelli, M.A.C. Secco, W.R. Guimaraes, A.Delben and J.R. Delben, *J. Therm. An. Calor.*, 2005, 81, 45.

[215] V. Dimitrov, T. Komatsu, *J. Non-Cryst. Solids* 1999, 249, 2-3, 160.

[216] M. Nalin, Y. Messaddeq, S.J.L. Ribeiro, M. Poulain, V. Briois, G.Brunklaus, C. Rosenhahn, B. D. Moseld and H. Eckert, *J. Mat. Chem.*, 2004, 14, 3398.

[217] M. Nalin, Ma. Poulain, Mi. Poulain, S.J.L. Ribeiro, Y. Messaddeq, *J. Non-Cryst. Solids*, 2001, 284, 110.

[218] R.E. Youngman, S. Sen, L.K. Corneliu, A.J.G. Ellison; *Phys. Chem. Glasses*, 2003, 44, 2, 69.

[219] G.W. Morey; *"The properties of Glass, 2nd edition*, New York, Reynhold Publishing Corp, 1954.

[220] K. Terashima, T. Hashimoto, T. Uchino, S.H. Kim, T. Yoko; *J. Ceram. Soc. Japan*, 1996, 104, 1008.

[221] T. Honma, R. Sato, Y. Benino, T. Komatsu, V. Dimitrov; *J. Non-Cryst. Solids*, 2000, 272, 1.

[222] A. Datta, A.K. Giri, D. Chakravorty; *Jpn. J. Appl. Phys.*, 1995, 34, 1431.

[223] J. Qi, D.F. Xue, G.L. Ning; *Phys. Chem. Glasses*, 2004, 45, 361.

[224] S Chatlani, J.E. Shelby; *Phys. Chem. Glasses*, 2006, 47, 288.

[225] V. Dimitrov, T. Komatsu, *J. Non-Cryst. Solids* 2010, Vol. 356, 258.

[226] D. Holland, A.C. Hannon, M.E. Smith, C.E. Johnson, M.F. Thomas, A.M. Beesley; *Sol. State Nucl. Magn. Reson.*, 2004, 26, 172.

[227] C. Svensson; *Acta Cryst.*, 1974, B30, 458.

[228] C. Svensson; *Acta Cryst.*, 1975, B31, 2016.

[229] M. Janssen *Acta Cryst.*, 1979, B35, 539.

[230] M. Nalin, G. Poirier, S.J.L. Ribeiro, Y. Messaddeq, L. Cescato; *J. Non-Cryst. Solids*, 2007, 353, 1592.

[231] G. Wu; *Chem. Phys. Lett.*, 1998, 298, 375.

[232] N.P. Seregin, S.A. Nemov S.M. Irkaev; *Semiconductors*, 2002, 36, 9, 975; translated from *Fizika i Tekhnica Poluprovodnikov*, 2002, 36, 9, 1049.

[233] R. Hussin, D. Holland, R. Dupree; *J. Non-Cryst. Solids*, 2002, 298, 32.

[234] M.M. Ahmed, C.A. Hogarth, M.A. Ghauri; *J. Mat. Sci. Let.*, 1984, 3, 341.

[235] N. Shinkai, R.C. Bradt, G.E. Rindone; *J. Mat. Sci. Let.*, 1983, 18, 2466.

[236] A.M. Efimov; *Glass. Phys. Chem.*, 1979, 5, 198.

[237] N.B. Knyazyan; *Glass. Phys. Chem.*, 1985, 11, 49.

[238] E.H. Ratcliffe; *Glass Technol.*, 1963, 4, 113.

[239] M. Montagna, F. Rossi; *J. Non-Cryst. Solids*, 1998, 231, 178.

[240] H. Masuda, R. Kimura, N. Sakamoto, K. Morinaga; *J. Jpn. Inst. Metals*, 1999, 63, 284.

[241] L.I. Lazoutova, V.S. Rabkin, E.V. Kozlova; *Proc. ICG*, 1998, D05, 5.

[242] O. Deparis, F.P. Mezzapesa, C. Corbari, P.G. Kazansky, K. Sakaguchi; *J. Non-Cryst. Solids*, 2005, 351, 2166.

[243] M.Z. Jhou, J.H. Jean; *J. Am. Ceram. Soc.*, 2006, 89, 786.

[244] D. Ehrt; *Phys. Chem. Glasses*, 2006, 47, 669.

[245] S.V. Nemilov, N.V. Komarova; *Glass Phys. Chem.*, 1992, 18, 558.

[246] A. Kajinami, Y. Harada, S. Inoue, S. Deki, N. Umesaki; *Jpn. J. Appl. Phys.*, 1999, Suppl. 38-1, 132.

[247] R.K. Brow, D.R. Tallant, S.T. Myers, C.C. Phifer; *J. Non-Cryst. Solids*, 1995, 191, 45.

[248] J.W. Wiench, M. Pruski, B. Tischendorf, J.U. Otaigbe, B.C. Sales; *J. Non-Cryst. Solids*, 2000, 263 - 264, 101.

[249] A. Gulino, G. Compagnini, A.A. Scalisi; *Chem. Mater.*, 2003, 15, 3332.

[250] G. Walter, U. Hoppe, J. Vogel, G. Carl, P. Hartmann; *J. Non-Cryst. Solids*, 2004, 333, 252.

[251] B. Tischendorf, T.M. Alam, R.T. Cygan, J.U. Otaigbe; *J. Non-Cryst. Solids*, 2003, 316, 261.

[252] G. Walter, G. Goerick, C. Rüssel; *J. Non-Cryst. Solids*, 2006, 352, 4051.

[253] U. Hoppe, G. Walter, G. Carl, J. Neuefeind, A.C. Hannon, *J. Non-Cryst. Solids*, 2005, 351, 1020.

[254] K. Suzuya, K. Itoh, A. Kajinami, C.K. Loong; *J. Non-Cryst. Solids*, 2004, 345-346, 80.

[255] J. Shanker, K. Singh; *Phys. Stat. Sol.*, 1982, (b) 109, 402.

[256] W.A. Weyl, Office of Naval Research, *Tech. Report No.66*, The Pennsylvania State University.

[257] H. Takebe, S. Fujino, K. Morinaga; *J. Am. Ceram. Soc.*, 1994, 77, 9, 2455.

[258] V. Dimitrov, S. Sakka; *J. Appl. Phys.*, 1996, 79, 3, 1736.

[259] V. Dimitrov, T. Komatsu; *J. Sol. State Chem.*, 2002, 163, 100.

[260] S. Sakaguchi, S. Todoroki; *App. Optics*, 1997, 36, 27, 6809.

[261] L. Rivoalen, A. Revcolevschi, J. Livage, R. Collongues; J. Non-Cryst. Solids, 1976, 21, 171.

[262] M. Wilson, P.A. Madden, S.A. Peebles, P.W. Fowler; *Mol. Physics*, 1996, 88, 4, 1143.

[263] P.N. Keating; *Phys. Rev.*, 1966, 145, 2, 637.

[264] M. Yoshimoto, N. Saga; *J. Ceram. Soc. Jap.*, 1986, 94, 1041.

[265] D.S. Sanditov, S.S. Sangadiev; *Glass Phys. Chem.*, 1998, 24, 525.

[266] N.V. Komarova, S.V. Nemilov; *Glass Phys. Chem.*, 1991, 17, 13.

[267] T.L. Barr; *"Modern ESCA, The Principles and Practice of X-Ray Photoelectron Spectroscopy"*, CRS Press, Boca Raton, 1994.

[268] E. Huheey, E.A. Keiter, R.L. Keiter; *"Inorganic Chemistry: Principles of structure and reactivity"*, Prentice Hall, 1996.

[269] S.K. Blower, C. Greaves; *Acta Cryst.*, 1988, C44, 587.

[270] A.I. Rabukhin; *Glass Ceram.*, 1994, 51, 353.

[271] R.A.H. El-Mallawany; *"Tellurite Glasses Handbook: Physical Properties and Data"*, CRC Press, 2002.

[272] Japanese Patent, A259259, 1996, Nikon Corporation.

[273] K. Matusita, H. Kato, T. Komatsu, M. Yoshimoto, N. Soga; *J. Non-Cryst. Solids*, 1989, 112, 341.

[274] J. Pirenne, E. Kartheuser;*Physica*, 1964, 30, 2005.

[275] N.C. Pyper; *J. Phys.: Condens. Matter.*, 1995, 7, 9127.

[276] N.C. Pyper; *Phil. Trans. R. Soc.*, 1986, A320, 107.

[277] K. Zábranský, Y. Jirásková; *AIP Conf. Proc.*, 2008, 1070, 10.

[278] E. Ratner, M. Ron; *Phys. Rev. B*, 1982, 25, 10, 6496.

[279] L. Dwynn Lafleur; *Phys. Rev. B*, 1979, 20, 7, 2581.

[280] X. Chen, Y. Luo, J. Zhang, K. Jiang, J.B. Pendry, S. Zhang; *Nature Commun.*, 2011, 2, 176.

[281] B. Zhang, Y. Luo, X. Liu, G. Barbastathis; *Phys. Rev. Let.*, 2011, 106, 033901.

Appendix A

Sénarmont method

A.1 Mathematical description of the polariscope

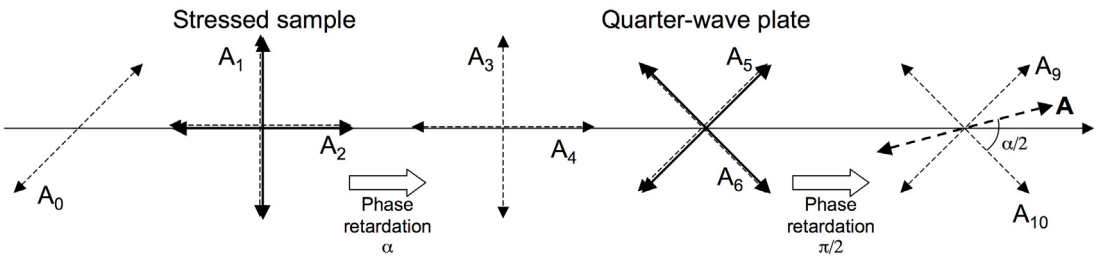

Figure A.1: The different states of polarization along the polariscope

A monochromatic unpolarized light is sent through a linear polarizer which polarizing axis makes an angle of 45°C with the direction of the uniaxial stress. This polarized wave can be described by the equation:

$$A_0 = a\sin(\omega t) \tag{A.1}$$

The different states of polarization along the polariscope are represented in Figure A.1. The direction of polarization of the waves and the polarizing axis of the stressed

sample and quarter-wave plate are shown. Passing through the stressed sample, the linearly polarized beam of light is decomposed in two components: an extraordinary component polarized in the direction of the uniaxial stress and an ordinary component perpendicular to the direction of the stress.

$$\begin{cases} A_1 = A_0 \cos\frac{\pi}{4} = \frac{a}{\sqrt{2}} \sin(\omega t) \\ A_2 = A_0 \cos\frac{\pi}{4} = \frac{a}{\sqrt{2}} \sin(\omega t) \end{cases} \tag{A.2}$$

The difference between the ordinary refractive index and the extraordinary refractive index induces a phase difference α between these two components. Equations A.2 becomes:

$$\begin{cases} A_3 = \frac{a}{\sqrt{2}} \sin(\omega t) \\ A_4 = \frac{a}{\sqrt{2}} \sin(\omega t - \alpha) \end{cases} \tag{A.3}$$

Through the quarter-wave plate, the component A_3 and A_4 are be combined to give two other components A_5 and A_6.

$$\begin{cases} A_5 = A_3 \cos\frac{\pi}{4} + A_4 \cos\frac{\pi}{4} \\ A_6 = A_3 \cos\frac{\pi}{4} - A_4 \cos\frac{\pi}{4} \end{cases}$$

$$\begin{cases} A_5 = \frac{a}{2} \sin(\omega t) + \frac{a}{2} \sin(\omega t - \alpha) \\ A_6 = \frac{a}{2} \sin(\omega t) - \frac{a}{2} \sin(\omega t - \alpha) \end{cases}$$

$$\begin{cases} A_5 = \frac{a}{2} [\sin(\omega t) + \sin(\omega t + \alpha] \\ A_6 = \frac{a}{2} [\sin(\omega t) - \sin(\omega t - \alpha)] \end{cases} \tag{A.4}$$

Trigonometric identity: $\cos A \sin B = \frac{1}{2}[\sin(A + B) + \sin(A - B)]$

Applying this formula to Equation A5:

$$\begin{cases} A + B = \omega t \\ A - B = \omega t - \alpha \end{cases}$$

$$\begin{cases} A = \omega t - B \\ \omega t - B - B = \omega t - \alpha \end{cases}$$

$$\begin{cases} A = \omega t - \frac{\alpha}{2} \\ B = \frac{\alpha}{2} \end{cases}$$

And then A_5 becomes A_7:

$$A_7 = a\cos(\omega t - \frac{\alpha}{2})\sin(\frac{\alpha}{2}) \tag{A.5}$$

A_6 can be transformed:

$$A_6 = \frac{a}{2}[\sin(\omega t) - \sin(\omega t - \alpha)] \tag{A.6}$$

Trigonometric identity: $\sin(-A) = -\sin(A)$

$$A_6 = \frac{a}{2}[\sin(\omega t) - (-\sin(\alpha - \omega t))]$$
$$A_6 = \frac{a}{2}[\sin(\omega t) + \sin(\alpha - \omega t)] \tag{A.7}$$

And then, applying the same treatment as A_5, A_6 becomes:

$$A_8 = a\sin(\omega t - \frac{\alpha}{2})\cos\frac{\alpha}{2} \tag{A.8}$$

A quarter-wave plate is composed of two axis, a fast axis and a slow axis, similar to the extraordinary and ordinary axis in the stressed sample. The fast and slow axis are perpendicular, and the light polarized along the fast axis will propagate faster than the light polarized along the slow axis. The thickness of the quarter-wave plate is determined to give rise to a phase difference of $\pi/2$ between the two perpendicular components. A quarter wave-plate can work only in narrow range of wavelengths

because the phase difference depends on the optical path.

In the following case the component A_7 corresponds to the component of the slow axis. A_7 becomes A_9 and A_8 becomes A_{10}.

$$A_9 = a\cos(\omega t - \frac{\alpha}{2} - \frac{\pi}{2})\sin(\frac{\alpha}{2}) \tag{A.9}$$

Trigonometric identity: $\cos(\theta - \frac{\pi}{2}) = \sin(\theta)$

$$\begin{cases} A_9 = a\sin(\omega t - \frac{\alpha}{2})\sin(\frac{\alpha}{2}) \\ A_{10} = a\sin(\omega t - \frac{\alpha}{2})\cos\frac{\alpha}{2} \end{cases} \tag{A.10}$$

$$A = a\sin(\omega t - \frac{\alpha}{2}) \tag{A.11}$$

$$\begin{cases} A_9 = A\sin(\frac{\alpha}{2}) \\ A_{10} = A\cos(\frac{\alpha}{2}) \end{cases} \tag{A.12}$$

Therefore the combination of A_9 and A_{10} gives a linearly polarized beam of light A (see Figure A.2).

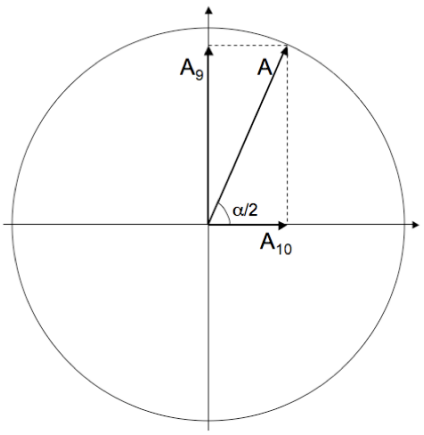

Figure A.2: Combination of A_9 and A_{10} giving linearly polarized wave A.

A.2 Elliptical polarization

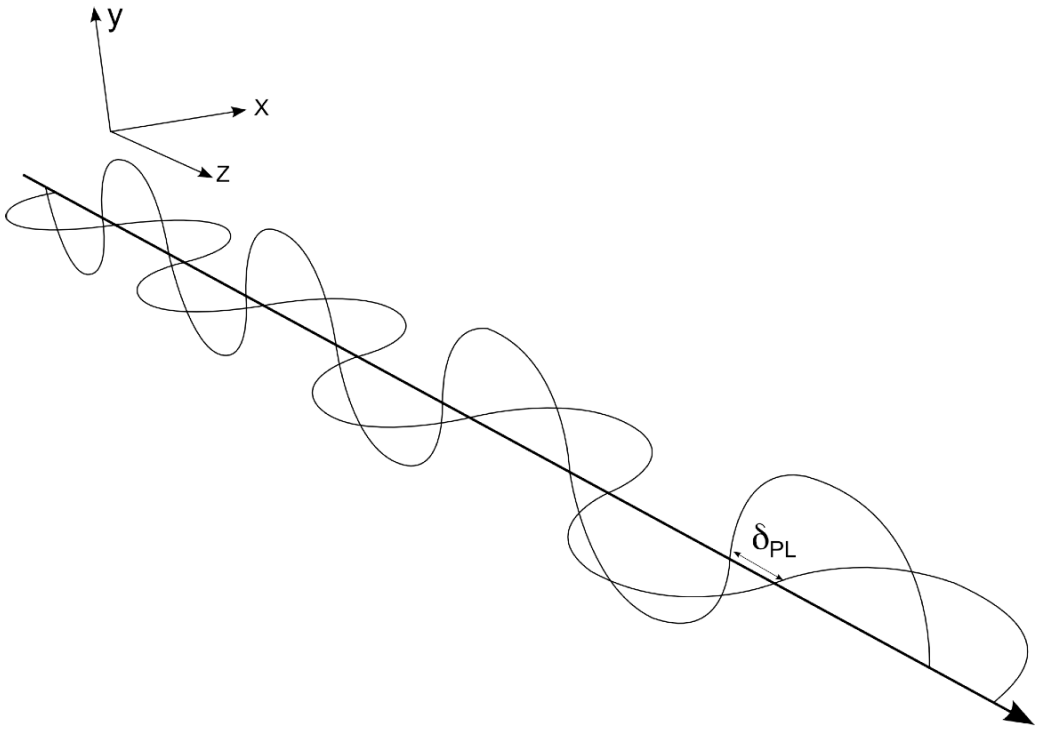

Figure A.3: Propagation of the elliptical polarized light

Equations A.3 can be written with general expressions:

$$A_3 = A_0 \cos\frac{\pi}{4} = \frac{a}{\sqrt{2}}\sin(\omega t)$$

$$\Rightarrow y = B\sin(\omega t) \tag{A.13}$$

$$A_4 = A_0 \cos\frac{\pi}{4} = \frac{a}{\sqrt{2}}\sin(\omega t - \alpha)$$

$$\Rightarrow x = C\sin(\omega t - \alpha) \tag{A.14}$$

where B and C are the amplitudes of each linearly polarized beam. In a general case B $\neq$ C but here $B = C = a/\sqrt{2}$ because the first linear polarizer polarized the light with an angle of 45° with respect to the direction of the stress. The component

y is considered to be polarized along the extraordinary axis, and the component x along the ordinary axis; the waves propagate along the z-axis. This is shown in Figure A.3. In addition, x has an angular phase retardation of α with respect to y ($\alpha = (2\pi\delta_{PL})/\lambda$, with δ_{PL} the effective path length difference).

A trigonometric identity gives: $\sin(A - B) = \sin A \cos B - \cos A \sin B$

Therefore Equation A.14 becomes:

$$x = C[\sin(\omega t)\cos(-\alpha) - \cos(\omega t)\sin(-\alpha)] \tag{A.15}$$

Geometrical considerations are represented in Figure A.4. The Z axis represents

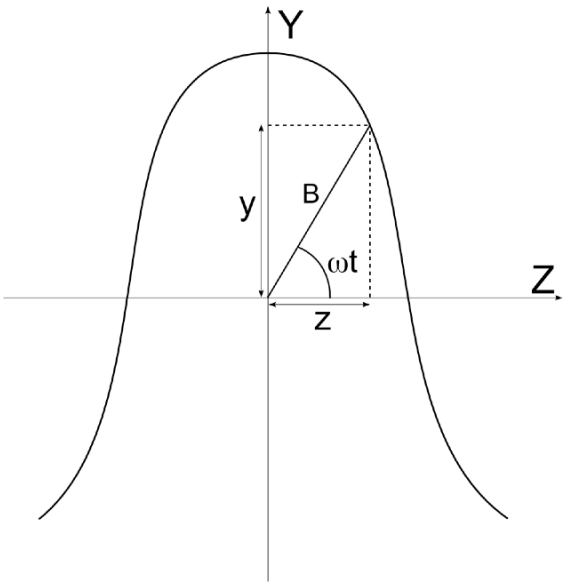

Figure A.4: Geometric considerations

the direction of the propagation of the electromagnetic wave, and the Y axis is the direction of the polarization of the wave described by Equation A.13, which is also the direction of the uniaxial stress. B is the amplitude of the wave and its projections

on the Y and Z axis are y (Equation A.13) and z respectively.

$$cos(\omega t) = \frac{z}{B} \tag{A.16}$$

and

$$B^2 = y^2 + z^2$$
$$z^2 = B^2 - y^2$$
$$z = \sqrt{B^2 - y^2}$$

Replacing z in Equation A.16

$$\cos(\omega t) = \frac{\sqrt{B^2 - y^2}}{B} \tag{A.17}$$

Also Equation A.13 gives:

$$\sin(\omega t) = \frac{y}{B} \tag{A.18}$$

Therefore Equation A.15 becomes:

$$x = C[\frac{y}{B}\cos(-\alpha) - \frac{\sqrt{B^2 - y^2}}{B}\sin(-\alpha)]$$
$$x = C[\frac{y}{B}\cos(\alpha) + \frac{\sqrt{B^2 - y^2}}{B}\sin(\alpha)]$$
$$\frac{B}{C}x = y\cos\alpha + \sqrt{B^2 - y^2}\sin\alpha$$
$$\frac{B}{C}x - y\cos\alpha = \sqrt{B^2 - y^2}\sin\alpha$$
$$(\frac{B}{C})^2x^2 - 2\frac{B}{C}xy\cos\alpha + y^2\cos^2\alpha = B^2\sin^2\alpha - y^2\sin^2\alpha$$
$$(\frac{B}{C})^2x^2 - 2\frac{B}{C}xy\cos\alpha + y^2\cos^2\alpha + y^2\sin^2\alpha = B^2\sin^2\alpha$$

Trigonometric identity: $\cos^2\theta + \sin^2\theta = 1$

$$(\frac{B}{C})^2x^2 - 2\frac{B}{C}xy\cos\alpha + y^2 = B^2\sin^2\alpha$$
$$\frac{x^2}{C^2} - \frac{2}{BC}xy\cos\alpha + \frac{y^2}{B^2} = \sin^2\alpha$$

This is the equation of an ellipse.

A.3 Orientation of the quarter-wave plate

In a previous section, it was considered that the wave described by A_7 was on the slow axis of the quarter-wave plate. This case gives two components A_9 and A_{10} that can be combined to give a linearly polarized light A.

$$\begin{cases} A_9 = A\sin(\frac{\alpha}{2}) \\ A_{10} = A\cos(\frac{\alpha}{2}) \end{cases} \tag{A.12}$$

Now the case with A_8 on the slow axis is considered, and in this case A_{10} has a retardation of $\pi/2$:

$$A_{10} = a\sin(\omega t - \frac{\alpha}{2} - \frac{\pi}{2})\cos(\frac{\alpha}{2}) \tag{A.19}$$

Trigonometric identity: $\sin(\theta - \frac{\pi}{2}) = \cos(\theta)$

$$\begin{cases} A_{10} = a\cos(\omega t - \frac{\alpha}{2})\cos(\frac{\alpha}{2}) \\ A_9 = a\cos(\omega t - \frac{\alpha}{2})\sin(\frac{\alpha}{2}) \end{cases} \tag{A.20}$$

$$A' = a\cos(\omega t - \frac{\alpha}{2}) \tag{A.21}$$

$$\begin{cases} A_9 = A\sin(\frac{\alpha}{2}) \\ A_{10} = A\cos(\frac{\alpha}{2}) \end{cases} \tag{A.22}$$

Therefore the orientation of the quarter-wave plate is not really important. The fast axis and the slow axis can be switched, the angle of the linearly polarized beam A is always $\alpha/2$. However the slow and fast axis have to make an angle of 45with the direction of the stress.

A.4 Analyzer

In the graph Intensity = f(θ), is the angular phase retardation α determined by the angle giving a maximum or a miminum value for the intensity?
Depending how the analyzer is set up at the beginning of the experiment, α can be determined by a maximum or a miminum in the graph Intensity = f(θ). Before to start the measurement, the position of the analyser has to be set up. To do so no stress has to be applied on the sample. Two cases are possible:

- Case1: If the polarizing axis of the analyser is parallel to the axis of the first polarizer, therefore a maximum transmission (minimum absorption) is measured.
- Case 2: If the polarizing axis of the analyser is perpendicular to the axis of the first polarizer, therefore a minimum transmission (maximum absorption) is measured.

Therefore in case 1 α is given by a maximum **transmission** and in case 2 α is given by a maximum **absorption**.

A.5 Determination of the Stress Optic Coefficient

A.5.1 Direct calculation

The stress optic coefficient C is calculated through the formula:

$$\delta_{PL} = Cl\sigma \tag{A.23}$$

$$C = \frac{\delta_{PL}}{l\sigma} \tag{A.24}$$

Where δ_{PL} is the effective path length difference, l the sample thickness and σ the mechanical stress applied on the glass sample.

In the part 2.1, it was said that the angular phase retardation is α. The effective path length difference δ_{PL} and the angular phase retardation α are related trhough the equation:

$$\alpha = \frac{2\pi\delta_{PL}}{\lambda} \tag{A.25}$$

The value of α has to be in radian. The angle θ measured with the analyzer is equal to $\alpha/2$ and is measured in degrees, therefore θ has to be changed in radian:

$$\theta_{(radian)} = \frac{\theta_{(degree)}2\pi}{360} = \frac{\theta_{(degree)}\pi}{180} \tag{A.26}$$

$$\frac{\alpha}{2} = \theta_{(radian)} \tag{A.27}$$

$$\frac{\alpha}{2} = \frac{\theta_{(degree)}\pi}{180} \tag{A.28}$$

$$\alpha = \frac{2\theta_{(degree)}\pi}{180} = \frac{\theta_{(degree)}\pi}{90} \tag{A.29}$$

From Equation A.25, the effective path length difference can be written:

$$\delta_{PL} = \frac{\alpha\lambda}{2\pi} \tag{A.30}$$

$$\delta_{PL} = \frac{\theta_{(degree)}\pi}{90}\frac{\lambda}{2\pi} = \frac{\theta_{(degree)}\lambda}{180} \tag{A.31}$$

The mechanical stress is the ratio of a pressure by a surface, it can be calculated from the strength applied on the surface of the glass:

$$\sigma = \frac{Pg}{A} \tag{A.32}$$

Where P is the weigh applied on the sample (in kg), g is the standard gravitational acceleration (in $m.s^{-2}$) and A is the area of the sample on which the weigh is applied. The stress calculated from these units is given in Pascal (Pa).
The stress optic coefficient C is given in Brewsters which is equivalent to $10^{-12}m^{-2}.N^{-1}$; to be able to obtain this unit, the mechanical stress has to be given with the unit $10^5N.m^{-2}$. Therefore Equation A.32 has to be slightly transformed:

$$\sigma = \frac{Pg}{A}10^{-5} \ \ (10^5N.m^{-2}) \tag{A.33}$$

This point will be explained in the next part about the units.
If Equation A.31 and Equation A.33 are introduced in Equation A.24, the expression of the stress optic coefficient is given by:

$$C = \frac{\lambda A \theta_{degree}}{180 l P g} \times 10^{-5} \tag{A.34}$$

Where: λ: wavelength (in Å)
A: area of the sample (in m^2)
θ_{degree}: angle measured with the analyser (in degree)
l: thickness of the sample (in mm)
P: weight applied on the surface A of the sample (in kg)
g: standard gravitational acceleration (9.8 $m.s^{-2}$)

This equation gives the value of stress optic coefficient in brewster directly from the parameters given by the experiment
However, it can also be convenient to calculate C by another way. The Equation A.23 can be written:

$$\frac{\delta_{PL}}{l} = C\sigma \tag{A.35}$$

From all the data given by the experiment (λ, A, θ_{degree}, l and P), δ_{PL} and σ can be calculated from Equation A.31 and Equation A.33. The graph for $\delta_{PL}/l = f(\sigma)$ (Equation A.35) must give a line and its slope is the stress optic coefficient C.

A.5.2 Coherence of the units

A brewster is a unit equivalent to $10^{-12} m^2.N^{-1}$. This section will demonstrate that Equation A.34 is coherent and that the combination of the different parameters gives a stress optic coefficient in Brewster.
The mechanical stress has the unit of a pressure, it is the ratio of a strength by a surface and its value is given by Equation A.33. In this equation, P is in kg, g in $m.s^{-2}$ and A in m^2.

$$[\sigma] = \frac{[kg]\times[m]}{[m]^2\times[s]^2}$$

The mechanical stress should be the ratio of a strength by a surface, but in this expression the strength does not appear. By definition a newton is equivalent to $kg.m.s^{-2}$.

$$[N] \equiv [kg][m][s]^{-2}$$

$$[g] \equiv [m][s]^{-2} \equiv [kg][m][s]^{-2}[kg]^{-1} \equiv [N][kg]^{-1}$$

Therefore the unit for the mechanical stress is:

$$[\sigma] \equiv \frac{[P][g]}{[A]} \equiv \frac{[kg][N]}{[m]^2[kg]} \equiv \frac{[N]}{[m]^2} (\equiv [Pa])$$

The effective path length difference has to be in angström, which is equivalent to 10^{-10}m; its expression is given by Equation A.31.

$$[\delta] \equiv \frac{[\theta_{degree}][\lambda]}{[180^o]} \equiv \frac{[degree]10^{-10}[m]}{[degree]} \equiv 10^{-10}[m]$$

The thickness of the sample has to be in mm which is equivalent to 10^{-3} m.

$$[l] \equiv 10^{-3}[m]$$

Therefore the unit of C is:

$$[C] \equiv \frac{[\delta]}{[l][\sigma]} \equiv \frac{10^{-10}[m][m]^2}{10^{-3}[m][N]} \equiv 10^{-7}\frac{[m]^2}{[N]}$$

From all these considerations the unit of C is not a brewster but 10^{-5} brewster. To obtain a brewster, the solution can be to introduce a mechanical stress with a value corresponding to $10^5 N.m^{-2}$ (equivalent to $10^5 Pa$). This operation is done in Equation A.33.

$$[C] \equiv \frac{[\delta]}{[l][\sigma]} \equiv \frac{10^{-10}[m][m]^2}{10^{-3}[m]10^5[N]} \equiv 10^{-12}\frac{[m]^2}{[N]} \equiv [brewster]$$

Appendix B

Copyright Permission

This sections contains terms and conditions of the Elsevier Licence.

ELSEVIER LICENSE
TERMS AND CONDITIONS

Apr 26, 2011

This is a License Agreement between Vincent Martin ("You") and Elsevier ("Elsevier") provided by Copyright Clearance Center ("CCC"). The license consists of your order details, the terms and conditions provided by Elsevier, and the payment terms and conditions.

All payments must be made in full to CCC. For payment instructions, please see information listed at the bottom of this form.

Supplier	Elsevier Limited The Boulevard,Langford Lane Kidlington,Oxford,OX5 1GB,UK
Registered Company Number	1982084
Customer name	Vincent Martin
Customer address	5221 Cornwallis street Halifax, NS B3K0B6
License number	2656691162328
License date	Apr 26, 2011
Licensed content publisher	Elsevier
Licensed content publication	Journal of Non-Crystalline Solids
Licensed content title	Structural aspects of the photoelastic response in lead borate glasses
Licensed content author	V. Martin, B. Wood, U. Werner-Zwanziger, J.W. Zwanziger
Licensed content date	1 May 2011
Licensed content volume number	357
Licensed content issue number	10
Number of pages	6
Start Page	2120
End Page	2125
Type of Use	reuse in a thesis/dissertation
Intended publisher of new work	other
Portion	full article
Format	both print and electronic
Are you the author of this Elsevier article?	Yes

Will you be translating?	No
Order reference number	
Title of your thesis/dissertation	Structural dependence of the photoelastic response of oxide glass
Expected completion date	Sep 2011
Estimated size (number of pages)	200
Elsevier VAT number	GB 494 6272 12
Permissions price	0.00 USD
VAT/Local Sales Tax	0.0 USD / 0.0 GBP
Total	0.00 USD
Terms and Conditions	

INTRODUCTION

1. The publisher for this copyrighted material is Elsevier. By clicking "accept" in connection with completing this licensing transaction, you agree that the following terms and conditions apply to this transaction (along with the Billing and Payment terms and conditions established by Copyright Clearance Center, Inc. ("CCC"), at the time that you opened your Rightslink account and that are available at any time at http://myaccount.copyright.com).

GENERAL TERMS

2. Elsevier hereby grants you permission to reproduce the aforementioned material subject to the terms and conditions indicated.

3. Acknowledgement: If any part of the material to be used (for example, figures) has appeared in our publication with credit or acknowledgement to another source, permission must also be sought from that source. If such permission is not obtained then that material may not be included in your publication/copies. Suitable acknowledgement to the source must be made, either as a footnote or in a reference list at the end of your publication, as follows:

"Reprinted from Publication title, Vol /edition number, Author(s), Title of article / title of chapter, Pages No., Copyright (Year), with permission from Elsevier [OR APPLICABLE SOCIETY COPYRIGHT OWNER]." Also Lancet special credit - "Reprinted from The Lancet, Vol. number, Author(s), Title of article, Pages No., Copyright (Year), with permission from Elsevier."

4. Reproduction of this material is confined to the purpose and/or media for which permission is hereby given.

5. Altering/Modifying Material: Not Permitted. However figures and illustrations may be altered/adapted minimally to serve your work. Any other abbreviations, additions, deletions and/or any other alterations shall be made only with prior written authorization of Elsevier Ltd. (Please contact Elsevier at permissions@elsevier.com)

6. If the permission fee for the requested use of our material is waived in this instance,

please be advised that your future requests for Elsevier materials may attract a fee.

7. Reservation of Rights: Publisher reserves all rights not specifically granted in the combination of (i) the license details provided by you and accepted in the course of this licensing transaction, (ii) these terms and conditions and (iii) CCC's Billing and Payment terms and conditions.

8. License Contingent Upon Payment: While you may exercise the rights licensed immediately upon issuance of the license at the end of the licensing process for the transaction, provided that you have disclosed complete and accurate details of your proposed use, no license is finally effective unless and until full payment is received from you (either by publisher or by CCC) as provided in CCC's Billing and Payment terms and conditions. If full payment is not received on a timely basis, then any license preliminarily granted shall be deemed automatically revoked and shall be void as if never granted. Further, in the event that you breach any of these terms and conditions or any of CCC's Billing and Payment terms and conditions, the license is automatically revoked and shall be void as if never granted. Use of materials as described in a revoked license, as well as any use of the materials beyond the scope of an unrevoked license, may constitute copyright infringement and publisher reserves the right to take any and all action to protect its copyright in the materials.

9. Warranties: Publisher makes no representations or warranties with respect to the licensed material.

10. Indemnity: You hereby indemnify and agree to hold harmless publisher and CCC, and their respective officers, directors, employees and agents, from and against any and all claims arising out of your use of the licensed material other than as specifically authorized pursuant to this license.

11. No Transfer of License: This license is personal to you and may not be sublicensed, assigned, or transferred by you to any other person without publisher's written permission.

12. No Amendment Except in Writing: This license may not be amended except in a writing signed by both parties (or, in the case of publisher, by CCC on publisher's behalf).

13. Objection to Contrary Terms: Publisher hereby objects to any terms contained in any purchase order, acknowledgment, check endorsement or other writing prepared by you, which terms are inconsistent with these terms and conditions or CCC's Billing and Payment terms and conditions. These terms and conditions, together with CCC's Billing and Payment terms and conditions (which are incorporated herein), comprise the entire agreement between you and publisher (and CCC) concerning this licensing transaction. In the event of any conflict between your obligations established by these terms and conditions and those established by CCC's Billing and Payment terms and conditions, these terms and conditions shall control.

14. Revocation: Elsevier or Copyright Clearance Center may deny the permissions described in this License at their sole discretion, for any reason or no reason, with a full refund payable to you. Notice of such denial will be made using the contact information provided by you. Failure to receive such notice will not alter or invalidate the denial. In no event will Elsevier or Copyright Clearance Center be responsible or liable for any costs, expenses or damage incurred by you as a result of a denial of your permission request,

other than a refund of the amount(s) paid by you to Elsevier and/or Copyright Clearance Center for denied permissions.

LIMITED LICENSE

The following terms and conditions apply only to specific license types:

15. **Translation**: This permission is granted for non-exclusive world **English** rights only unless your license was granted for translation rights. If you licensed translation rights you may only translate this content into the languages you requested. A professional translator must perform all translations and reproduce the content word for word preserving the integrity of the article. If this license is to re-use 1 or 2 figures then permission is granted for non-exclusive world rights in all languages.

16. **Website**: The following terms and conditions apply to electronic reserve and author websites:
Electronic reserve: If licensed material is to be posted to website, the web site is to be password-protected and made available only to bona fide students registered on a relevant course if:
This license was made in connection with a course,
This permission is granted for 1 year only. You may obtain a license for future website posting,
All content posted to the web site must maintain the copyright information line on the bottom of each image,
A hyper-text must be included to the Homepage of the journal from which you are licensing at http://www.sciencedirect.com/science/journal/xxxxx or the Elsevier homepage for books at http://www.elsevier.com , and
Central Storage: This license does not include permission for a scanned version of the material to be stored in a central repository such as that provided by Heron/XanEdu.

17. **Author website** for journals with the following additional clauses:

All content posted to the web site must maintain the copyright information line on the bottom of each image, and
he permission granted is limited to the personal version of your paper. You are not allowed to download and post the published electronic version of your article (whether PDF or HTML, proof or final version), nor may you scan the printed edition to create an electronic version,
A hyper-text must be included to the Homepage of the journal from which you are licensing at http://www.sciencedirect.com/science/journal/xxxxx , As part of our normal production process, you will receive an e-mail notice when your article appears on Elsevier's online service ScienceDirect (www.sciencedirect.com). That e-mail will include the article's Digital Object Identifier (DOI). This number provides the electronic link to the published article and should be included in the posting of your personal version. We ask that you wait until you receive this e-mail and have the DOI to do any posting.
Central Storage: This license does not include permission for a scanned version of the material to be stored in a central repository such as that provided by Heron/XanEdu.

18. **Author website** for books with the following additional clauses:
Authors are permitted to place a brief summary of their work online only.
A hyper-text must be included to the Elsevier homepage at http://www.elsevier.com

All content posted to the web site must maintain the copyright information line on the bottom of each image

You are not allowed to download and post the published electronic version of your chapter, nor may you scan the printed edition to create an electronic version.

Central Storage: This license does not include permission for a scanned version of the material to be stored in a central repository such as that provided by Heron/XanEdu.

19. **Website** (regular and for author): A hyper-text must be included to the Homepage of the journal from which you are licensing at http://www.sciencedirect.com/science/journal/xxxxx. or for books to the Elsevier homepage at http://www.elsevier.com

20. **Thesis/Dissertation**: If your license is for use in a thesis/dissertation your thesis may be submitted to your institution in either print or electronic form. Should your thesis be published commercially, please reapply for permission. These requirements include permission for the Library and Archives of Canada to supply single copies, on demand, of the complete thesis and include permission for UMI to supply single copies, on demand, of the complete thesis. Should your thesis be published commercially, please reapply for permission.

21. **Other Conditions**:

v1.6

Gratis licenses (referencing $0 in the Total field) are free. Please retain this printable license for your reference. No payment is required.

If you would like to pay for this license now, please remit this license along with your payment made payable to "COPYRIGHT CLEARANCE CENTER" otherwise you will be invoiced within 48 hours of the license date. Payment should be in the form of a check or money order referencing your account number and this invoice number RLNK10976512.
Once you receive your invoice for this order, you may pay your invoice by credit card. Please follow instructions provided at that time.

Make Payment To:
Copyright Clearance Center
Dept 001
P.O. Box 843006
Boston, MA 02284-3006

For suggestions or comments regarding this order, contact Rightslink Customer Support: customercare@copyright.com or +1-877-622-5543 (toll free in the US) or +1-978-646-2777.

Appendix C

Copyright Permission

This sections contains terms and conditions of the John Wiley and Sons Licence.

JOHN WILEY AND SONS LICENSE
TERMS AND CONDITIONS

May 19, 2011

This is a License Agreement between Vincent Martin ("You") and John Wiley and Sons ("John Wiley and Sons") provided by Copyright Clearance Center ("CCC"). The license consists of your order details, the terms and conditions provided by John Wiley and Sons, and the payment terms and conditions.

All payments must be made in full to CCC. For payment instructions, please see information listed at the bottom of this form.

License Number	2672791222581
License date	May 19, 2011
Licensed content publisher	John Wiley and Sons
Licensed content publication	International Journal of Applied Glass Science
Licensed content title	Correlation of Structure and Photoelastic Response in Tin Phosphate Glass
Licensed content author	Vincent Martin,Ulrike Werner-Zwanziger,Josef W. Zwanziger,Richard A. Dunlap
Licensed content date	Apr 1, 2011
Start page	no
End page	no
Type of use	Dissertation/Thesis
Requestor type	Author of this Wiley article
Format	Print and electronic
Portion	Full article
Will you be translating?	No
Order reference number	
Total	0.00 USD
Terms and Conditions	

TERMS AND CONDITIONS

This copyrighted material is owned by or exclusively licensed to John Wiley & Sons, Inc. or one of its group companies (each a "Wiley Company") or a society for whom a Wiley Company has exclusive publishing rights in relation to a particular journal (collectively "WILEY"). By clicking "accept" in connection with completing this licensing transaction, you agree that the following terms and conditions apply to this transaction (along with the billing and payment terms and conditions established by the Copyright Clearance Center Inc., ("CCC's Billing and Payment terms and conditions"), at the time that you opened your Rightslink account (these are available at any time at http://myaccount.copyright.com)

Terms and Conditions

1. The materials you have requested permission to reproduce (the "Materials") are protected by

copyright.

2. You are hereby granted a personal, non-exclusive, non-sublicensable, non-transferable, worldwide, limited license to reproduce the Materials for the purpose specified in the licensing process. This license is for a one-time use only with a maximum distribution equal to the number that you identified in the licensing process. Any form of republication granted by this licence must be completed within two years of the date of the grant of this licence (although copies prepared before may be distributed thereafter). The Materials shall not be used in any other manner or for any other purpose. Permission is granted subject to an appropriate acknowledgement given to the author, title of the material/book/journal and the publisher and on the understanding that nowhere in the text is a previously published source acknowledged for all or part of this Material. Any third party material is expressly excluded from this permission.

3. With respect to the Materials, all rights are reserved. Except as expressly granted by the terms of the license, no part of the Materials may be copied, modified, adapted (except for minor reformatting required by the new Publication), translated, reproduced, transferred or distributed, in any form or by any means, and no derivative works may be made based on the Materials without the prior permission of the respective copyright owner. You may not alter, remove or suppress in any manner any copyright, trademark or other notices displayed by the Materials. You may not license, rent, sell, loan, lease, pledge, offer as security, transfer or assign the Materials, or any of the rights granted to you hereunder to any other person.

4. The Materials and all of the intellectual property rights therein shall at all times remain the exclusive property of John Wiley & Sons Inc or one of its related companies (WILEY) or their respective licensors, and your interest therein is only that of having possession of and the right to reproduce the Materials pursuant to Section 2 herein during the continuance of this Agreement. You agree that you own no right, title or interest in or to the Materials or any of the intellectual property rights therein. You shall have no rights hereunder other than the license as provided for above in Section 2. No right, license or interest to any trademark, trade name, service mark or other branding ("Marks") of WILEY or its licensors is granted hereunder, and you agree that you shall not assert any such right, license or interest with respect thereto.

5. NEITHER WILEY NOR ITS LICENSORS MAKES ANY WARRANTY OR REPRESENTATION OF ANY KIND TO YOU OR ANY THIRD PARTY, EXPRESS, IMPLIED OR STATUTORY, WITH RESPECT TO THE MATERIALS OR THE ACCURACY OF ANY INFORMATION CONTAINED IN THE MATERIALS, INCLUDING, WITHOUT LIMITATION, ANY IMPLIED WARRANTY OF MERCHANTABILITY, ACCURACY, SATISFACTORY QUALITY, FITNESS FOR A PARTICULAR PURPOSE, USABILITY, INTEGRATION OR NON-INFRINGEMENT AND ALL SUCH WARRANTIES ARE HEREBY EXCLUDED BY WILEY AND ITS LICENSORS AND WAIVED BY YOU.

6. WILEY shall have the right to terminate this Agreement immediately upon breach of this Agreement by you.

7. You shall indemnify, defend and hold harmless WILEY, its Licensors and their respective directors, officers, agents and employees, from and against any actual or threatened claims, demands, causes of action or proceedings arising from any breach of this Agreement by you.

8. IN NO EVENT SHALL WILEY OR ITS LICENSORS BE LIABLE TO YOU OR ANY OTHER PARTY OR ANY OTHER PERSON OR ENTITY FOR ANY SPECIAL, CONSEQUENTIAL, INCIDENTAL, INDIRECT, EXEMPLARY OR PUNITIVE DAMAGES, HOWEVER CAUSED, ARISING OUT OF OR IN CONNECTION WITH THE DOWNLOADING, PROVISIONING, VIEWING OR USE OF THE MATERIALS REGARDLESS OF THE FORM OF ACTION, WHETHER FOR BREACH OF CONTRACT, BREACH OF WARRANTY, TORT, NEGLIGENCE, INFRINGEMENT OR OTHERWISE (INCLUDING, WITHOUT LIMITATION, DAMAGES BASED ON LOSS OF PROFITS, DATA, FILES, USE, BUSINESS OPPORTUNITY OR CLAIMS OF THIRD PARTIES), AND WHETHER OR NOT THE PARTY HAS BEEN ADVISED OF THE POSSIBILITY OF SUCH DAMAGES. THIS LIMITATION SHALL APPLY NOTWITHSTANDING ANY FAILURE OF ESSENTIAL PURPOSE OF ANY LIMITED REMEDY PROVIDED HEREIN.

9. Should any provision of this Agreement be held by a court of competent jurisdiction to be illegal, invalid, or unenforceable, that provision shall be deemed amended to achieve as nearly as possible the same economic effect as the original provision, and the legality, validity and

enforceability of the remaining provisions of this Agreement shall not be affected or impaired thereby.

10. The failure of either party to enforce any term or condition of this Agreement shall not constitute a waiver of either party's right to enforce each and every term and condition of this Agreement. No breach under this agreement shall be deemed waived or excused by either party unless such waiver or consent is in writing signed by the party granting such waiver or consent. The waiver by or consent of a party to a breach of any provision of this Agreement shall not operate or be construed as a waiver of or consent to any other or subsequent breach by such other party.

11. This Agreement may not be assigned (including by operation of law or otherwise) by you without WILEY's prior written consent.

12. Any fee required for this permission shall be non-refundable after thirty (30) days from receipt.

13. These terms and conditions together with CCC's Billing and Payment terms and conditions (which are incorporated herein) form the entire agreement between you and WILEY concerning this licensing transaction and (in the absence of fraud) supersedes all prior agreements and representations of the parties, oral or written. This Agreement may not be amended except in writing signed by both parties. This Agreement shall be binding upon and inure to the benefit of the parties' successors, legal representatives, and authorized assigns.

14. In the event of any conflict between your obligations established by these terms and conditions and those established by CCC's Billing and Payment terms and conditions, these terms and conditions shall prevail.

15. WILEY expressly reserves all rights not specifically granted in the combination of (i) the license details provided by you and accepted in the course of this licensing transaction, (ii) these terms and conditions and (iii) CCC's Billing and Payment terms and conditions.

16. This Agreement will be void if the Type of Use, Format, Circulation, or Requestor Type was misrepresented during the licensing process.

17. This Agreement shall be governed by and construed in accordance with the laws of the State of New York, USA, without regards to such state's conflict of law rules. Any legal action, suit or proceeding arising out of or relating to these Terms and Conditions or the breach thereof shall be instituted in a court of competent jurisdiction in New York County in the State of New York in the United States of America and each party hereby consents and submits to the personal jurisdiction of such court, waives any objection to venue in such court and consents to service of process by registred or certified mail, return receipt requested, at the last known address of such party. . BY CLICKING ON THE "I ACCEPT" BUTTON, YOU ACKNOWLEDGE THAT YOU HAVE READ AND FULLY UNDERSTAND EACH OF THE SECTIONS OF AND PROVISIONS SET FORTH IN THIS AGREEMENT AND THAT YOU ARE IN AGREEMENT WITH AND ARE WILLING TO ACCEPT ALL OF YOUR OBLIGATIONS AS SET FORTH IN THIS AGREEMENT.

v1.4

Gratis licenses (referencing $0 in the Total field) are free. Please retain this printable license for your reference. No payment is required.

If you would like to pay for this license now, please remit this license along with your payment made payable to "COPYRIGHT CLEARANCE CENTER" otherwise you will be invoiced within 48 hours of the license date. Payment should be in the form of a check or money order referencing your account number and this invoice number RLNK10990669.
Once you receive your invoice for this order, you may pay your invoice by credit card. Please follow instructions provided at that time.

Make Payment To:

Copyright Clearance Center
Dept 001
P.O. Box 843006
Boston, MA 02284-3006

For suggestions or comments regarding this order, contact Rightslink Customer Support: customercare@copyright.com or +1-877-622-5543 (toll free in the US) or +1-978-646-2777.